DYNAMICS OF NUCLEAR REACTIONS IN SUPERHEAVY MASS REGION

A THESIS

Submitted to the

FACULTY OF SCIENCE

THAPAR UNIVERSITY, PATIALA

for the degree of

DOCTOR OF PHILOSOPHY

by

KIRANDEEP SANDHU

SCHOOL OF PHYSICS AND MATERIALS SCIENCE

THAPAR UNIVERSITY

PATIALA-147004

INDIA

Dedicated to

my parents who gave me life

and

made it worth living

CERTIFICATE

This is to certify that the thesis entitled "**DYNAMICS OF NUCLEAR REACTIONS IN SUPERHEAVY MASS REGION**" being submitted by **Ms. Kirandeep Sandhu** for the fulfilment of the requirements for the award of Degree of Doctor of Philosophy in the School of Physics and Materials Science, Thapar University, Patiala, is a record of the candidate's own work carried out by her under my supervision. The matter presented in this thesis has not been submitted in part or full for the award of any degree in any university or institute.

Supervisor

Dr. Manoj K. Sharma

Professor and Head

School of Physics and Materials Science

Thapar University, Patiala- 147004

Punjab (India)

Thapar University, Patiala

CANDIDATE'S DECLARATION

I hereby certify that the thesis entitled "**DYNAMICS OF NUCLEAR REACTIONS IN SUPERHEAVY MASS REGION**" in partial fulfilment of the requirements for the award of Degree of Doctor of Philosophy in the School of Physics and Materials Science, Thapar University, Patiala, is a record of my own work carried under the supervision of Dr. Manoj K. Sharma. The matter presented in this thesis has not been submitted by me in part or full for the award of any other degree in any other university or institute.

This is to certify that the above statement made by the candidate is correct to the best of our knowledge.

Dr. Manoj K. Sharma

(Supervisor)

Head of the Department

29/7/15

Dean R&SP

29/7/2015

External Examiner

Date: 29.7.2015

Acknowledgements

My first thanks go to the Almighty who gave me the strength and wisdom to accomplish the task assigned to me pertaining to this research work.

My vocabulary runs short to express my sincere and deepest gratitude to my supervisor, Dr. Manoj K. Sharma, Professor and Head, School of Physics and Materials Science, Thapar University, Patiala, who left no stone unturned in guiding me at every step of my research. He is a unique combination of patience, calmness and positive thinking. In spite of his busy schedule, he always stole some time to give me useful tips in my research work. Many a time when I fumbled in choosing the right procedure in my work, he came to rescue and showed me the infallible path to go ahead and continue my work. Apart from learning from my revered supervisor a lot of the subject in question, I imbibed so many personal attributes from his demeanor which will stand in good stead in my future life. I learned to stay unperturbed in a situation where there seemed to be no way out. Thank you very much sir. Special thanks to madam Sharma for her affection.

I gratefully recognize the collaborative effort of Dr. Raj K. Gupta, Professor of Physics (Retd.), Physics Department, Panjab University, Chandigarh for his suggestions and positive criticisms in my research work. He has a vast experience of more than four decades in the field of research. He provided me with the nuances of research work.

I would be failing in my duty if I do not pay due respect and thanks to the Advisory Doctoral Committee comprising Dr. Suneel Kumar, Dr. A. K. Lal and Dr. Alka Upadhyay. At all the presentations that I gave every six months the Doctoral Committee gave very valuable suggestions. After the presentations, the Committee discussed all the points among themselves and later on apprised me of certain modifications or improvements wherever necessary. I am really grateful to all the members of the Doctoral Committee for all the help they gave me.

The Dean of Research and Sponsored Projects of Thapar university, Dr. O. P. Pandey, deserves my gratitude and thanks for encouraging me and providing me the possible research facilities. I am very much thankful to him for his affectionate behavior throughout the period of my research. Special thanks to Dr. Kulvir Singh for providing me useful and valuable tips for research and fellowship as a teaching associate well in time. Also, I express my gratitude to all the faculty and staff of the School for their help and kind support.

I would like to thank Dr. Raj Kumar, Dr. Gudveen Sawhney and Dr. Karan Singh Vinayak for their gentle guidance and suggestions which have helped me during my Ph.D. tenure. I am also thankful to Dr. Deepika Jain for her encouragement and support.

This thesis would not have been possible without the assistance of a number of individuals. I would like to thank Miss Gurvinder Kaur for the co-operation, encouragement and all time help. I am grateful to Anirudh, Mandeep, Navjot, Kamal, Aman, Rajni, Sangeeta, Neha and Kanishka for the help, support and jovial company. I am thankful to many others who are not mentioned here but contributed to the completion of this thesis.

Though last but not the least, my family, especially my younger sister Roopkiran Sandhu deserve my gratitude and thanks for their unstinting support in completing my assigned job. I don't think I can ever repay my parents for their affection and the labour they did to see me succeed in my mission. My father, Mr. Amteshwar Singh Sandhu, in spite of the pangs he had been suffering, never grudged to drop me at the university or bring me back home at late hours. I find no words to thank my mother, Kamaljit Kaur Sandhu, for her love and affection. She devoted maximum time in taking care that I am provided with all the necessities on time so that my studies do not suffer at all. Finally I am happy to acknowledge my husband Sunny Sandhir who supported and inspired me during the awful phases of my life and shared happiness during the good times.

The financial assistance in the form of fellowship from Department of Research and technology (DST) is gratefully acknowledged.

Patiala

December, 2014. (Kirandeep Sandhu)

List of Publications

I. International Journals:

1. Fusion-evaporation residue as a dynamical decay process in the ^{48}Ca+^{249}Bk$\rightarrow^{297}$117* reaction, **Kirandeep Sandhu**, Manoj K. Sharma and Raj K. Gupta, Physical Review C **85**, 024604 (2012).

2. Deformation and orientation effects in the decay of ^{268}Sg* formed in a ^{30}Si-induced reaction across the Coulomb barrier, **Kirandeep Sandhu**, Manoj K. Sharma and Raj K. Gupta, Physical Review C **86**, 064611 (2012).

3. Fusion-evaporation residues and α-decay chains of the superheavy element Z=115 formed in the ^{243}Am+^{48}Ca reaction using the dynamical cluster-decay model, Raj Kumar, **Kirandeep Sandhu**, Manoj K. Sharma and Raj K. Gupta, Physical Review C **87**, 054610 (2013).

4. Decay and related stability aspects of the $^{266}_{104}$Rf* nucleus formed in the ^{18}O+^{248}Cm reaction, **Kirandeep Sandhu**, Manoj K. Sharma, Amandeep Kaur and Raj K. Gupta, Physical Review C **90**, 034610 (2014).

5. Dynamics of ^{40,48}Ca+^{238}U$\rightarrow^{278,286}$112* reactions across the Coulomb barrier using dynamical cluster decay model, **Kirandeep Sandhu**, Gurvinder Kaur and Manoj K. Sharma, Nuclear Physics A **921**, 114 (2014).

6. Role of nuclear deformations and proximity interactions in heavy particle radioactivity, Gudveen Sahwney, **Kirandeep Sandhu**, Manoj K. Sharma and Raj K. Gupta, European Physics Journal A **50**, 175 (2014).

7. Decay mechanism of $^{290,292}114^{*}$ superheavy nuclei formed in ^{48}Ca-induced reactions, **Kirandeep Sandhu** and Manoj K. Sharma, Brazilian Journal of Physics **44**, 64 (2014).

8. Probing nuclear matter at the extremes through application of dynamical cluster-decay model to superheavy nuclei, Niyti, Manoj K. Sharma, **Kirandeep Sandhu**, Sahila Chopra and Raj K. Gupta, Int. Rev. of Phys. IREPHY, Vol. 8, No. 3, 86 (2014) .

9. Stability aspect of superheavy nucleus $^{296}116^{*}$ formed in ^{48}Ca+^{248}Cm reaction, **Kirandeep Sandhu** and Manoj K. Sharma, AIP Conference Proceedings **1524**, 123 (2013).

10. Study of the decay of $^{291}115^{*}$ formed in ^{48}Ca+^{243}Am reaction, Raj Kumar, Manoj K. Sharma, **Kirandeep Sandhu** and Raj K. Gupta, EPJ Web of Conferences **66**, 03050 (2014).

11. Role of rotational energy and deformations in the dynamics of ^{6}Li+^{90}Zr reaction, Gurvinder Kaur, Neha Grover, **Kirandeep Sandhu** and Manoj K. Sharma, Nuclear Physics A **927**, 232 (2014).

12. Deformations and orientations effects in heavy particle radioactivity of Z=115, Gudveen Sahwney, **Kirandeep Sandhu**, Manoj K. Sharma and Raj K. Gupta, EPJ Web of Conferences, **66**, 03050 (2014).

****

II. In Conferences, Symposiums and Workshops:

1. Evaporation residue cross-sections of ^{249}Bk+ ^{48}Ca$\rightarrow^{297}$117* reaction, **Kirandeep Sandhu**, Manoj K. Sharma and Raj K. Gupta, *Proceedings of DAE Symposium on Nuclear Physics*, Andhra University, Vishakhapatnam, Vol. **56**, 528 (2011).

2. Isotopic analysis of superheavy nucleus Z=114, **Kirandeep Sandhu** and Manoj K. Sharma, *Proceedings of DAE symposium on Nuclear Physics*, Delhi University, Delhi, Vol. **57**, 500 (2012).

3. Decay of Z=112 isotopes and related orientation effects across the Coulomb barrier, **Kirandeep Sandhu** and Manoj K. Sharma, *Proceedings of DAE symposium on Nuclear Physics*, BARC, Mumbai, Vol. **58**, 412 (2013).

4. Decay of ^{290}114* nucleus formed in the heavy ion reaction involving radioactive target, **Kirandeep Sandhu** and Manoj K. Sharma, 2nd national conference on advanced materials and radiation physics (AMRP-2011), SLIET, Longowal (2011).

5. ^{208}Pb daughter radioactivity in ^{294}117 superheavy nucleus, Gudveen Sahwney, **Kirandeep Sandhu**, Manoj K. Sharma and Raj K. Gupta, 3rd national conference on advanced materials and radiation physics (AMRP-2013), Pg-84 RP(P)-14, SLIET, Longowal (2013).

6. Production of ^{260,261,262}Rf isotopes in ^{248}Cm+^{18}O reaction and the associated nuclear phenomena, **Kirandeep Sandhu**, Manoj K. Sharma and Raj K. Gupta, *Proceedings of 75 years of nuclear fission*, Pg. 88. (2014).

7. Role of short and long range interactions in $4n$-decay channel of ^{266}Rf* nucleus, **Kirandeep Sandhu**, Manoj K. Sharma, Amandeep Kaur and Raj K. Gupta, *Proceedings of DAE symposium on Nuclear Physics*, BHU, Banaras, Vol. **59**, 466 (2014).

Contents

Abstract **1**

1 Introduction **6**

1.1 Formation and stability of SH nuclei 9

1.1.1 Cold Fusion 11

1.1.2 Hot fusion 12

1.2 Role of deformations and orientations 13

1.3 Decay patterns of superheavy nuclei 15

1.3.1 Neutron evaporation 16

1.3.2 Fusion-fission and quasi-fission 17

1.3.3 Alpha (α)- decay 18

1.3.4 Heavy particle radioactivity (HPR) 20

1.4 Organization of thesis 21

Bibliography **25**

2 Methodology **31**

2.1 Introduction 31

2.2 The Fragmentation potential $V(\eta)$ 35

2.2.1 Binding energies B_i's 38

2.2.2 The Coulomb potential . . . 41
2.2.3 The Proximity Potential for deformed, oriented nuclei . . . 42
2.2.4 Rotational Energy due to angular momentum . . . 46
2.3 Scattering Potential $V(R)$ . . . 47
2.4 The Preformed Cluster Model . . . 47
2.4.1 Preformation probability P_0 . . . 49
2.4.2 Penetration probability P . . . 49
2.5 The Dynamical Cluster Decay Model . . . 52
2.5.1 Preformation probability P_0^ℓ . . . 54
2.5.2 Penetration probability P_ℓ . . . 54
2.5.3 The neck -length parameter and concept of "barrier lowering" . . . 56

Bibliography **58**

3 Neutron-evaporation and magicity effects in the SH-region **64**
3.1 Introduction . . . 65
3.2 Calculations and Results . . . 66
3.3 Summary . . . 76

Bibliography **78**

4 Alpha(α)-decay and heavy particle radioactivity (HPR) **80**
4.1 Introduction . . . 81
4.2 Calculations and Results . . . 83
4.2.1 Neutron evaporation cross-sections of $^{291}115^*$ CN . . . 84
4.2.2 α-decay chains of $^{291}115^*$-xn using the PCM . . . 86

4.2.3 Heavy particle radioactivity of Z=113, 115 and 117 superheavy isotopes . . . 88
4.3 Summary . . . 94

Bibliography **96**

5 Orientation effects across the Coulomb barrier **99**
5.1 Introduction . . . 100
5.2 Calculations and Results . . . 101
5.3 Summary . . . 108

Bibliography **110**

6 Role of higher order deformations and isotopic dependence **111**
6.1 Introduction . . . 112
6.2 Calculations and Results . . . 113
6.2.1 Role of higher order deformations . . . 114
6.2.2 Role of isospin in the decay of Z=112, 114 and 115 superheavy isotopes 116
6.3 Summary . . . 123

Bibliography **125**

7 Summary and outlook **127**

List of Figures

1.1 The variation of fission barrier heights as a function of the fissility parameter [3]. The black points are the experimental data, solid line represents the calculations through liquid-drop model used by [4]. 7

1.2 The nuclear landscape, showing superheavy elements with stability marked around Z=114, 120 and N=184, taken from [9]. 8

1.3 Schematic diagram for deformed orientated nuclei representing (a) the equatorial interaction leading to compact nuclear configuration, observed for the above barrier energies and (b) polar interaction leading to elongated nuclear configuration associated with below or sub barrier region. 15

2.1 Flowchart representing the basic structure of Preformed cluster model (PCM) [6]- [10] and Dynamical cluster decay model (DCM) [11]- [24]. . . . 36

2.2 Schematic configurations of two axially symmetric deformed, oriented nuclei, lying in the same plane and for various θ_1 and θ_2 values in the range 0^0 to 180^0 [32]. The θ's are measured anticlockwise direction from the colliding axis and the angle α's in clockwise from the symmetry axis. . . . 38

2.3 A scattering potential, used in the PCM, for α- decay of $^{289}115 \rightarrow {}^{285}113 + \alpha$ [24] at $\ell = 0$, including deformations upto β_{2i}. The path of barrier tunnelling is also shown. 50

2.4 The scattering potential for $^{291}115^{*} \rightarrow ^{289}115+2n$ reaction at E^{*}_{CN} =33.37 MeV, calculated at the extreme values of angular momentum. The "barrier lowering parameter" is also shown for ℓ=ℓ_{min} and ℓ=ℓ_{max} values [24]. . . . 56

3.1 (a) Comparison of fragmentation potential as a function of light fragment mass for three choices of magic numbers Z=126, 120, 114 and N=184, same value of ΔR is taken for all the magic shell cases. (b) Measured and calculated $3n$-cross-sections as function of proton magic numbers. Calculations are done for three set of magic pairs, using sticking (I_S) moment of inertia. In each panel, the ΔR is kept same for the remaining two cases. 67

3.2 Variation of fragmentation potential as a function of angular momentum, using non-sticking moment of inertia (I_{NS}) for (a) $4n$, (b) $5n$ and (c) $6n$ decay channels, at different E_{lab} energies, using Z=126, 120, 114 and N=184 magic shell pairs. 68

3.3 Variation of preformation probability (P_0) as a function of light fragment mass at $\ell = \ell_{min}$ for Z=126, 120, 114 and N=184 magic pairs at (a) 88.2 MeV (b) 94.8 MeV and (c) 101.3 MeV beam energies for the decay of ^{266}Rf* nucleus. For all the three cases of magic pairs, the magnitude of ΔR is taken same. 69

3.4 Fragmentation potentials for the decay of $^{297}117^{*}$ compound nucleus as a function of light fragment mass (A_2) for spherical and β_{2i}-deformed case at ℓ_{max} values. The fragmentation path is plotted at the neck length (ΔR) parameters of $2n$, $3n$ and $4n$ decay channels, fitted for the deformed case. . 70

3.5 Same as Fig 3.4, but for only deformed and oriented nuclei at ℓ=0 and ℓ_{max} values, and for ^{4}He decay channel also. 71

3.6 (a) The variation of preformation probability (P_0) with angular momentum (ℓ) in the reaction ^{48}Ca+^{249}Bk$\rightarrow^{297}$117*, for the case with effects of deformations and orientations included. (b) Same as (a), but for the WKB penetration probability (P). 72

3.7 Channel cross-section (σ_{xn}) plotted as the function of angular momentum (ℓ). The minimum and maximum angular momentum values ℓ_{min} and ℓ_{max}, respectively, illustrated for $4n$-decay channel. 73

3.8 Total DCM calculated cross-sections σ_{3n} and σ_{4n+^4He} for the decay of ^{297}117*, plotted as the function of E^*_{CN}, and compared with experimental data [11]. The lower limits of data are shown by downwards arrows. . . 74

3.9 (a) Variation of ΔV_B as a function of E^*_{CN} for the xn decay of ^{297}117*, for $\ell = \ell_{max}$ case.(b) Variation of ΔV_B as function of ℓ for (b_1) $3n$ decay at E^*_{CN}=35.3 MeV, and (b_2) $4n$ decay at E^*_{CN}=39.3 MeV. 76

4.1 Preformation probability for the decay of ^{291}115* compound system formed in the ^{48}Ca+^{243}Am reaction for spherical and deformed choices of fragments with optimum hot orientations ($\theta_i^{opt.}$) at E^*_{CN}=33.37 MeV and respective ℓ_{max}-values. The deformations are taken up to quadrupole (β_{2i}), with both the static and dynamic choices. 84

4.2 Calculated cross- sections for $2n$, $3n$ and $4n$ evaporation channels of the ^{48}Ca+^{243}Am reaction as a function of E^*_{CN}, compared with experimental data [15]. The error bars are also shown. The deformations are up to β_{2i}, along with optimum hot orientations. The Bass barrier [24] is also shown as a downward arrow. The dashed line is to guide the eye. 85

4.3 Variation of the neck-length parameter (ΔR) with E^*_{CN}, obtained for the best fit to neutron fusion-evaporation data [15] for the ^{48}Ca+^{243}Am reaction, using the DCM. The inset shows the comparison of neck-lengths of the $2n$ channel for spherical and deformed choices of nuclei. 86

4.4 Comparison of experimental and PCM calculated half-lives of α-decay chains from (a) $2n$ (b) $3n$ and (c) $4n$-decay channels of $^{291}115^*$ formed in the ^{48}Ca+^{243}Am reaction. The hot optimum orientations are used with in the framework of the PCM. 87

4.5 Fragmentation potential for the parent nucleus $^{294}117$ using proximity potentials Prox-77 and Prox-00 for β_{2i} deformed choice of nuclei with optimum (θ_i^{opt}) orientations forming hot compact (filled symbols) and cold elongated (open symbols) configuration, taking into account all possible fragments. . 89

4.6 Preformation probability (P_0) for the decay of $^{278}113$, $^{289}115$ and $^{294}117$ nuclei using nuclear potentials Prox-77 and Prox-00 for spherical [panels (a), (c), and (e)] and deformed [panels (b), (d) and (f)] choices of nuclei. The most probable cluster corresponding to Pb daughter is pointed out with solid lines. 90

4.7 PCM predicted decay half-lives for the most probable cluster emitted from $^{278}113$, $^{287-289}115$ and $^{293,294}117$ isotopes over a range of neck-length parameter (ΔR) for the use of β_{2i}-deformed decay products. 92

4.8 (a) Role of shell corrections δU, illustrated for ^{289}115 by plotting the preformation factor (P_0) as a function of both the cluster and daughter masses, using Z=126 and N=184. (b) The same as (a), plotted by considering the different magic shell closures Z=126, 120, 114 and N=184 for the use of Prox-00. ΔR=0.98 fm, having kept the same in all the three cases for comparison. 93

5.1 (a) Fragmentation potential for the ^{30}Si+^{238}U$\rightarrow^{268}$Sg* reaction as a function of light fragment mass for spherical, β_{2i} -static and dynamic deformations with "optimum" orientations (θ_i^{opt}) at ℓ_{max} values. (b) Same as that of (a) but plotted for the preformation probability. 101

5.2 DCM calculated fission cross-sections for the decay of ^{268}Sg* (in hot equatorial and cold polar configurations), plotted as the function of $E_{c.m.}$, compared with the experimental data of Ref. [2]. 104

5.3 Variation of fragmentation potential V (MeV) as a function of light fragment mass (A_2) for the decay of ^{268}Sg* CN, using hot-compact and cold non-compact configurations. 105

5.4 Preformation probability (P_0) for the ^{30}Si+^{238}U$\rightarrow^{268}$Sg* reaction varies as a function of fragment mass number at highest value of angular momentum (ℓ_{max}), for the neck length parameter (ΔR) fitted to the case of deformed nuclei. 106

5.5 Variation of ΔV_B as function of angular momentum (ℓ) for the decay of the compound nucleus ^{268}Sg*, considering the hot compact and cold non-compact configurations, respectively at $E_{c.m.}$=169 MeV and $E_{c.m.}$=129 MeV. 107

5.6 Variation of barrier height (V_B) as function of fragment mass (A_2) for the decay of $^{268}Sg^*$ compound nucleus, using hot equatorial and cold polar configurations, at different values of angular momentum (ℓ). 108

6.1 (a ,b) Barrier height plotted as a function of orientation angle (θ_i) for $^{40,48}Ca+^{238}U\rightarrow^{278,286}112^*$ reactions at $E_{c.m.}$=230 MeV and 180 MeV respectively. (c, d) Same as above figures, but for barrier position. 114

6.2 Comparative analysis of fragmentation potentials for $^{40,48}Ca+^{238}U\rightarrow^{278,286}112^*$ reactions as a function of light fragment mass (A_2) for (a) spherical (b) β_{2i}-static with "optimum" orientations (θ_i^{opt}) and (c) β_{4i}-static with "compact" orientations (θ_i^c) at ℓ_{max} values, calculated at energy $E_{c.m.}$=230 MeV, using hot equatorial configuration. 115

6.3 Plot of preformation probability varies with fragment mass for symmetric fission channels of $^{40,48}Ca+^{238}U\rightarrow^{278,286}112^*$ reactions at (a,b) $E_{c.m.}$ =230 MeV and (c,d) 180 MeV, using hot equatorial configuration and (e,f) $E_{c.m.}$ =180 MeV with cold polar configuration. 117

6.4 Preformation probability as a function of symmetric fragment's atomic number for the decay of $^{278,286}112^*$ compound nuclei associated with (a,b,c,d) equatorial and (e,f) polar configurations, (*the mass numbers of decaying fragments are shown within for each atomic number*). 119

6.5 Fragmentation potentials for $^{48}Ca+^{242,244}Pu\rightarrow^{290,292}114^*$ reactions as a function of light fragment mass (A_2) with β_{2i} deformations and "optimum" orientations (θ_i^{opt}) at $\ell = 0$ and ℓ_{max} values. 120

6.6 (a) Fragmentation potential and (b) preformation probability for Z=114 isotopes at neck-length parameter of $3n$ neutron-evaporation channel using β_{2i}-deformations and optimum orientations (θ_i^{opt}) at $\ell = \ell_{max}$. 121

List of Tables

3.1 Experimental and DCM calculated evaporation residue cross-sections σ_{xn}, x=2, 3 and 4, in the decay of $^{297}117^{*}$ formed in the ^{48}Ca+^{249}Bk reaction, compared with other available results. 75

4.1 The experimental and PCM calculated half-lives ($T_{1/2}$), together with the corresponding preformation probability (P_0), penetrability (P), impinging frequency (ν_0), neck-length parameter (ΔR), and Q-values ($Q_{out.}$) [21] for the α-decay chains after $2n$, $3n$ and $4n$ decays of $^{291}115^{*}$ formed in the ^{48}Ca+^{243}Am reaction. 88

5.1 Experimental and DCM calculated evaporation residue cross-sections (σ_{xn}, x= 3, 4 and 5) of ^{268}Sg* CN, fitted for hot equatorial configuration. 103

5.2 Experimental and DCM calculated fission cross-sections ($\sigma_{fission}$) in the decay of ^{268}Sg* formed in the ^{30}Si+^{238}U reaction by considering hot equatorial configuration. 103

5.3 Experimental and DCM calculated fission cross-sections ($\sigma_{fission}$) in the decay of ^{268}Sg* formed in the ^{30}Si+^{238}U reaction by considering cold polar configuration. 104

6.1 The DCM calculated neutron evaporation residue cross-sections (σ_{xn}, x=2, 3 and 4), for the decay of $^{289}115^{*}$ and $^{293}115^{*}$ compound systems, formed in ^{48}Ca+^{241}Am and ^{48}Ca+^{245}Am reactions, respectively, at the same CN excitation energy and neck-length parameter as that of $^{291}115^{*}$. 122

Abstract

The aim of present work is to carry out an extensive theoretical investigation of the decay properties, and patterns of a variety of superheavy nuclear systems formed in heavy ion reactions. This investigation has been performed within the framework of Preformed cluster model (PCM) and Dynamical cluster decay model (DCM). The PCM is applied to understand the ground state decays such as α-emission and heavy particle radioactivity (HPR), whereas DCM is applied to account for the decay of hot (E$\neq$0) and rotating ($\ell\neq$0) nuclei formed in low energy heavy ion reactions. The deformation and orientation effects of nuclei are explicitly included in these formalisms. The thesis is organized into seven chapters and a brief outline of the work is given below.

Chapter 1 gives the general introduction related to present work, which includes the broad outline of experimental and theoretical developments related to the dynamics of hot and rotating compound nuclei in the superheavy mass region. A detailed discussion is made about the formation and decay processes of superheavy nuclei. The cold and hot fusion processes are described, which follows by various decay channels such as neutron evaporation, fusion-fission and quasi-fission. In addition to this, the ground state decays such as α-decay and heavy particle radioactivity (HPR) are also explained for overall understanding of nuclear dynamics in superheavy region. Besides this, the role of excitation energy, deformations and orientations are discussed in view of reaction dynamics governed

via heavy ion collisions.

Chapter 2 gives the details of the Preformed cluster model (PCM) and Dynamical cluster decay model (DCM) which are used to address the ground state and excited state decay patterns of nuclei. DCM is formulated from PCM (applied for ground state decays) by employing the temperature effects in its various interaction terms. Both models are based on the Quantum Mechanical Fragmentation Theory (QMFT). In this approach, the Schrödinger equation is solved in the mass asymmetry [η=(A_1-A_2)/(A_1+A_2)] co-ordinates to account for the probability of formation of decaying fragments at compound nucleus stage. Then the penetration probability of these preformed fragments is estimated using WKB approximation. The fragmentation potential which goes as input to solve the Schrödinger equation, is calculated as sum of binding energies, Coulomb interaction potential, proximity potential and angular momentum dependent potential. It may be noted that all the above terms in DCM are temperature dependent, whereas temperature and angular momentum effects are silent in the PCM. Besides this, the deformation and orientation effects are incorporated well within both formalisms. In DCM, the emission of light particles (LPs), intermediate mass fragments (IMFs) and fission fragments upto symmetric division of the compound nucleus, are treated on equal footings as the dynamical collective mass motions of preformed clusters or fragments through the barrier, in contrast to statistical models which follow different approaches for different processes. The ground state dynamics with PCM is also governed via collective clusterization process.

In **Chapter 3**, the decay of $^{266}Rf^{*}$ and $^{296}116^{*}$ superheavy nuclear systems formed in ^{18}O+^{248}Cm and ^{48}Ca+^{248}Cm reactions are studied using the Dynamical cluster decay model (DCM) to investigate the neutron proton magicity in superheavy mass region. The

calculations are carried out by using Z=114, 120, 126 and N=184 shell closures and the neutron evaporation data is addressed. The lower magnitude of the fragmentation potential and consequently higher values of preformation probability for Z=126 and N=184 magic pair, seem to suggest that Z=126 and N=184 are the best suited magic candidates to address the neutron evaporation residues. Using these magic shells, further in this chapter the evaporation residues of $^{297}117^{*}$ nucleus formed in ^{48}Ca+^{249}Bk are studied in the DCM framework. The $2n$, $3n$ and $4n$ cross-sections of $^{297}117^{*}$ are explored using the quadrupole (β_{2i}) deformations, as the spherical fragmentation approach could not address the data nicely. Even after inclusion of deformation effects, the $4n$ channel cross-sections are underestimated. Finally ^{4}He-decay contribution is added to $4n$-channel cross-sections which fits the data nicely. In addition to this, the fusion-fission component in the decay of $^{297}117^{*}$ compound nucleus is also predicted.

In **Chapter 4**, the decay of another odd mass superheavy nucleus $^{291}115^{*}$ formed in ^{48}Ca+^{243}Am reaction is studied over a wide range of compound nucleus energies using the Dynamical cluster decay model (DCM). The $2n$, $3n$ and $4n$ decay of $^{291}115^{*}$ superheavy nucleus is investigated and it is observed that the neutron cross-sections find nice agreement with an experimental data with the inclusion of quadrupole (β_{2i}) deformations and optimum orientations (θ_i^{opt}) of decaying fragments. The comparative analysis of spherical, β_{2i}-static and dynamic fragmentations is also carried out. Furthermore, the $2n$, $3n$ and $4n$ cross-sections are predicted at the bass barrier.

In addition to the neutron evaporation, the α-decay and heavy particle radioactivity (HPR) are also discussed in this chapter using the Preformed cluster model (PCM). Both mechanisms are investigated within the hot optimum orientation approach. The α- decay chains of $^{289}115$, $^{288}115$ and $^{287}115$ superheavy nuclei are studied by modifying the

penetration probability of the decaying alpha particle. On the other hand, the role of different proximity potentials such as Prox-77 and Prox-00 is studied to understand the heavy particle radioactivity of $^{278}113$, $^{287-289}115$ and $^{293,294}117$ superheavy nuclei.

In **Chapter 5**, the role of orientation degree of freedom is investigated in the dynamics of $^{268}Sg^{*}$ nucleus formed in ^{30}Si induced reaction over a wide range center of mass energies across the Coulomb barrier. Hot equatorial configuration is taken into account to address the fission cross-sections at above barrier energies. Nice fitting of data is obtained within this approach with the emergence of symmetric mass fragmentation. On contrary to this, at below/sub barrier energies asymmetric fragmentation is observed for the cold polar configuration. The asymmetric mass distribution leads to demonstrate the fact that quasi-fission may compete fusion-fission at sub-barrier energies. Also the inbuilt property of barrier lowering effect of DCM is estimated for both oriented configurations, and its magnitude is higher for the use of cold polar configuration as compared to the hot compact. In addition to the explicit role of orientations, at the highest center of mass energy, the comparative analysis of spherical, β_{2i}-static and dynamic deformations is carried out to understand the effect of deformations on the decay path of the $^{268}Sg^{*}$ nucleus.

In **Chapter 6**, the Dynamical cluster decay model (DCM) is applied to understand the effect of higher multipole deformations in reference to data on $^{40,48}Ca+^{238}U$ reactions at energies lying across the Coulomb barrier. The angle at which compact system is achieved, gets modified slightly with the inclusion hexadecapole deformation for $^{278,286}112^{*}$ nuclei. Also the effects of β_{4i} deformations along with β_{2i} and spherical considerations are investigated on the decay path of $^{278,286}112^{*}$ compound nuclei. In addition to this, isotopic analysis of $^{278,286}112^{*}$ nuclei is carried out by comparing the preformation probability of

the fission fragments at $E_{c.m.}$=180 and 230 MeV, using β_{2i}-deformations, for hot equatorial and cold elongated configurations of nuclei. Suppression in the preformation factor is observed while going from hot equatorial to cold polar configuration, and is observed more for $^{278}112^{*}$ compound nucleus as compared to $^{286}112^{*}$. The role of isospin is also observed for Z=114 isotopes by comparing the fragmentation and preformation profile of the $^{288,290,292,294}114^{*}$ nuclei at T$\sim$1.25 MeV. Different isotopes of Z=115 are also studied within the DCM framework by comparing the magnitudes of preformation probability, penetration probability and the neutron evaporation cross-sections of $^{289,291,293}115^{*}$ compound nuclei.

Finally, in **Chapter 7**, conclusions and an outlook of the work is presented.

Chapter 1

Introduction

After Becquerel had announced "the discovery of radioactivity" from Uranium minerals in 1896 [1]; the commencement of new discipline allowed the scientific community to envision a new era of nuclear physics. Plenty of radioactive elements were then discovered, all descended from the primordial U and Th. After this revolutionary epoch, nuclear scientists have ventured for the search of new heavy elements with an attempt to resolve the queries of partly fundamental character. Some of the important queries are: what is the limit on the existence of elements, how new elements can be synthesized, which property determines their stability, how long is the lifespan, etc. Neutron capture with successive β-decay was considered as the primary process to answer these questions and make it possible to climb up the periodic table element by element.

In the race of furtherance to achieve higher and higher atomic number, the extreme mass is the limitation for the production of new elements as the strong Coulomb force acting between protons dominates the nuclear stability. Consequently, the survival probability of newly synthesized nucleus becomes quite small and it may disintegrate via α-decay or fission. The liquid drop model [2] provided scrutiny of the retrospect on the basis of the saturation property and low compressibility of the nuclear matter thereby suggesting

the upper limit regarding the existence of heavy nuclei. According to this model [2], the limiting value for existence of the nuclei is located near Z∼100. In pursuit of this investigation, some peculiarities were also observed whose rationale was unanswered in the framework of liquid drop model.

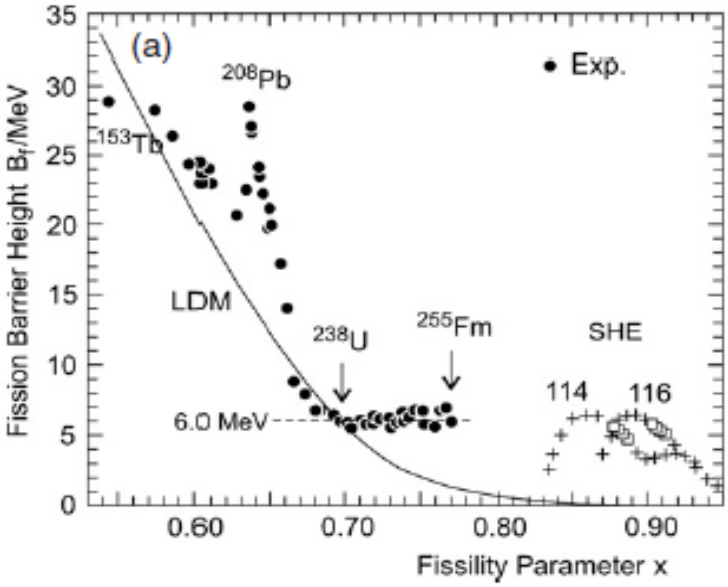

Figure 1.1 The variation of fission barrier heights as a function of the fissility parameter [3]. The black points are the experimental data, solid line represents the calculations through liquid-drop model used by [4].

For example, in reference to the fission barrier heights depicted in Fig. 1.1, one may concentrate on the following observations of [3, 5] (i) there is a strong disagreement in the experimental and theoretical (LDM) estimates of fission barrier heights. (ii) barrier height of ^{208}Pb and neighboring nuclei is significantly large, (iii) the fission barrier heights of actinide isotopes varying from U to Fm are almost constant. Since then, it has been realized that the preconceived knowledge about the stability of the heavy nuclei is not sufficient to locate the island of stability, suggested by Glenn T. Seaborg [6] in the late sixties.

The properties of nuclei are not smooth function of protons and neutrons, hence show

non-uniformities as depicted from the Fig. 1.1. This investigation calls for understanding of the completely different aspect of the nucleus, in which nucleons are considered to behave as independent particles. In 1949, Mayer and Jensen introduced the concept of spin-orbit interaction, based upon which the shell model [7, 8] was proposed. The model predicted unexpected gaps in the single particle level distribution corresponding to magic proton or neutron shells at 2, 8, 20, 28, 50, 82 and 126. The stability of nuclei with the so-called closed proton and neutron shells counteracts the repelling Coulomb forces. The important consequence of this observation provides the possibility of the existence of elements far beyond the transuranium region. Subsequent to this, an island of stability was proposed (shown in Fig. 1.2), located around proton number 114 and 120 or 126 with neutron number 184. For these magic shell closures, the word "Superheavy" was coined. With this, new horizons in the nuclear physics are unlocked and intensive theoretical/experimental studies are being made in this field at different scientific centers of the world.

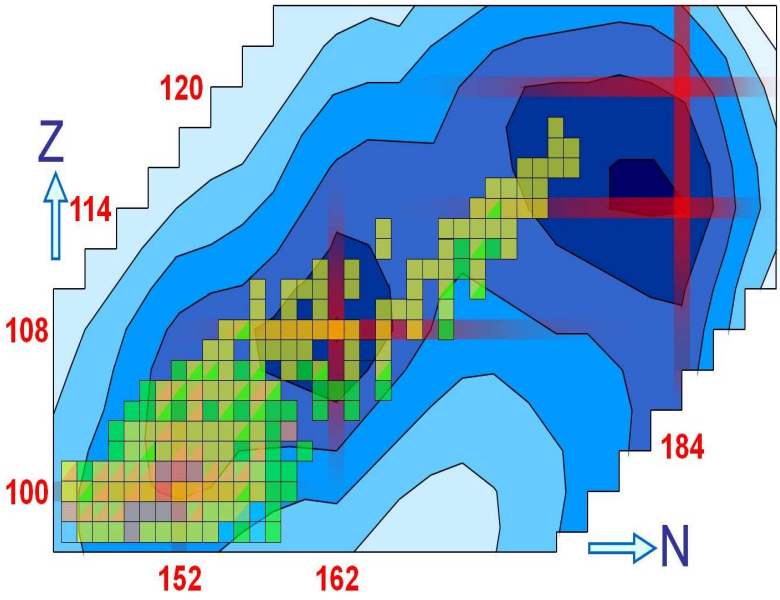

Figure 1.2 The nuclear landscape, showing superheavy elements with stability marked around Z=114, 120 and N=184, taken from [9].

1.1 Formation and stability of SH nuclei

With foundation of the shell model, a macroscopic-microscopic theory was developed, which is based on an assumption that the total energy of the nucleus can be decomposed into two parts E=E_{marco}+ E_{micro}, where E_{marco} corresponds to the liquid drop energy and E_{micro} is the microscopic energy, calculated using the Nilsson or Wood-Saxon single particle potential [10]. The main achievement of macro-microscopic theory was the development of a method to calculate the shell-corrections for the ground and highly deformed states. Most of the calculations based upon the macro-microscopic approach disclosed the gap in the superheavy region at N=184 with some evidences of proton shell closure at Z=114. These shell closures had found support in the models [11, 12] based on the Strutinsky shell correction method [10].

Parallel to macro-microscopic approach, the microscopic interactions were developed based on the Hartee-Fock approximation with Skyrme (SHF) [13,14] or Gogny interactions [15] and relativistic mean field (RMF) models [16], which find their genesis in the self-consistent mean field theories. The SHF and RMF interactions rely on a theoretically motivated and phenomenologically adjusted energy density functional. Although both the formalisms have been used extensively, but the macro-microscopic method is preferred to extrapolate the properties of the nuclei to a nearby neighborhood [17] as the parameter sets are improved continuously in accordance with the experimental data. On the other hand, for extrapolation to the region far from nuclear stability, the different self-consistent mean field models provide better description of nuclear behavior [17].

The Skyrme Hartee-Fock approximation is the first class of non relativistic self consistent mean field theories in which two body interaction was introduced. Using definite parametrization, the Skyrme Hartee-Fock with the parameter sets of SkI3 and SkI4 predicted Z=120 and 184 magic pair for the superheavy elements. However Hartee-Fock Bo-

goliubov calculations with finite range Gogny force suggested Z=120, 126 and N=172, 184 as the possible shell closures [18]. The applicability of these formalisms is also extended to estimate the transition probabilities, static quadrupole moments and yrast spectra [19,20] of various nuclei. The second class of self-consistent mean field theories is based on the relativistic mean field (RMF) models, using this Rutz *et al.* [14] predicted the Z=120 and N=172 as the next possible magic shells in spherical RMF theory. Meanwhile, Patra *et al.* [21] had applied axially deformed RMF theory, and predicted Z=120 and N=172 or 184 as the magic candidates for the superheavy mass region. Hence in general, the nuclear physicists working in the area of superheavy synthesis have two fold aim (i) to understand the unexpected nuclear structural effects of massive nuclei, (ii) use this structural stability aspect to govern the evident prediction of stable superheavy nuclei with spherical shell closures at proton number Z=114, 120, 126 and neutron number N=172 or 184.

Similar attempt is also made within the Dynamical cluster-decay model (DCM) [22]-[32], based upon the Quantum Mechanical Fragmentation Theory (QMFT) [33,34]. Niyti *et al.* investigated $^{286}112^{*}$ [35] nuclear system in the DCM framework and concluded that Z=126, N=184 and Z=120, N=184 are the best suited superheavy shell closures to advocate the evaporation channels and the fusion-fission dynamics respectively. Thereafter, we generalized the above results for wider range of the superheavy mass region by understanding the decay of $^{266}\mathrm{Rf}^{*}$ [29] and $^{296}116^{*}$ [30] using the proposed magic shell closures.

Having no consensus among the nuclear community about the center of stability, the outreach of SHE towards the superheavy landscape (shown in Fig. 1.2.) is one of the most sorted aspects in today's context. The constant increase of the Coulomb repulsion with increment in the atomic number of the nuclei restricts the production rates of superheavy elements. The first attempt to penetrate the region of SHE was undertaken using neutron

capture reactions [36], however this technique was not explored much because the superheavy nucleus formed in this process decays before the capture of subsequent neutron. Consequently the theoreticians and experimentalists jumped onto the heavy-ion induced reactions which demand significant improvement in the experimental setups and available theoretical methodologies. The developments in the laboratories of Berkely (LBNL), Dubna (JINR), Japan (RIKEN) and Germany (GSI) had overturned the synthesis process of superheavy nuclei within last two decades by introducing the extremely different techniques of production known as "cluster-based cold fusion" and "actinide-based hot fusion" processes. A brief description of these concepts is given in subsequent sections.

1.1.1 Cold Fusion

As superheavy isotopes were born out of nuclear structural effects, their evolution was leadingly associated with "cluster-based fusion" which was later surpassed with actinide targets induced fusion. In the cluster based fusion, collision of ^{208}Pb and ^{209}Bi targets with the medium mass neutron-rich projectiles such as ^{54}Cr to ^{70}Zn leads to the formation of low-excited superheavy compound nucleus in the energy range E^*_{CN}=10-20 MeV (near barrier energies) and the process is termed as "cold fusion". As a consequence of low excitation energy, the survivability of the compound nucleus increases because the transition to the ground state is mainly associated with the emission of one/two neutron(s) or gamma rays. This is the main advantage of using cold fusion reactions. Hence with this process the six heavy isotopes of superheavy elements Z=107-112 were synthesized [37–39] in various laboratories.

In spite of the favorable fact (one/two neutron(s) emission), the further advancement towards the center of 'island of stability' with higher Ga and Ge beams seems problematic due to which the synthesis of superheavy isotopes via cold fusion is limited up to Z=113.

Actually, the forecasts regarding synthesis of heavier nuclei using cold fusion process are not very optimistic because of the following reasons: there exists sharp decrease in cross-section with increase in charge number of the projectile [37]. (ii) the neutron deficient evaporation products are obtained, far from the closed shells or sub-shells of superheavy region. Hence for the synthesis of nuclei with Z≥113, the usually preferred cold fusion approach is supplemented with "Hot fusion" process in quest of regarding the island of stability in superheavy region.

1.1.2 Hot fusion

To compensate for the factors hindering fusion, the use of asymmetric reactions having actinide targets were suggested to extend the periodic table towards the superheavy mass region. The supremacy of charge asymmetry between the beam and the target nucleus provides an advantage of low Coulomb repulsion in the entrance channel which inturn governs high fusion probability. For example, the magnitude of Coulomb repulsion in ^{48}Ca+^{244}Pu reaction forming ^{292}114* compound nucleus is about $Z_p * Z_t$=1880 which increases 40 % with the use of cold fusion reaction synthesis via ^{76}Ge+^{208}Pb [5]. Hence the former reaction is more acceptable for the formation of Z=114 isotopes. In comparison to cold fusion reactions, the excitation energy for actinide based reactions is usually higher within the range of 30-50 MeV, for which the compound nucleus de-excites with the emission of more than 2 neutrons. This kind of synthesis is termed as "hot fusion" reaction. The higher energy range for the hot fusion reaction is the consequence of weaker binding energies of actinide targets. To compensate such high energies above the Coulomb barrier, doubly magic ^{48}Ca projectile [40,41] is preferred which may produce the compound nuclei with ∼10 MeV less excitation energy [37]. Hence ^{48}Ca+ actinide targets such as ^{238}U [42], ^{242,244}Pu [42–44], ^{243}Am [45], ^{248}Cm [42, 46], ^{249}Cf [47], ^{249}Bk [48] are the signature

reactions for producing the superheavy isotopes in the hot fusion process. Neutron excess in the evaporation residues lying closer to the predicted summit of the superheavy island is another asset of using hot fusion reactions. For example, the compound nucleus formed in ^{48}Ca+^{244}Pu reaction has eight additional neutrons as compared to the cold fusion product formed in ^{76}Ge+^{208}Pb reaction. These eight neutrons play a vital role in the production of the superheavy nucleus, closer to the island of stability [5]. Precisely, the quest to attain the magicity near to N=184 to have high fission barriers, ascends the ladder of SHEs gradually by hot fusion of colliding nuclei. With this, plenty of isotopes were discovered from Z=112 to 118 [42]- [48].

In spite of the pioneer of the reaction synthesis, the understanding of hot fusion reaction dynamics is not so easy. Unlike cold fusion reaction partners, the collision in the hot fusion process requires the addressal of preferred orientations as the actinide targets are prolate deformed. So, to have the complete dynamics of the reactions in picture, one has to understand the role of deformations and orientations in the formation and decay of the compound nuclei formed in heavy ion reactions.

1.2 Role of deformations and orientations

The knowledge of substantial comprehension of the extreme shapes, the higher multipole deformations (described by the usual deformation parameters , β_{λ_i} (λ=2, 3, 4)) and the extreme proton to neutron ratio are eminently useful to have an overall systematics of the heavy ion induced reactions. Particularly in the superheavy element synthesis, where the interaction potential plays important role due to dominating Coulomb forces, the deformed oriented nuclei undergo an additional degree of freedom to uplift their stability. The low fusion barriers for actinide (prolate deformed) based reactions in comparison to

Pb and Bi induced reactions elucidate the significance of the deformations on the interaction of the reaction partners. The decaying scenario is also affected significantly with the inclusion of deformations in the superheavy mass region. From the DCM point of view, mostly asymmetric mass fragmentation is obtained in heavy mass fragment (HMF) region, for deformed choice [26, 28, 32]. On the other hand, the potential energy surfaces (PES) for the spherical case indicate symmetric mass distribution of the decaying fragments. Also relatively more structural changes are observed in the decay path of the superheavy compound nucleus, with the inclusion of deformation effects which otherwise remain smooth for the spherical fragmentation approach. The relevant importance of the deformations on the decay path is shown for $^{297}117^{*}$ [26] and $^{291}115^{*}$ [28] superheavy nuclei, discussed in chapter 3 and 4.

Besides deformation effects, another parameter that influences the fusion probability is the relative orientation of the deformed nuclei which changes the barrier height and distance between the centers of colliding nuclei. In early 1980's, this study got triggered off by Greiner [49] while understanding the ^{238}U+ ^{238}U collision dynamics, where a particular orientation of ^{238}U nucleus could lead to a very long lived giant molecule. On the basis of this study, one may observe that high fusion probability is restricted only by certain orientations of the reaction partners, as particular inclination of the actinide target leads to the most compact starting configuration on way to the compound nucleus formation [50]. When two nuclei touch each other in the above barrier regime by their lateral surfaces (near-side collisions), shown in Fig. 1.3(a), high formation probability of the compact composite system is expected. On the other hand, the elongated configuration of the dinuclear system can be visualized in the sub-barrier region [50], when the interaction is along the polar axis of the collision geometry (represented in Fig 1.3(b)). Hence the importance of deformed oriented nuclei for the synthesis of superheavy nuclei is clear from

the interaction scenario, based upon which the above and below barrier reaction dynamics can be distinguished.

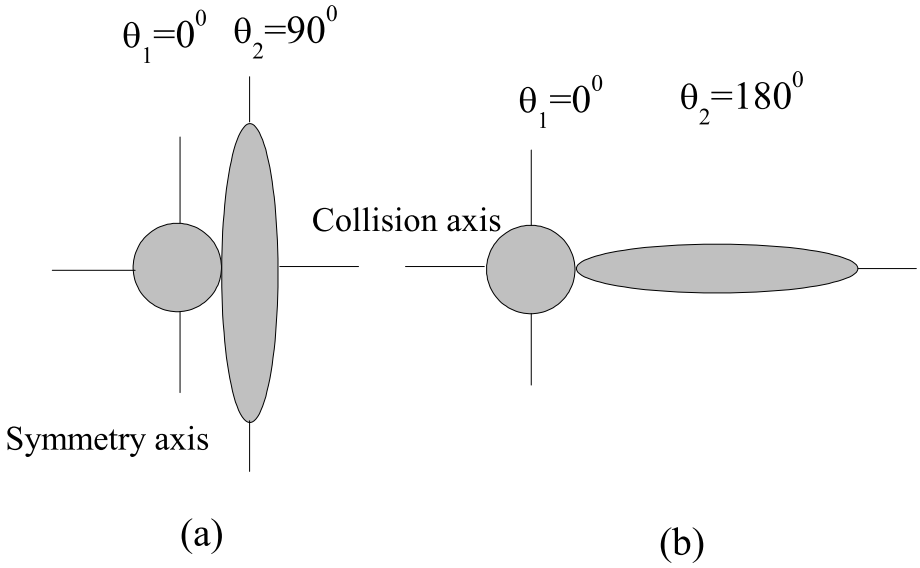

Figure 1.3 Schematic diagram for deformed orientated nuclei representing (a) the equatorial interaction leading to compact nuclear configuration, observed for the above barrier energies and (b) polar interaction leading to elongated nuclear configuration associated with below or sub barrier region.

Such compact and elongated structures in the Dynamical cluster decay model (DCM) [22]- [32] was addressed recently on the basis of the ± signs of the quadrupole deformations [22,23]. The optimum orientations are suggested for cold, non-compact and hot, compact configurations shown in Fig. 1.3, corresponding to the largest interaction radius/lower barrier and the smallest interaction radius/highest barrier respectively.

1.3 Decay patterns of superheavy nuclei

When a projectile nucleus interacts with a heavy target, there are several possible outcomes and/or mechanisms that come into picture such as particle evaporation, fusion-fission and quasi-fission etc. In case the fused dinuclear system forms a compact, mononu-

clear configuration, equilibrated in all degrees of freedom, then compound nucleus stage is perceived which usually disintegrates via neutron evaporation and fusion -fission processes. On the other hand, there might be a possibility that the re-separation of the reaction partners occurs before forming an equilibrated composite state. Such non-compound nucleus decay phenomenon may be termed as quasi-fission (QF) and deep inelastic collision (DIC).

Superheavy nuclei are usually produced via evaporation of neutrons from the compound nucleus with competing fusion-fission and quasi-fission/DIC channels. The nuclei thus obtained are unstable having the lifetime of an order of few seconds. With such a small lifespan they further disintegrate by themselves following the path of α-decay chain and spontaneous fission, which are considered as the main residual decay modes of the superheavy nuclei. The commonly observed excited as well as the ground state decay mechanisms are explained in the following discussion.

1.3.1 Neutron evaporation

From the fully equilibrated compound nucleus, light particle emission (in the form of neutron evaporation) is the main decay channel for the production of superheavy nuclei. The superheavy compound nuclear systems formed via heavy ion interactions emit neutrons and γ -rays for lowering the excitation energy and subsequently forming the residual nucleus. Thus, the emission of neutrons and γ -rays inturn convert the excited nuclear system in relatively stable form. For the cold fusion process, the de-excitation of the compound nucleus takes place through $1n$ and $2n$ emission as the excitation energies involved within this process are low. However due to high excitation energy, the compound nuclei with Z_{CN}=112-118, formed in hot processes release their energy by a cascade emission of 2-5 neutrons. This process in general competes with usual fusion-fission dynamics. Broadly speaking, the survival probability of an excited nucleus is decided on the basis of

emitted neutrons and γ -rays in competition with the fission.

Following neutron evaporation, a large number of superheavy isotopes have been synthesized. Some of the recent investigations [43, 45, 48] have been addressed using the Dynamical cluster decay model (DCM). Specifically an extensive analysis is carried out for Z=117, 116, 115, 114, 106 and 104 nuclei in the framework of DCM through collective clusterization technique in which the preformation probability (P_0), penetration probability (P) and the fragmentation potential (V_η) of decay fragments provide nice description of the emitted neutron clusters and complementary heavy fragments. In addition to this, DCM calculations also suggest the reaction time for the emission of neutron clusters on the basis of the neck formation effects.

1.3.2 Fusion-fission and quasi-fission

In heavy ion induced reactions, the fusion-fission and quasi-fission are the major competing decay processes. The clarification of these mechanisms is extremely desirable to understand the superheavy reaction dynamics. Elaborating this, the superheavy compound nucleus (CN) synthesis is generally hindered by the quasi-fission process because the colliding nuclei do not evolve inside the fission saddle, but re-separate after nucleon transfer. On the other hand, after full momentum transfer, if the entrance channel evolves inside the fission saddle point, the fusion-fission phenomenon may occur. The balance between these processes strongly depends on certain factors such as excitation energy, deformations/orientations of incoming or outgoing partners, mass asymmetry of entrance channel and the Coulomb barrier Z_1Z_2.

The fusion-fission process is generally observed for above barrier energies where the projectile nucleus has sufficient energy to overcome the Coulomb barrier, hence form the compact compound nuclear structure. It has been observed that the heavy ion colli-

sion reactions lead to symmetric mass fragmentation for such compact nuclear structure, formed in above barrier interaction along the equatorial axis of collision. Hence fusion-fission component is characterized by symmetric fragment distribution. On the contrary, quasi-fission has been recognized by broad fragment mass distribution from the elongated nuclear structure, formed at relatively lower incident energies. In other words, quasi-fission mainly leads to the formation of asymmetric fragments. Polar collision at below or sub-barrier energies is considered as the possible reason for the occurrence of quasi-fission process. Hence one may observe, different mass and/or TKE distributions [50] for fusion-fission and quasi-fission channels.

In order to address the orientation based processes, even-Z superheavy nuclear systems $^{268}Sg^{*}$ [27] and $^{278,286}112^{*}$ [31] are investigated through DCM [22]- [32] approach where fusion-fission component (corresponding to symmetric/near symmetric mass distribution) is recognized for compact equatorial configuration at above barrier energies. However, for elongated configuration used at lower incident energies, the asymmetric fragment distribution is dominant, exhibiting quasi-fission like mechanism.

1.3.3 Alpha (α)- decay

Till now we have been concentrating on the excited state compound and non-compound nucleus dynamics which occur before the formation of a relatively stable superheavy nucleus. Following the neutron evaporation, the residual superheavy nuclei are formed with relatively stable configurations, but due to small lifespan they usually decay via alpha emission and/or spontaneous fission. Theoretically, these processes share the same underlying mechanism in physics known as quantum mechanical tunnelling effect, first explained by Gamow [51] in 1928. Later Condon and Gurney independently explained this phenomenon by means of the wave mechanics [52]. In this pioneering work, the α-decay was

contemplated as the penetration of the pre-born fragment inside the heavy/superheavy nuclei which carries away the positive charge to achieve the largest possible release of the kinetic energy. It becomes increasingly important for heavy nuclei because the disruptive Coulomb force increases with the size at faster rate (namely, as Z^2) than does the specific nuclear binding force which increases approximately as A. Hence a large number of nuclei lying in the periodic table exhibit the α-decay phenomenon [53, 54] which was first seen a century ago in the famous Rutherford experiment [55].

According to the microscopic analysis, α-decay is possible only if the shell effects supply an extra binding energy to increase the fission barrier height. Usually, in the course of a series of α decays, the effect of magic shells for superheavy nuclei gradually becomes weaker for descendant isotopes and finally terminates the chain by spontaneous fission, characterized by the minimum shell effects. In spite of this, the decaying scenario is different for even-Z and odd-Z nuclei. In the odd-Z isotopes, the probability of α-decay with respect to spontaneous fission increases because of the strong fission hindrance caused by unpaired nucleons [45,48]. Consequently, long lived decay chains are observed for odd-Z nuclei.

To further analyze this concept, the Preformed cluster model (PCM) [56]- [59] based on the Quantum Mechanical Fragmentation Theory (QMFT) is applied for investigating the α-decay of Z=115 isotopes [28]. A nice fitting of the experimentally observed half-lives is obtained within a constant scaling factor in penetration probability (P) for the α-decay chains of $^{287}115$, $^{288}115$ and $^{289}115$ nuclei formed in $4n$, $3n$ and $2n$ channels of $^{291}115^{*}$ respectively. The detailed description of α- emission from Z=115 isotopes is discussed later in chapter 4.

1.3.4 Heavy particle radioactivity (HPR)

The exotic radioactive decay between α-emission and spontaneous fission is known as cluster radioactivity or heavy particle decay apart from the three basic decay modes (α- decay, β-decay and γ-emission). The first signature of the cluster radioactivity was observed by Rose and Jones [60] in 1984 through the detection of ^{14}C cluster emitted from ^{223}Ra nucleus. Since then, a number of cluster radioactive decays from heavy parent nuclei with Z = 87 to 96 were investigated. The daughter nucleus is always ^{208}Pb (a doubly closed shell nucleus) or its neighboring nucleus for all the cluster decays in trans-lead region. This observation has been verified in almost all experimental and theoretical studies, and hence consequently one may presume that the shell structure of daughter nucleus significantly contributes towards the cluster radioactivity process. The concept of heavy particle radioactivity ($Z_{cluster} > 28$) with corresponding daughter nucleus around ^{208}Pb for superheavy elements (Z > 110) is recently studied by Poenaru *et al.* [61] using analytical super-asymmetric fission model (ASAFM). Various heavy clusters ranging Z=29-42 are reported in [61] with a possible interpretation of cluster half-lives (T_C) and branching ratios relative to alpha (α)- decay.

Through collective clusterization process, the cluster decay of ^{278}113, $^{287-289}$115 and ^{293,294}117 [59] nuclei is investigated using Preformed cluster model (PCM) [56]- [59] leading to doubly magic ^{208}Pb or its neighboring nuclei. The calculations have been done by including two different versions of proximity potential such as Prox-77 [62] and Prox-00 [63] (having different isospin and asymmetry dependent parameters). The detailed description of heavy particle radioactivity (HPR) is discussed in chapter 4.

Conclusively from the above discussion of this chapter, one may observe that paving the way towards the center of stability of extreme mass nuclei, the Dynamical cluster decay model (DCM) [22]- [32] which is the reformulation of the Preformed cluster model

(PCM) [56]- [59] revitalized this interesting journey by handling the various decay modes such as neutron evaporation channels, fusion-fission, quasi-fission, alpha decay and heavy particle radioactivity (HPR). The rigorous understanding of the dynamical features of hot and rotating nuclei such as angular momentum, excitation energy, deformations and orientations of the incoming and the decaying channels shaped this formalism in the magnificent way to grasp a complete knowledge of superheavy reaction dynamics.

1.4 Organization of thesis

The thesis is organized as follows:

Chapter 2 gives details of Preformed cluster model [56]- [59] (PCM) applied for ground state decays and Dynamical cluster decay model (DCM) [22]- [32] for understanding the decay of hot and rotating compound nuclei. These methodologies are based on the Quantum Mechanical Fragmentation Theory (QMFT) [33, 34], using collective mass transfer in binary fragmentation process. Besides the temperature and angular momentum effects in the decay of hot (excited) compound nuclei, DCM takes care of the deformation and orientation effects of the nuclei involved. The temperature dependent binding energies, proximity and Coulomb interactions, along with angular momentum dependent potential contributing towards the preformation and penetrability processes are briefly described for DCM framework. The deformations and orientations of the fragments are also included in PCM, but the temperature and angular momentum effects are silent. The shell effects corresponding to proposed superheavy magic numbers are also included in PCM and DCM based calculations for overall understanding of structural aspects of nuclear systems formed in superheavy region.

In **Chapter 3**, first a brief account of the superheavy magic shell closures with Z=114, 120, 126 and N=184 is presented by understanding the neutron evaporation decay of $^{296}116^{*}$ [30] and $^{266}Rf^{*}$ [29] compound nuclei. The calculations are carried out for sticking (I_S) and non-sticking (I_{NS}) moments of inertia respectively. Within both approaches, it has been observed that Z=126 and N=184 is the best suited magic pair for addressing the neutron evaporation residues of superheavy nuclei. Following this analysis, the DCM has been applied to study the decay of $2n$, $3n$ and $4n$ evaporation channels of $^{297}117^{*}$ [26] compound nucleus formed in $^{48}Ca+^{249}Bk$ [48] hot fusion reaction. Using spherical fragmentation approach, σ_{2n}, σ_{3n} and σ_{4n} could not be addressed, whereas with the inclusion of quadrupole (β_{2i})- deformations and "optimum" orientations θ_i^{opt}, the σ_{2n} and σ_{3n} cross-sections were fitted nicely to the experimental data. The $4n$ cross-sections were still underestimated by about 25% which indicated the possibility of some other competing evaporation residue, like the ^{4}He decay, contributing to $4n$-decay cross-sections. In addition to this, a possible contribution of fusion-fission component is also predicted which needs experimental verification.

In **Chapter 4**, the DCM calculated excitation functions of $2n$, $3n$ and $4n$ evaporation residues are obtained for the decay of $^{291}115^{*}$ [28] compound nucleus, lying in the excitation energy range E^{*}_{CN}=31-47 MeV. In the decay of $^{291}115^{*}$, only $2n$-cross-sections could be fitted with the spherical choice of fragmentation. However, to address higher neutron clusters, say $3n$ and $4n$, the deformation effects are shown to play significant role. The PES for the spherical case indicate symmetric fission, whereas the deformed choice gives asymmetric peaks in the heavy mass fragment (HMF) region. The effect of dynamic deformations on the decay path of $^{291}115^{*}$ compound nucleus is also explored. Furthermore, the xn channel cross-sections are estimated at Bass barrier by interpolating the neck-length parameters fixed in reference to the available data [45]. In addition to

this, the α-decay chains from three isotopes of Z=115 with parent mass 287, 288 and 289 are investigated by using the Preformed cluster model (PCM) with "hot" optimum orientations [28]. A nice fitting of the experimentally observed half-lives is obtained within a constant scaling factor in penetration probability for spherical and deformed fragmentation approach. Another application of the Preformed cluster model (PCM) is explored through the study of heavy particle radioactivity (HPR) from the ground state decay of $^{293,294}117$, $^{287-289}115$ and $^{278}113$ superheavy nuclei [59]. The calculations have been done for two different versions of proximity potential, i.e. Prox-77 [62] and Prox-00 [63].

In **Chapter 5**, the Dynamical cluster decay model (DCM) is used to study the orientation effects in the dynamics of $^{268}Sg^*$ compound nucleus [27] at above and below Coulomb barrier energies. For above barrier, the symmetric mass distribution is observed, using 'hot equatorial configuration' which is supplemented by the asymmetric mass fragmentation for 'cold polar configuration' at below/ sub barrier energies. The asymmetric peaks at sub-barrier energies may be associated with some competing process, like quasi-fission. The contribution of barrier modification at above-barrier energies is relatively lower for hot equatorial configuration as compared to cold polar configuration. The exclusive role of deformations is also explored by comparing spherical fragmentation with β_{2i}-static and β_{2i}-dynamic fragmentation approaches.

In **Chapter 6**, the effect of higher multipole shapes included upto hexadecapole (β_{4i})-deformations is studied to understand the dynamics of $^{40,48}Ca + ^{238}U \rightarrow ^{278,286}112^*$ reactions [31]. With inclusion of hexadecapole (β_{4i})-deformations the compact angle is modified, and the compact configuration is observed for $\theta_c < 90^0$ for both nuclear systems. Further, the decay path of $^{278}112^*$ and $^{286}112^*$ compound nuclei show changes in the potential energy surfaces (PES) when the spherical fragmentation approach is substituted by static β_{2i} and β_{4i} deformed fragmentations. The isotopic analysis of $^{278,286}112^*$ compound

nuclei shows higher contribution of quasi-fission for neutron deficient $^{278}112^{*}$ nucleus. In addition to the above, the role of changing N/Z ratio is also observed through the decay of $^{288,290,292,294}114^{*}$ compound nuclei. No significant changes in the fragmentation and preformation profile are observed by changing the N/Z ratio in Z=114 isotopes. Besides this, the role of isospin in Z=115 isotopes is observed by comparing the xn-channel cross-sections of $^{289,291,293}115^{*}$ nuclei formed in ^{48}Ca $+^{241,243,245}$Am reactions. The systematic variation in xn cross-sections as a function of target mass imparts useful information in reference to the isotopic dependence of the Z=115 element.

Finally **Chapter 7**, concludes the over all work of the thesis. Brief notes regarding the significance of the work and scope for extension of this work is discussed.

Bibliography

[1] H. Becquerel, Compt. Rend. **122**, 420 (1896).

[2] N. Bohr and J. A. Wheeler, Phys. Rev. **56**, 426 (1939).

[3] Yu. Ts. Oganessian and Yu. A. Lazarev, *Treatise on Heavy-Ion Science* edited by D. A. Bromley (New York: Plenum) vol **4**, p3 (1985).

[4] W. D. Myers and W. J. Swiatecki, Nucl. Phys. **81**, 1 (1966); W. D. Myers and W. J. Swiatecki, Ark Fys. **36**, 343 (1967).

[5] Yu. Ts. Oganessian, J. Phys. G: Nucl. Part. Phys. **34**, R165 (2007).

[6] G. T. Seaborg, Ann. Rev. Nuclear Sci. **18**, 53 (1968).

[7] O. Haxel, J. H. D. Jensen, and H. E. Suess, Phys. Rev. **75**, 1766 (1949).

[8] M. G. Mayer, Phys. Rev. **75**, 1969 (1949).

[9] http://www-win.gsi.de/tasca/research.html, Tasca research program.

[10] V. M. Strutinsky, Nucl. Phys. A **95**, 420 (1967); Nucl. Phys. A **122**, 1 (1968).

[11] U. Mosel and W. Greiner, Z. Phys. **222**, 261 (1969); A. Sobiczewski, Phys. Part. Nuclei **25**, 295 (1994).

[12] P. Moller and J. R. Nix, J. Phys. G: Nucl. Part. Phys. **20**, 1681 (1994); R. Smolanczuk, J. Skalski, and A. Sobiczewski, Phys. Rev. C **52**, 1871 (1995).

[13] S. Cwiok, J. Dobaczewski, P. H. Heenen, P. Magierski, and W. Nazarewicz, Nucl. Phys. A **611**, 211 (1996).

[14] K. Rutz, M. Bender, T. Burvenich, T. Schilling, P. G. Reinhard, J. A. Maruhn, and W. Greiner, Phys. Rev. C **56**, 238 (1997).

[15] J. F. Berger, M. Girod, and D. Gogny, Nucl. Phys. A **428**, 23c (1984); J. F. Berger, L. Bitaud, J. Decharge, M. Girod, and S. Peru-Desenfants, Proc. of Int. Hirschegg Workshop XXIV, *Extremes of Nuclear Structure* edited by H. Feldmeier, J. Knoll, and W. Norenberg, (GSI, Darmstadt), p. 56 (1996).

[16] H. F. Boersma, Phys. Rev. C **48**, 472 (1993); G. A. Lalazissis, M. M. Sharma, P. Ring, and Y. K. Gambhir, Nucl. Phys. A **608**, 202 (1996).

[17] P. Armbruster, Annu. Rev. Nucl. Part. Sci. **50**, 411 (2000).

[18] M. Bender, K. Rutz, P. G. Reinhard, J. A. Maruhn, and W. Greiner, Phys. Rev. C **60**, 034304 (1999); A. T. Kruppa, M. Bender, W. Nazarewicz, P. G. Reinhard, T. Vertse, and S. Cwiok, Phys. Rev. C **61**, 034313 (2000).

[19] P. K. Rath, R. Chandra, K. Chaturvedi, P. K. Raina, and J. G. Hirsch, Phys. Rev. C **80**, 044303 (2009).

[20] A. Bharti and S. K. Khosa, Phys. Rev. C **53**, 2528 (1996).

[21] R. K. Gupta, S. K. Patra, and W. Greiner, Mod. Phys. Lett. A **12**, 1727 (1997); S. K. Patra, C. L. Wu, C. R. Praharaj, and R. K. Gupta, Nucl. Phys. A **651**, 117 (1999).

[22] R. K. Gupta, M. Balasubramaniam, R. Kumar, N. Singh, M. Manhas, and W. Greiner, J. Phys. G: Nucl. Part. Phys. **31**, 631 (2005).

[23] R. K. Gupta, M. Manhas, and W. Greiner, Phys. Rev. C **73**, 054307 (2006).

[24] M. K. Sharma, G. Sawhney, R. K. Gupta, and W. Greiner, J. Phys. G: Nucl. Part. Phys. **38**, 105101 (2011); M. K. Sharma, S. Kanwar, G. Sawhney, R. K. Gupta, and W. Greiner, J. Phys. G: Nucl. Part. Phys. **38**, 055104 (2011).

[25] D. Jain, R. Kumar, M. K. Sharma, and R. K. Gupta, Phys. Rev. C **85**, 024615 (2012); M. Kaur, R. Kumar, and M. K. Sharma, Phys. Rev. C **85**, 014609 (2012); G. Sahwney, G. Kaur, M. K. Sharma, and R. K. Gupta, Phys. Rev. C **88**, 034603 (2013).

[26] K. Sandhu, M. K. Sharma, and R. K. Gupta, Phys. Rev. C **85**, 024604 (2012).

[27] K. Sandhu, M. K. Sharma, and R. K. Gupta, Phys. Rev. C **86**, 064611 (2012).

[28] R. Kumar, K. Sandhu, M. K. Sharma, and R. K. Gupta, Phys. Rev. C **87**, 054610 (2013).

[29] K. Sandhu, M. K. Sharma, A. Kaur, and R. K. Gupta, Phys. Rev. C **90**, 034610 (2014).

[30] K. Sandhu and M. K. Sharma, AIP Conf. Proc. **1524**, 123 (2013).

[31] K. Sandhu, G. Kaur, and M. K. Sharma, Nucl. Phys. A **921**, 114 (2014).

[32] K. Sandhu and M. K. Sharma, Braz. J. Phys. **44**, 64 (2014).

[33] J. Maruhn and W. Greiner, Phys. Rev. Lett. **32**, 548 (1974).

[34] R. K. Gupta, W. Scheid, and W. Greiner, Phys. Rev. Lett. **35**, 353 (1975).

[35] R. K. Gupta, Niyti, M. Manhas, and W. Greiner, J. Phys. G: Nucl. Part. Phys. **36**, 115105 (2009); Niyti, R. K. Gupta, and W. Greiner, J. Phys. G: Nucl. Part. Phys. **37**, 115103 (2010).

[36] G. T. Seaborg and W. D. Loveland, *The Elements Beyond Uranium*, (New York: Wiley) (1990).

[37] S. Hofmann, Rep. Prog. Phys. **61**, 639 (1998).

[38] P. Armbruster, Annu. Rev. Nucl. Part. Sci. **35**, 135 (1985).

[39] G. Munzenberg, Rep. Prog. Phys. **51**, 57 (1988).

[40] E. K. Hulet *et al.*, Phys. Rev. Lett. **39**, 385 (1977).

[41] Yu. Ts. Oganessian, M. G. Itkis, A. G. Popeko, V. K. Utyonkov, and A. V. Yeremin, Nucl. Phys. A **682**, 108c (2001).

[42] Yu. Ts. Oganessian *et al.*, Phys. Rev. C **70**, 064609 (2004).

[43] P. A. Ellison *et al.*, Phys. Rev. Lett. **105**, 182701 (2010).

[44] J. M. Gates *et al.*, Phys. Rev. C **83**, 054618 (2011).

[45] Yu. Ts. Oganessian *et al.*, Phys. Rev. Lett. **108**, 022502 (2012), Phys. Rev. C **87**, 014302 (2013).

[46] S. Hofmann *et al.*, Eur. Phys. J. A **48**, 62 (2012).

[47] Yu. Ts. Oganessian *et al.*, Phys. Rev. C **74**, 044602 (2006); G. Mandaglio, G. Giardina, A. K. Nasirov, and A. Sobiczewski, Phys. Rev. C **86**, 064607 (2012).

[48] Yu. Ts. Oganessian *et al.*, Phys. Rev. C **83**, 054315 (2011).

[49] W. Greiner, International NATO Advanced Study Institute (NASI) Course on *Quantum Electrodynamics of Strong Fields*, Lahnstein (1981); M. Seiwert, N. Abul-Naga, V. Oberacker, J. A. Maruhn, and W. Greiner, Gesellschaft fur Schwerionenforschung (GSI) Annual Report (1981).

[50] K. Nishio, H. Ikezoe, I. Nishinaka, S. Mitsuoka, K. Hirose, T. Ohtsuki, Y. Watanabe, Y. Aritomo, and S. Hofmann, Phys. Rev. C **82**, 044604 (2010); K. Nishio, S. Mitsuoka, I. Nishinaka, H. Makii, Y. Wakabayashi, H. Ikezoe, K. Hirose, T. Ohtsuki, Y. Aritomo, and S. Hofmann, Phys. Rev. C **86**, 034608 (2012).

[51] G. Gamov, Z. Phys. **51**, 204 (1928).

[52] R. W. Gurney and E. U. Condon, Nature (London) **122**, 439 (1928).

[53] R. K. Gupta, S. Kumar, R. Kumar, M. Balasubramaniam, and W. Schied, J. Phys. G: Nucl. Part. Phys. **28**, 2875 (2002); Y. K. Gambhir, A. Bhagwat, M. Gupta, and A. K. Jain, Phys. Rev. C **68**, 044316 (2003).

[54] S. Kumar, M. Balasubramaniam, R. K. Gupta, G. Munzenberg, and W. Schied, J. Phys. G: Nucl. Part. Phys. **29**, 625 (2003); K. P. Santhosh, J. G. Joseph, and S. Sahadevan, Phys. Rev. C **82**, 064605 (2010).

[55] E. Rutherford and H. Geiger, Proc. R. Soc. London, Ser. A. **81**, 162 (1908); E. Rutherford and T. Royds, Phil. Mag. **17**, 281 (1909).

[56] S. S. Malik and R. K. Gupta, Phys. Rev. C **39**, 1992 (1989).

[57] G. Sawhney, M. K. Sharma, and R. K. Gupta, Phys. Rev. C **83**, 064610 (2011).

[58] R. Kumar and M. K. Sharma, Phys. Rev. C **85**, 054612 (2012).

[59] G. Sawhney, K. Sandhu, M. K. Sharma, and R. K. Gupta, Eur. Phys. J. A **50**, 175 (2014).

[60] H. J. Rose and G. A. Jones, Nature (London) **307**, 245 (1984).

[61] D. N. Poenaru, R. A. Gherghescu, and W. Greiner, Phys. Rev. Lett. **107**, 062503 (2011); Phys. Rev. C **85**, 034615 (2012).

[62] J. Blocki, J. Randrup, W. J. Swiatecki, and C. F. Tsang, Ann. Phys. (NY) **105**, 427 (1977).

[63] W. D. Myers and W. J. Swiatecki, Phys. Rev. C **62**, 044610 (2000).

Chapter 2

Methodology

2.1 Introduction

The various theoretical attempts to locate an 'island of stability' have widened the area of nuclear research to a substantial extend. With such efforts, great opportunities are being provided to understand the superheavy structure and associated reaction dynamics. For example, the theoretical approaches such as Strutinsky macro-microscopic method [1], the (non-relativistic) self consistent Skyrme (or Gogny) Hartree-Fock [2, 3] and the relativistic mean field theories [4, 5] have been successfully applied in this field to explore the properties and related aspects of superheavy nuclei. In the present work, we have applied the Preformed cluster model (PCM) [6]- [10] and Dynamical cluster decay model (DCM) [11]- [24], which are based on the well known Quantum Mechanical Fragmentation Theory (QMFT) [25]- [30].

The QMFT (based on two center shell model) is a unified description of two body channel heavy ion interaction and is the only theory, given prior to experiments, that brings out clearly the applicability of the quantum concept of probability and role of shell effects for fusion reactions as well as for fission processes. It is used as an average two

body potential in Strutinsky macro-microscopic method [1]. In QMFT [25]- [30], the substantive quantities for the description of the nuclear dynamics are the potential energy surfaces and the mass parameters defining the kinetic energy of the system. The QMFT works in terms of the following collective variables:

(i) relative separation distance (co-ordinate) R between the two nuclei or (or, equivalently the length parameter $\lambda = L/2R_0$, with L as the length of the nucleus and R_0 is the radius of the spherical nucleus).

(ii) The deformation co-ordinates $\beta_{\lambda i}$ (λ=2,3,4... and i=1,2) of the decaying and colliding nuclei.

(iii) The orientation degree of freedom $\theta_i (i = 1, 2)$ of the deformed interacting nuclei.

(iv) Azimuthal angle ϕ between the principal planes of the two interacting nuclei.

(v) Neck parameter ε, defined by the ratio $\varepsilon = E_0/E'$ for the interaction region ($R < R_1 + R_2$, R_i (i=1, 2) is the radius of the two nuclei). Here E_0 is the actual height of the barrier and E' is the fixed barrier of the two center oscillator. $\epsilon = 0$ represents a broad neck formation, whereas $\epsilon = 1$ gives that the neck is fully squeezed in, corresponding to the asymptotic region ($R > R_1 + R_2$).

(vi) Mass and charge fragmentation co-ordinates [25–27]. The mass and charge fragmentation for separated nuclei/fragments for the two body channels are defined by the mass and charge-asymmetry coordinates as:

$$\eta = \frac{A_1 - A_2}{A}; \qquad \eta_Z = \frac{Z_1 - Z_2}{Z} \tag{2.1}$$

Similarly, the neutron asymmetry coordinate [27]

$$\eta_N = \frac{N_1 - N_2}{N} \tag{2.2}$$

can also be used, but it is sufficient to treat only two of them as dynamical co-ordinates since they are related as:

$$\eta = \frac{Z}{A}\eta_Z + \frac{N}{A}\eta_N \tag{2.3}$$

Here $Z = Z_1 + Z_2$, $N = N_1 + N_2$ and $A = A_1 + A_2$. Z_i, N_i and A_i $(i = 1, 2)$ are the charge number, the neutron number and the mass number of two decaying fragments. Z, N and A are respectively the charge number, neutron number and mass number of the compound nuclear system. The η_Z coordinate gives the associated charge distribution effects.

In terms of these collective coordinates and their velocities, the collective Hamiltonian can be written as:

$$H = K(\mathbf{R}, \beta, \varepsilon, \eta, \eta_Z; \dot{\mathbf{R}}, \dot{\beta}, \dot{\varepsilon}, \dot{\eta}, \dot{\eta}_Z) + V(\mathbf{R}, \beta, \varepsilon, \eta, \eta_Z) \tag{2.4}$$

Here K refers to the kinetic energy and V to collective potential energy. The $\mathbf{R}$, ε, η, η_Z are already defined above and β stands for $\beta_{\lambda 1}$ and $\beta_{\lambda 2}$; λ=2,3,4... .
For the potential $V(\eta, \eta_Z, R)$, minimized in the η_Z co-ordinate, Schrödinger wave equation in terms of mass co-ordinates η and relative separation R co-ordinates can be written as:

$$H(\eta, R)\psi(\eta, R) = E(\eta, R)\psi(\eta, R) \tag{2.5}$$

with the Hamiltonian,

$$H(\eta, R) = K(\eta) + K(R) + K(\eta, R) + V(\eta) + V(R) + V(\eta, R) \tag{2.6}$$

The mass parameters B_{ij}, defining the kinetic energy term K in the above Eqs. (2.4) and (2.6) are either the cranking masses used in the Asymmetric Two-Center Shell Model

($ATCSM$) or the classical hydrodynamical masses [31], which are shown to have good agreement with microscopic cranking calculations. The coupling term of the kinetic energy $K(\eta, R)$, proportional to $\frac{\partial^2}{\partial\eta\partial R}$, is neglected here, since the coupled cranking masses are very small [25, 27], ($B_{R\eta} \ll (B_{RR}B_{\eta\eta})^{1/2}$ and $B_{R\eta z} \ll (B_{RR}B_{\eta z\eta z})^{1/2}$). Same is true for the coupling term of potential energy $V(\eta, R)$.

Therefore, in a decoupled approximation [30], the Schrödinger equation (2.5) can be solved for which the Hamiltonian takes the form:

$$H = -\frac{\hbar^2}{2\sqrt{B_{\eta\eta}}}\frac{\partial}{\partial\eta}\frac{1}{\sqrt{B_{\eta\eta}}}\frac{\partial}{\partial\eta} - \frac{\hbar^2}{2\sqrt{B_{RR}}}\frac{\partial}{\partial R}\frac{1}{\sqrt{B_{RR}}}\frac{\partial}{\partial R} + V(\eta) + V(R) \tag{2.7}$$

For decoupled Hamiltonian (2.7), Schrödinger wave Eq. (2.5) can be separated for the η and R co-ordinates as follows,

$$\left[-\frac{\hbar^2}{2\sqrt{B_{\eta\eta}}}\frac{\partial}{\partial\eta}\frac{1}{\sqrt{B_{\eta\eta}}}\frac{\partial}{\partial\eta} + V(\eta)\right]\psi^{\nu}(\eta) = E^{\nu}_{\eta}\psi^{\nu}(\eta) \tag{2.8}$$

and

$$\left[-\frac{\hbar^2}{2\sqrt{B_{RR}}}\frac{\partial}{\partial R}\frac{1}{\sqrt{B_{RR}}}\frac{\partial}{\partial R} + V(R)\right]\psi^{\nu}(R) = E^{\nu}_{R}\psi^{\nu}(R) \tag{2.9}$$

with

$$\psi(\eta, R) = \psi(\eta)\psi(R) \tag{2.10}$$

and

$$E = E_{\eta} + E_{R} \tag{2.11}$$

The states $\psi^{\nu}(\eta)$ are the vibrational states in the potential $V(\eta)$ and are labelled by the quantum numbers $\nu = 0, 1, 2, ...$

The Schrödinger equation Eq. (2.8) is formulated here to calculate the preformation

probability (P_0) of the fragments, as this theory is based on the fact that the fragments are pre-born prior to the decay of the nuclear system. Once the clusters/fragments are preformed, their penetration probability P across the interaction barrier can be calculated by using the WKB approximation. On the basis of this concept, the Preformed cluster model (PCM) was proposed in [6]- [10], which was formulated to understand the ground state cluster decay of radioactive nuclei along with α-emission and spontaneous fission. Following the successful application of PCM for ground state decays, further attempt was made and the Dynamical cluster decay model (DCM) [11]- [24] was worked out which have been used extensively to study the decay of hot and rotating excited compound nuclear systems. The Preformed cluster model (PCM) [6]- [10] is T=0 and ℓ=0 version of Dynamical cluster decay model (DCM) [11]- [24], the deformation and orientation effects are duly incorporated in both the formalisms. In Fig. 2.1 below, the flowchart is provided to understand the basic structure of Preformed cluster model (PCM) and Dynamical cluster decay model (DCM). Fig. 2.1, suggests the procedure for calculating channel cross-sections and decay half-lives respectively in DCM and PCM approaches.

Following the description of flowchart, the chapter is organized in a way, that first, the input potentials required for obtaining the preformation probability (P_0) and the penetration probability (P) are discussed. Then, the complete analysis of P_0 and P is presented with and without temperature and angular momentum effects for DCM and PCM respectively. Finally, the description of the channel cross-sections and decay half-lives is explained in brief.

2.2 The Fragmentation potential $V(\eta)$

The fragmentation potential or collective potential energy required to solve the Eq. (2.8) is calculated differently for the Preformed cluster model (PCM) and Dynamical cluster

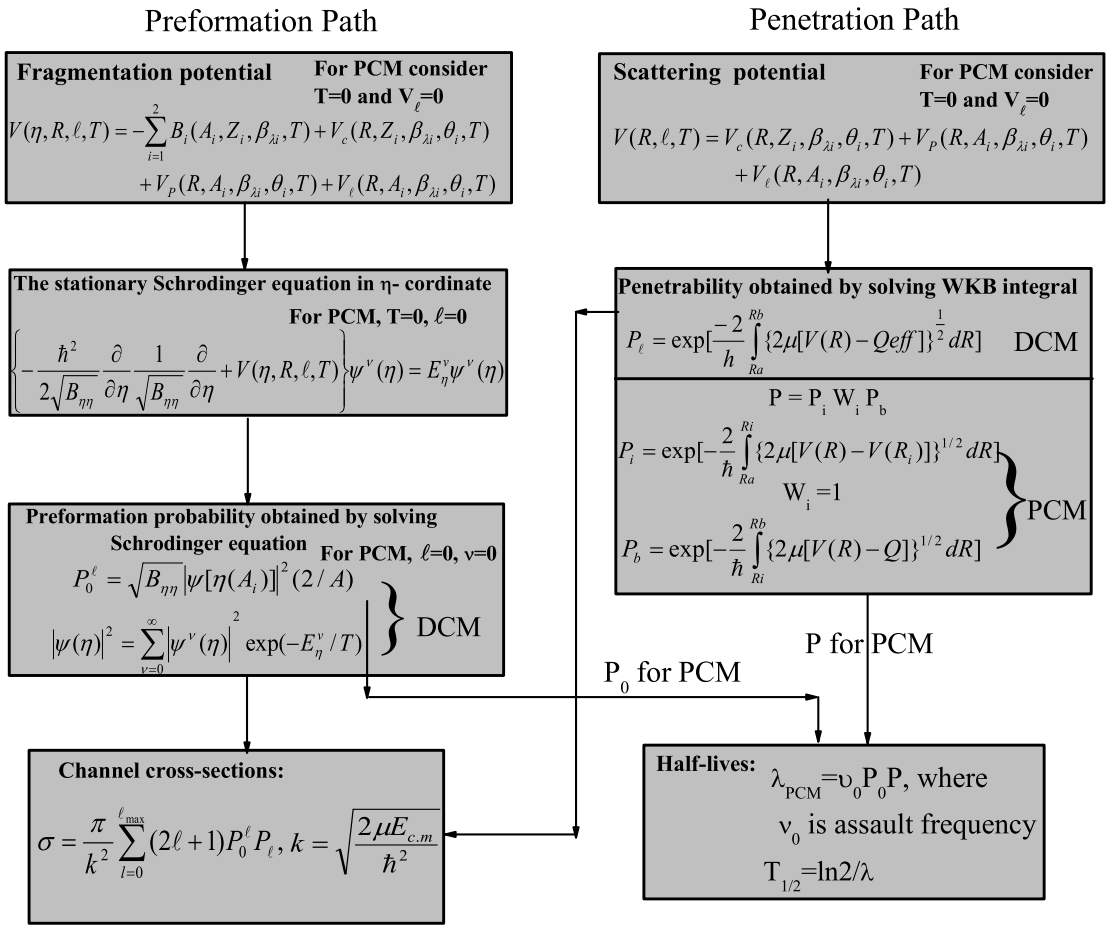

Figure 2.1 Flowchart representing the basic structure of Preformed cluster model (PCM) [6]- [10] and Dynamical cluster decay model (DCM) [11]- [24].

decay model (DCM). For PCM, the required expression of fragmentation potential for deformed and oriented nuclei is:

$$V(\eta,R)=-\sum_{i=1}^{2}B_i(A_i,Z_i,\beta_{\lambda i})+V_c(R,Z_i,\beta_{\lambda i},\theta_i)+V_p(R,A_i,\beta_{\lambda i},\theta_i) \tag{2.12}$$

where $B_i(A_i,Z_i)$ are the binding energies of the incoming as well as the decaying fragments. V_C is the Coulomb potential required to address the charged particles interactions, and V_P is the nuclear proximity potential which is observed when the surfaces of interact-

ing nuclei are brought in close proximity. From Eq. (2.12), it is clear that the fragmentation potential used in the PCM is temperature and angular momentum independent. On the other hand, for DCM approach, the collective potential energy $V(\eta)$ is modified by introducing an additional centrifugal term to include the angular momentum effects. In addition to this, the temperature effects are also included in each potential to address the dynamics of hot and rotating nuclei. The temperature and angular momentum dependent fragmentation potential is given as:

$$\begin{aligned} V(\eta, R, \ell, T) &= -\sum_{i=1}^{2} B_i(A_i, Z_i, \beta_{\lambda i}, T) + V_c(R, Z_i, \beta_{\lambda i}, \theta_i, T) \\ &+ V_p(R, A_i, \beta_{\lambda i}, \theta_i, T) + V_\ell(R, A_i, \beta_{\lambda i}, \theta_i, T) \end{aligned} \tag{2.13}$$

Here the charges Z_i are fixed by minimizing the potential V(η), in the η_Z coordinate at each η-value.

The fragmentation potential $V(\eta)$ for both formalisms is calculated at a fixed distance $R = R_1 + R_2 + \Delta R$ for consideration of deformed and oriented fragments, with

$$R_i(\alpha_i, T) = R_{0i}(T)[1 + \sum_{\lambda} \beta_{\lambda i} Y_\lambda^{(0)}(\alpha_i)], \tag{2.14}$$

and

$$R_{0i}(T) = [1.28A_i^{1/3} - 0.76 + 0.8A_i^{-1/3}] \times (1 + 0.0007T^2) \tag{2.15}$$

Here λ=2,3,4..., and α_i is the angle between the radius vector R_i and symmetry axis of the colliding nuclei (see Fig. 2.2), measured clockwise. In addition to this, the θ_i is the angle of orientation, defined as an angle between the symmetry axis and the axis of collision, with it's rotation measured in anti-clockwise direction from the axis of collision. Fig. 2.2 shows a schematic configuration of two axially symmetric deformed, oriented nuclei, lying

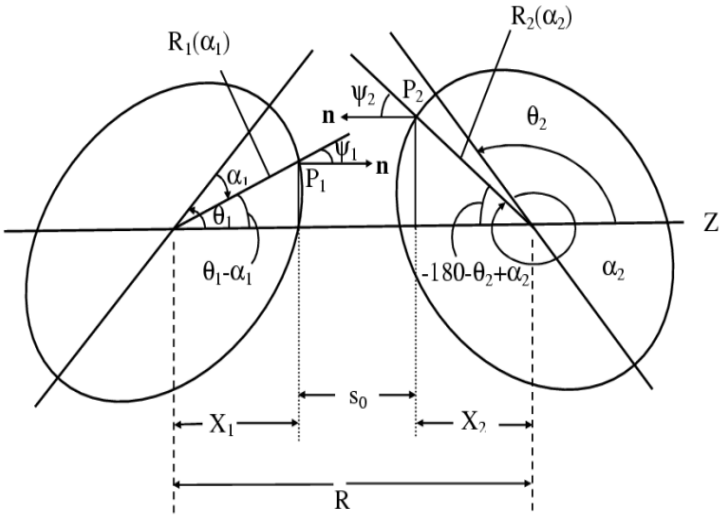

Figure 2.2 Schematic configurations of two axially symmetric deformed, oriented nuclei, lying in the same plane and for various θ_1 and θ_2 values in the range 0^0 to 180^0 [32]. The θ's are measured anticlockwise direction from the colliding axis and the angle α's in clockwise from the symmetry axis.

in the same plane ($\phi = 0^0$), for various θ_1 and θ_2 values in the range 0^0 to 180^0.

It is relevant to mention here that the temperature dependence shown in equations Eq. (2.14) and Eq. (2.15) are applicable only for DCM framework, while using PCM the radius vector R_i should be calculated at T=0.

2.2.1 Binding energies B_i's

B_i (i=1,2) appearing in Eq. (2.12) and (2.13), are the binding energies of nuclei, available from the experimental data of Audi-Wapstra [33]. Wherever the experimental B's are not available, the theoretical binding energies of Möller *et al.* [34] are used. In PCM, the temperature independent ground state binding energies are used, whereas the temperature dependence in the binding energies is included to understand the excited state decays through DCM.

Note that within the Strutinsky renormalization procedure [1], the binding energies contain both the macroscopic (liquid drop part) and the microscopic (shell correction) part, hence the binding energy B of a nucleus at temperature T is taken as the sum of liquid drop energy $V_{LDM}(T)$ and shell correction energy $\delta U(T)$ i.e

$$B(T) = V_{LDM}(T) + \delta U exp\left(- \frac{T^2}{{T_0}^2} \right) \tag{2.16}$$

The T dependent liquid drop contribution $V_{LDM}(T)$ is taken from Davidson *et al.* [35], which is based on the semi-empirical mass formula of Seeger [36], as:

$$\begin{aligned} V_{LDM}(A,Z,T) &= \alpha(T)A + \beta(T)A^{\frac{2}{3}} + \left(\gamma(T) - \frac{\eta(T)}{A^{\frac{1}{3}}}\right)\left(\frac{I^2 + 2 \mid I \mid}{A}\right) \\ &\quad + \frac{Z^2}{R_0(T)A^{\frac{1}{3}}}\left(1 - \frac{0.7636}{Z^{\frac{2}{3}}} - \frac{2.29}{[R_0(T)A^{\frac{1}{3}}]^2}\right) + \delta(T)\frac{f(Z,A)}{A^{\frac{3}{4}}}, \end{aligned} \tag{2.17}$$

where

$$I = a_a(Z - N), \quad a_a = 1.0,$$

and, respectively, for even-even, even-odd, and odd-odd nuclei,

$$f(Z,A) = (-1, 0, 1)$$

For $T = 0$, Seeger [36] obtained the constants, by fitting all even-even nuclei and 488 odd-A nuclei available at that time, as:

$$\alpha(0) = -16.11\text{MeV}, \quad \beta(0) = 20.21\text{MeV},$$

$$\gamma(0) = 20.65\text{MeV}, \quad \eta(0) = 48.00\text{MeV},$$

with the pairing energy term taken from Ref. [37],

$$\delta(0) = 33.0\text{MeV}.$$

For large amount of data available on ground-state binding energies, first the bulk constant $\alpha(0)$ and proton-neutron asymmetry constant a_a of $V_{LDM}(T = 0)$ were re-fitted in [11, 12, 15] to get the experimental binding energies. This was first done in [11, 12] for the 1995 Audi Wapstra Tables [38] of binding energies, and then in [15] for the 2003 Tables [33].

The T-dependent constants in Eq. (2.17) were obtained numerically as suggested by Davidson *et al.* [35] for the experimental information on the excited states of nuclei with T$\leq$5.5 MeV and extrapolated linearly for higher temperatures. These were calculated by determining the partition function $\mathcal{Z}$ (A, Z, T) of each nucleus in the canonical ensemble and making a least squares fit of the excitation energy

$$E_{ex}(A, Z, T) = V_{LDM}(A, Z, T) - V_{LDM}(A, Z, 0) \tag{2.18}$$

to the ensemble average

$$E_{ex}(A, Z, T) = T^2 \frac{\partial}{\partial T} ln\mathcal{Z}(A, Z, T) \tag{2.19}$$

The shell corrections in Eq. (2.16) are calculated from Myers and Swiatecki [39] "empirical" formula, contributing to the total binding energies, which are defined as:

$$\delta U = C \left[\frac{F(N) + F(Z)}{(A/2)^{\frac{2}{3}}} - cA^{\frac{1}{3}} \right] \tag{2.20}$$

where

$$F(X) = \frac{3}{5}\left(\frac{M_i^{\frac{5}{3}} - M_{i-1}^{\frac{5}{3}}}{M_i - M_{i-1}}\right)(X - M_{i-1}) - \frac{3}{5}\left(X^{\frac{5}{3}} - M_{i-1}^{\frac{5}{3}}\right) \tag{2.21}$$

with $X = N$ or Z, $M_{i-1} < X < M_i$ and M_i as the magic numbers 2, 8, 20, 28, 50, 82 and 126 or 120 or 114 for protons and 2, 8, 20, 28, 50, 82, 126 and 184 for neutrons. The constants $C = 5.8\ MeV$ and $c = 0.26$. The temperature dependent shell corrections in Eq. (2.16) are considered to vanish exponentially for higher excitation energies, approximately at T_0=1.5 MeV. Therefore only the liquid drop part is present at higher energies where the shell corrections vanish completely.

For superheavy elements, first the constants of $V_{LDM}(T = 0)$ are fitted for Z=126 and N=184 [11, 12, 15] magic pair. Next using Z=120 or 114 proton magic, the fitting of $V_{LDM}(T = 0)$ constants to address the experimental binding energy is again carried out in [21, 22, 40, 41]. $V_{LDM}(T = 0)$ is calculated as $V_{LDM}(T = 0)$=B(T=0)-δU(T = 0). As the δU(T = 0) changes for other magic pairs say Z=114, 120 and N=184, the liquid drop part is accordingly modified. Due to change in $V_{LDM}(T = 0)$ and hence in $V_{LDM}(T)$ for each pair of magic shells, the total fragmentation potential gets modified which in turn do influence the output parameters of PCM or DCM.

2.2.2 The Coulomb potential

It is the potential required to define the interaction between the two charged particles. Particularly in nuclear physics, it arises due the force of repulsion between the charged nuclei. It acts along the line joining the two nuclei. The Coulomb potential for two interacting spherical nuclei is given as:

$$V_c = \frac{Z_1 Z_2 e^2}{R} \tag{2.22}$$

For deformed and oriented interacting nuclei, different authors [42, 43] have given different expressions. The Coulomb potential for deformed and oriented nuclei in [42] is given as :

$$V_c(R, Z_i, \beta_{\lambda i}, \theta_i, T) = \frac{Z_1 Z_2 e^2}{R(T)} + 3Z_1 Z_2 e^2 \sum_{\lambda, i=1,2} \frac{R_i^{\lambda}(\alpha_i, T)}{(2\lambda+1)R(T)^{\lambda+1}} Y_{\lambda}^{(0)}(\theta_i) \left[\beta_{\lambda i} + \frac{4}{7}\beta_{\lambda i}^2 Y_{\lambda}^{(0)}(\theta_i)\right] \quad (2.23)$$

with R_i taken from Eq. (2.14). $Y_{\lambda}^{(0)}(\theta_i)$ represents the spherical harmonic function.

2.2.3 The Proximity Potential for deformed, oriented nuclei

This potential arises when the two surfaces are brought in close proximity with respect to each other. Broadly speaking, when two nuclear surfaces during interaction face each other within a small distance ($\approx 2fm$), then the surface energy term alone cannot give rise to the strong attraction. The attractive forces which then come into play are called proximity forces, and the additional potential due to these forces is called the proximity potential.

Having different isospin and asymmetry dependent parameters, various versions of the proximity potentials such as Prox-77, Prox-88, Prox-00, Bass-73, Bass-77, Bass-80, CW-76, BW-91, AW-95, Ngô-80 and Denisov DP were proposed. In the present work we have applied two different versions of the proximity potential namely, Prox-77 [44] and Prox-00 [45] to understand the superheavy reaction dynamics. Prox-77 is applied for majority of the nuclear systems, whereas the possible role of Prox-00 is explicitly discussed in chapter 4. The description of Prox-77 and Prox-00 potentials are defined below:

Proximity Potential-77

To account Prox-77, Blocki *et al.* [44] have reanalyzed and extended a theorem which was originally given by Deryagin [46], the theorem says that: the force between two gently curved surfaces in close proximity is proportional to the interaction potential per unit area between the two flat surfaces. The original version of Prox-77, based on the pocket formula of Blocki, was for spherical nuclei, and then extended for deformed and oriented nuclei by [32], and is given as:

$$V_p(R, A_i, \beta_{\lambda i}, \theta_i, T) = 4\pi \bar{R}(T)\gamma b(T)\Phi(s_0(T)) \tag{2.24}$$

where γ used is the specific nuclear surface tension, which is given by:

$$\gamma = 0.9517 \left[1 - 1.7826 \left(\frac{N-Z}{A}\right)^2\right] MeVfm^{-2} \tag{2.25}$$

and b is the diffuseness of the nuclear surface, which reads as:

$$b = \left[\pi/2\sqrt{3}\ln 9\right]_{t_{10-90}} \tag{2.26}$$

where t_{10-90} is the thickness of the surface in which the density profile changes from 90% to 10%. The value of b$\sim$1 fm. However, the temperature dependent b is given as:

$$b(T) = 0.99(1 + 0.009T^2) \tag{2.27}$$

The $\Phi(s_0)$ used in Eq. (2.24) is the universal function, independent of the shapes of nuclei or the geometry of nuclear system, but depends on the minimum separation distance s_0,

as:

$$\Phi(s_0) = \begin{cases} -\frac{1}{2}(s_0 - 2.54)^2 - 0.0852(s_0 - 2.54)^3 \\ -3.437exp(-\frac{s_0}{0.75}) \end{cases} \tag{2.28}$$

respectively, for $s_0 \leq 1.2511$ and $s_0 \geq 1.2511$. Here, s_0 is defined in units of b, i.e. s_0 is s_0/b. The s_0 is the distance of closest approach represented in Fig. 2.2, depends on deformations and orientations of reactants and products. For a fixed R, the minimum distance s_0 is defined as:

$$s_0 = R - X_1 - X_2 = R - R_1(\alpha_1)cos(\theta_1 - \alpha_1) - R_2(\alpha_2)cos(180 + \theta_2 - \alpha_2) \tag{2.29}$$

with the minimization conditions on s_0, we obtain

$$\begin{aligned} \tan(\theta_1 - \alpha_1) &= -\frac{R_1'(\alpha_1)}{R_1(\alpha_1)} \\ \tan(180 + \theta_2 - \alpha_2) &= -\frac{R_2'(\alpha_2)}{R_2(\alpha_2)} \end{aligned} \tag{2.30}$$

the $R_i'(\alpha_i)$ being first order derivative with respect to $R_i(\alpha_i)$.

For the axially symmetric shapes, the nuclear radius parameter (to all higher multipole orders λ=2,3,4,....) is given by Eqs. (2.14) and (2.15). In terms of the radii of curvature R_{i1} and R_{i2} in the principal planes of curvature of each nuclei (i=1,2) at the points of closest approach, the mean curvature radius $\bar{R}$ for deformed, oriented nuclei is given by:

$$\begin{aligned} \frac{1}{\bar{R}^2} &= \frac{1}{R_{11}R_{12}} + \frac{1}{R_{21}R_{22}} + \left[\frac{1}{R_{11}R_{21}} + \frac{1}{R_{12}R_{22}}\right] sin^2\phi \\ &+ \left[\frac{1}{R_{11}R_{22}} + \frac{1}{R_{21}R_{12}}\right] cos^2\phi \end{aligned} \tag{2.31}$$

Here, ϕ is the azimuthal angle between the principal planes of curvature of two nuclei (for co-planar nuclei ϕ=0^0).

Proximity Potential-00

Recently, Myers and Swiatecki [45] modified Eq.(2.24) by using the droplet model concept. The up-to-date knowledge of nuclear radii and surface tension coefficients are used within this formalism. Using the droplet model [47], matter radius C_i was calculated as:

$$C_i = c_i + \frac{N_i}{A_i} t_i (i = 1, 2) \tag{2.32}$$

where c_i denotes the half-density radii, obtained from the relation:

$$c_i = R_{00i} \left(1 - \frac{7}{2} \frac{b^2}{R_{00i}^2} - \frac{49}{8} \frac{b^4}{R_{00i}^4} + ... \right) \tag{2.33}$$

The authors of [45] had followed [48] to determine the half-density radii, either from the "two-parameter Fermi function" fits, or for a few cases of light nuclei, other parameterizations of the charge distributions were employed. For nuclei not listed in [48], the accurate formulae from [49] representing the measured rms values of the charge distributions were taken into consideration, expressed in terms of "equivalent rms radii". These are denoted by R_{00} in [49] and are approximated in [49] by

$$R_{00i} = 1.240 A_i^{1/3} \left\{ 1 + \frac{1.646}{A_i} - 0.191 \left(\frac{A_i - 2Z_i}{A_i} \right) \right\} fm \tag{2.34}$$

The t_i used in Eq. (2.32) is the neutron skin which is given as:

$$t_i = \frac{3}{2} r_0 \left(\frac{JI_i - \frac{1}{12} c_1 Z_i A_i^{-1/3}}{Q + \frac{9}{4} J A_i^{-1/3}} \right), \tag{2.35}$$

With r_0=1.14 fm. The value of nuclear symmetric energy coefficient J = 32.65 MeV, c_1=$3e^2/5r_0$=0.757895 MeV and neutron skin stiffness coefficient Q=35.4 MeV. The nu-

clear surface energy coefficient γ in terms of neutron skin reads as:

$$\gamma = \frac{1}{4\pi r_0^2}\left(18.63(MeV) - Q\frac{t_1^2 + t_2^2}{2r_0^2}\right) \tag{2.36}$$

with t_1 and t_2 taken from Eq. (2.35).

The universal function in the Prox-00 version is reported as:

$$\Phi(s_0) = \begin{cases} -0.1353 + \sum_{n=0}^{5}[c_n/(n+1)](2.5 - s_0)^{n+1} \\ \qquad \text{for} \quad 0 < s_0 \leq 2.5, \\ -0.09551\exp[(2.75 - s_0)/0.7176] \\ \qquad \text{for} \quad s_0 \geq 2.5, \end{cases} \tag{2.37}$$

The values of different constants c_n are c_0=-0.1886, c_1=-0.2628, c_2=-0.15216, c_3=-0.04562, c_4=0.069136, and c_5=-0.011454.

2.2.4 Rotational Energy due to angular momentum

The angular momentum effects of hot and rotating nuclei account an additional energy known as rotational energy, defined as:

$$V_\ell(R, A_i, \beta_{\lambda i}, \theta_i, T) = \frac{\hbar^2 \ell(\ell+1)}{2I(T)} \tag{2.38}$$

with moment of inertia in sticking limit, defined as:

$$I_s(T) = \mu R^2 + \frac{2}{5}A_1 m R_1^2(\alpha_1, T) + \frac{2}{5}A_2 m R_2^2(\alpha_2, T) \tag{2.39}$$

in which the individual masses/ charges are included in addition to the reduced mass ($\mu = \frac{A_1 A_2}{A_1 + A_2}m$). On the other hand, the reduced mass alone corresponds to the supposition

of prompt emission of fragments via use of moment of inertia in non-sticking limit, which is given by $I = I_{NS}{=}\mu R^2$ [50]. In DCM based calculations, the effect of non-sticking (I_{NS}) moment of inertia can mainly be observed for the decay of light particles (neutron evaporation) as the PES is modified only for evaporation channels and remains intact for IMFs, HMFs and fission fragments, as discussed in [22].

2.3 Scattering Potential $V(R)$

For a fixed η i.e. for given A_1 and A_2 combination, the scattering potential $V(R)$ is defined as the sum of Coulomb and proximity potentials where deformation and orientation effects are duly included i.e.

$$V(R) = V_c(R, Z_i, \beta_{\lambda i}, \theta_i) + V_p(R, A_i, \beta_{\lambda i}, \theta_i) \tag{2.40}$$

The above expression of the scattering potential is used to address the barrier penetration in PCM framework whereas angular momentum (corresponding to centrifugal potential) and temperature dependent scattering potential is applied in DCM approach, defined as:

$$V(R, \ell, T) = V_c(R, Z_i, \beta_{\lambda i}, \theta_i, T) + V_p(R, A_i, \beta_{\lambda i}, \theta_i, T) + V_\ell(R, A_i, \beta_{\lambda i}, \theta_i, T) \tag{2.41}$$

2.4 The Preformed Cluster Model

To understand the process of exotic cluster emission along with α-decay and spontaneous fission, many theoretical models were advanced [6], [51, 52] which may be broadly categorized as:

i) Unified fission model (UFM)

ii) Preformed cluster model (PCM)

The presumptions of both formalisms are completely different. In UFM [51, 52], which is the fission model, the cluster preformation is given by the penetrability of the internal part of the barrier. On the other hand, in PCM, the preformation probability is calculated by solving the Schrödinger wave Eq. (2.8) and is different for different clusters. It is relevant to mention here that in PCM the preformation probabilities P_0 for all the possible clusters can be obtained, whereas in other model like Blendowske *et al.* [53, 54], the preformation probabilities are calculated for the cluster mass up to $A = 28$ only. The Preformed cluster model [6]- [10] has been developed by adopting mainly the Gamow's theory [55] of α-decay. Here, instead of a square well potential, a more realistic nuclear potential, the nuclear proximity potential is used.

The decay constant, hence decay half-life in the PCM are defined as:

$$\lambda = \nu_0 P_0 P, \qquad T_{1/2} = \frac{\ln 2}{\lambda}, \tag{2.42}$$

The ν_0 in the above expression is the assault frequency. It is the frequency with which the cluster hits the barrier, and is defined as:

$$\nu_0 = \frac{v}{R_0} = \frac{(2E_2/\mu)^{1/2}}{R_0} \tag{2.43}$$

Here R_0 is taken as the radius of parent nucleus and $E_2 = \frac{1}{2}\mu v^2$ is the kinetic energy of the emitted cluster. In terms of the (positive) Q-value of decay, since both the emitted cluster and daughter nucleus are produced in ground state, the entire Q-value is the total kinetic energy ($Q = E_1 + E_2$), which is shared between the two fragments, such that for emitted cluster

$$E_2 = \frac{A_1}{A} Q \tag{2.44}$$

and $E_1(=Q-E_2)$ is the recoil energy of daughter nucleus.

2.4.1 Preformation probability P_0

The P_0 in Eq. (2.42) is the preformation probability, obtained as the solution of Schrödinger wave Eq. (2.8) in η-coordinate, for which the fragmentation potential as an input is calculated by Eq. (2.12). By solving numerically, Schrödinger wave equation gives solution as:

$$P_0(A_2) \propto |\psi^{\nu}(A_2)|^2 \tag{2.45}$$

with ν=0,1,2,3... referring to ground state (ν=0) and excited state solutions. For ground state decays such as α decay, spontaneous fission or cluster decay, only the lowest vibrational state $\nu = 0$ is taken. Then the mass (or charge) distribution yield which is proportional to the probability $|\psi^{(0)}(\eta)|^2$ (or $|\psi^{(0)}(\eta_Z)|^2$) is scaled to say, mass A_2 of one of the fragments ($d\eta = \frac{2}{A}$) and it is given by:

$$P_0 = |\psi_R^{(0)}(A_2)|^2 \frac{2}{A}\sqrt{B_{\eta\eta}(A_2)} \tag{2.46}$$

2.4.2 Penetration probability P

For R-motion, instead of solving the Schrödinger Eq. (2.9), we use the WKB approximation to calculate the penetration probability P. For each η-value, the potential V(R) for $R \geq R_t$ is calculated by using Eq. (2.40) whereas, for $R < R_t$ it is parameterized simply as a polynomial of degree two in R, given as:

$$V(R) = a_1 R + a_2 R^2 \qquad for \qquad R_0 \leq R \leq R_t \tag{2.47}$$

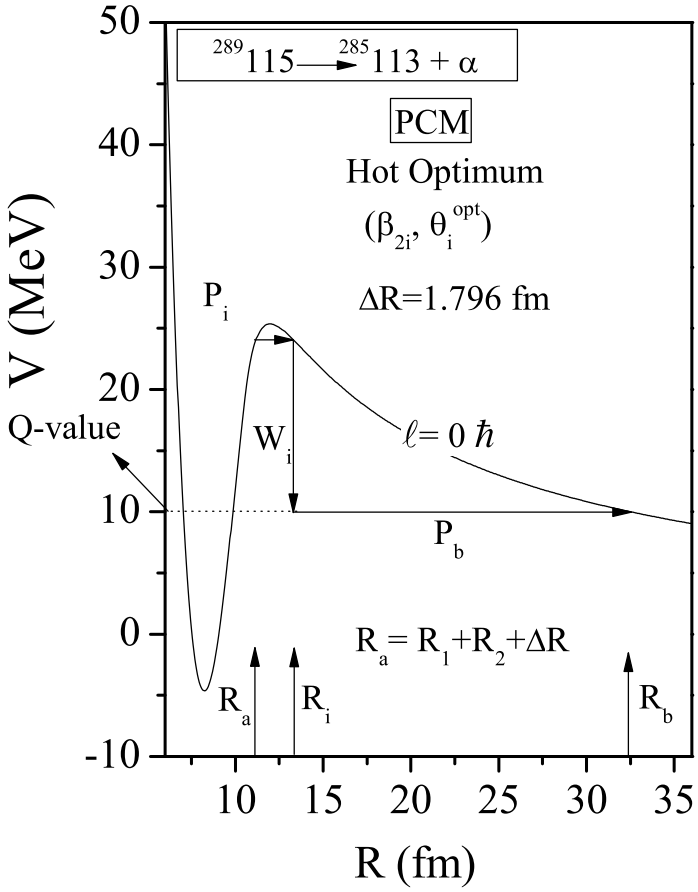

Figure 2.3 A scattering potential, used in the PCM, for α- decay of $^{289}115 \rightarrow {}^{285}113 + \alpha$ [24] at $\ell = 0$, including deformations upto β_{2i}. The path of barrier tunnelling is also shown.

The constants a_i $(i = 1, 2)$ occurring in the polynomial, are determined by using the following boundary conditions:

1. At $R = R_0$, $V(R) = Q$

2. At $R = R_t$, $V(R) = V(R_t)$

Here the first condition is satisfied by considering R=R_b, the outer turning point of the penetration path, with V(R_b)=Q-value. The second condition is satisfied by adding the neck-length parameter in the touching configuration (discussed in section 2.5.3) as R_a= $R_t + \Delta R$, where R_a is considered as the first (inner) turning point as shown in Fig. 2.3.

Following this, the transmission probability P is considered as the three step penetration path, which is shown in Fig. 2.3, for ground state α-decay of $^{289}115$:

1. The penetrability P_i from R_a to R_i,

2. the (inner) de-excitation probability W_i at R_i and

3. the penetrability P_b from R_i to R_b

giving the penetration probability as:

$$P = P_i W_i P_b. \tag{2.48}$$

Following the excitation model of M. Greiner and W. Scheid [56], the de-excitation probability W_i is given as:

$$W_i = \exp(-bE_i) \tag{2.49}$$

This means that the de-excitation process is restricted to only a single transition. If the parameter b were allowed to depend on R_i, it should then become a process of multiple de-excitation and proceed as step-like process. For a heavy cluster decay into the excited states of the daughter nucleus, $b = 0$ is assumed [56], which means W_i=1, therefore,

$$P = P_i P_b, \tag{2.50}$$

where P_i and P_b are calculated by using WKB approximation, as:

$$P_i = \exp\left[-\frac{2}{\hbar}\int_{R_a}^{R_i}\{2\mu[V(R) - V(R_i)]\}^{1/2}dR\right] \tag{2.51}$$

and

$$P_b = \exp\left[-\frac{2}{\hbar}\int_{R_i}^{R_b}\{2\mu[V(R)-Q]\}^{1/2}dR\right] \tag{2.52}$$

The integrals of the Eqs. (2.51) and (2.52) are solved analytically by parameterizing the above calculated potential V (R), as prescribed in [6, 7].

2.5 The Dynamical Cluster Decay Model

The Dynamical cluster decay model (DCM) [11]- [24] for the decay of hot and rotating nucleus (i.e. angular momentum $\ell \neq 0$ and temperature $T \neq 0$) is a reformulation of the Preformed cluster model (PCM) [6]- [10] for ground-state (ℓ=0, T=0) decay of a nucleus. The DCM (like PCM) is based on the dynamical (or quantum mechanical) fragmentation theory [25]- [30]. The deformation and orientation effects are duly taken care along with the influence of temperature and angular momentum in the decay of excited compound nucleus within DCM. The co-ordinates η and R of fragmentation theory in DCM, characterize, respectively,

(i) the nucleon-division (or -exchange) between outgoing fragments, and

(ii) the transfer of kinetic energy of incident channel ($E_{c.m.}$) to internal excitation (total excitation or total kinetic energy, TXE or TKE) of the outgoing channel, since the fixed $R = R_a$, at which the process is calculated, depends on temperature T as well as on η, i.e. $R(T, \eta)$. This energy transfer process follows the relation:

$$E^*_{CN} + Q_{out}(T) = TKE(T) + TXE(T) \tag{2.53}$$

The CN excitation energy $E_{CN}{}^*$ is related to temperature T (in MeV)

$$E^*_{CN} = E_{c.m.} + Q_{in} = (A/a)T^2 - T \qquad (MeV). \tag{2.54}$$

where "a" is the level density parameter, with a = 9 to 11 depending on the mass of the compound nucleus. For superheavy mass region usually A/11 is taken for majority of the cases. Q_{in} is the entrance channel Q-value given by $Q_{in} = B_1 + B_2 - B_{CN}$ where B's are the binding energies.

In terms of the partial wave analysis, using the decoupled approximation to η- and R-motions, the decay cross-section in DCM [11]- [24] is defined as:

$$\sigma = \sum_{\ell=0}^{\ell_{max}} \sigma_\ell = \frac{\pi}{k^2} \sum_{\ell=0}^{\ell_{max}} (2\ell+1) P_0^\ell P_\ell; \qquad k = \sqrt{\frac{2\mu E_{c.m.}}{\hbar^2}} \tag{2.55}$$

where, penetrability P_ℓ refers to R-motion and preformation probability P_0^ℓ to η-motion, both depend on temperature (T) and angular momentum (ℓ). The ℓ_{max}-value in Eq. (2.55) is the maximum angular momentum, fixed for the vanishing of the light particles cross-section, i.e., σ_{ER} (or σ_{xn}, particularly for superheavy nuclei) becoming negligibly small at $\ell = \ell_{max}$. The temperature and angular momentum effects differentiate DCM from the PCM framework. For ℓ=0 (s-wave) $\sigma_0 = \frac{\pi}{k^2} P_0^\ell P_\ell$, is equivalent to decay constant $\lambda = \nu_0 P_0 P$ (or decay half-life $T_{1/2} = ln2/\lambda$). Here one may observe that, σ_0 and λ differ only through the constants $\frac{\pi}{k^2}$ and ν_0. Hence, in DCM the decaying fragments are treated as the dynamical collective mass motion of *preformed clusters or fragments* through the barrier, same as taken in the PCM.

2.5.1 Preformation probability P_0^ℓ

The preformation probability gives the structural information of the CN and obtained by solving the stationary Schrödinger equation in η (see Eq. (2.8)), at a fixed R = R_a. In PCM, the preformation probability is given by the Eq. (2.46), in which temperature and angular momentum effects are silent. On the other hand, the temperature dependence in the preformation factor is included through the use of temperature dependent potential $V_(\eta)$, given by Eq. (2.13). Also, if the system is excited higher values of ν in Eq. (2.45) would also contribute. The possible consequence of such excitations are included here by assuming a Boltzmann like occupation of excited states:

$$|\psi(\eta)|^2 = \sum_{\nu=0}^{\infty} |\psi^\nu(\eta)|^2 \exp\left(-\frac{E_\eta^\nu}{T}\right) \tag{2.56}$$

It is relevant to mention that we are dealing here with the mass (or charge) asymmetry which is a directly measurable quantity, and acts dynamically as mass (or charge) transfer coordinate. Thus, the calculated yields $P_0(A_i)$ (or $P_0(Z_i)$) are directly comparable with experiments.

2.5.2 Penetration probability P_ℓ

Instead of three step penetration path, the barrier penetrability in the DCM is calculated through a single penetration step between R_a and R_b as shown in Fig. 2.4.

R_a is the first turning point of the penetration path which is defined as:

$$R_a(T) = R_t + \Delta R(\eta, T) \tag{2.57}$$

where

$$R_t = R_1(\alpha_1, T) + R_2(\alpha_2, T) \tag{2.58}$$

The temperature dependence in the radius vectors $R_1(\alpha_1, T)$ and $R_2(\alpha_2, T)$ is given by Eq. (2.15). It is relevant to mention here that, the temperature dependence in the penetration probability (P) is introduced through the radius vectors, used to estimate scattering potential which in turn influence the barrier penetration probability.

Due to single turning path, the potential calculated at the first and second turning point remains same and is equal to the effective Q-value of the decaying fragments, given as:

$$V(R_a, \ell) = V(R_b, \ell) = Q_{eff}(T) = TKE(T) \tag{2.59}$$

The Q_{eff}(T) for the decay of hot CN at temperature T, to two exit-channel fragments observed in *ground state* (T=0) is defined by:

$$Q_{eff}(T) \;=\; B(T) - [B_L(T=0) + B_H(T=0)] \tag{2.60}$$

with B's as the respective binding energies.

Hence in DCM, to understand the effective penetration path of the decaying fragments, the total penetrability P_ℓ is used in place of P_i and P_b integrals Eq. (2.51) and Eq. (2.52). The Q-value is replaced by Q_{eff} and the limits of integration are taken from R_a to R_b as depicted in Fig. 2.4.

Therefore P_ℓ is given as:

$$P_\ell = \exp\left[-\frac{2}{\hbar}\int_{R_a}^{R_b}\{2\mu[V(R) - Q_{eff}]\}^{1/2}dR\right] \tag{2.61}$$

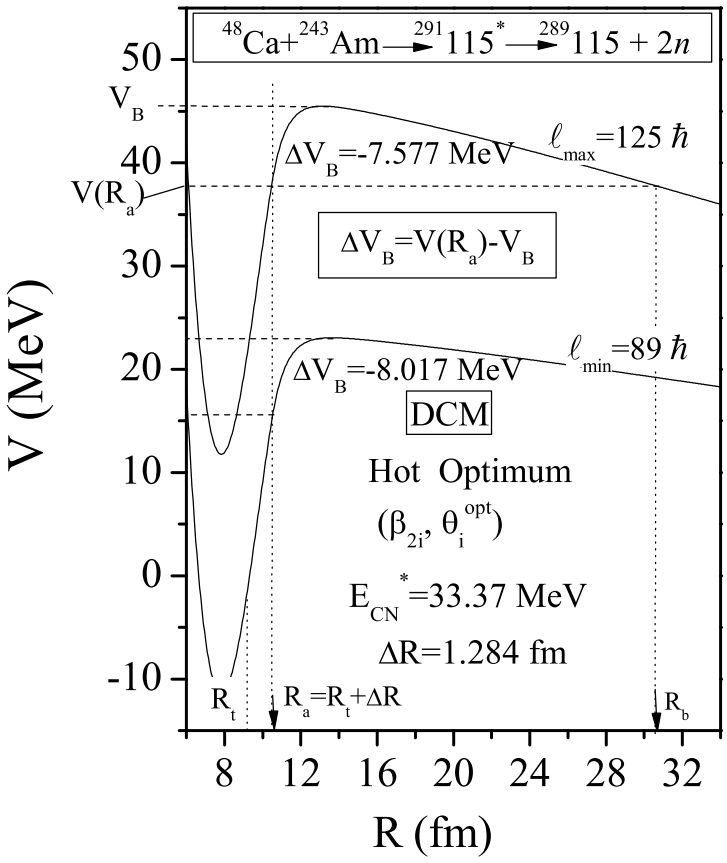

Figure 2.4 The scattering potential for $^{291}115^{*} \rightarrow ^{289}115+2n$ reaction at E^{*}_{CN} =33.37 MeV, calculated at the extreme values of angular momentum. The "barrier lowering parameter" is also shown for ℓ=ℓ_{min} and ℓ=ℓ_{max} values [24].

2.5.3 The neck -length parameter and concept of "barrier lowering"

In the definition of R_a above, ΔR is the relative separation distance between two fragments/ or clusters A_i (marked in Fig. 2.4). In the language of two center shell model (TCSM), used to determine shell effects δU, ΔR is shown to assimilate the neck formation effects [57–59], and hence is referred as the neck-length parameter. This is similar to that used in both the scission-point [60] and saddle-point [61, 62] statistical fission models for calculating the cross-sections. The parameter ΔR decides the first turning point of barrier

penetration, referring to actually used barrier height, and consequently to the concept of "barrier lowering"(see, Eq. (2.62) below).

Note that the predictions based on one dimensional barrier penetration calculations may result in sub-barrier fusion hindrance. One way to fix this problem is to use the coupled channel calculations, in which substantial enhancement in sub-barrier heavy-ion fusion cross-sections can be obtained. The important point to note in coupled-channel calculations is that the enhancement of sub-barrier fusion cross-section arises due to the *effective* barrier height of at-least one of the channels which has a *reduced* barrier. A similar "barrier lowering" is an in-built property of the DCM since, for a best fit to the data, the neck-length parameter ΔR (equivalently R_a) allows us to relate in a simple way the potential $V(R_a, \ell)$ to the top of the barrier $V_B(\ell)$ for each ℓ, by defining their difference $\Delta V_B(\ell)$ as the effective "lowering of barrier", given as:

$$\Delta V_B(\ell) = V(R_a, \ell) - V_B(\ell) \tag{2.62}$$

Here ΔV_B for each ℓ is defined as a negative quantity, the actual barrier height is effectively lowered, as also illustrated in Fig. 2.4 for ℓ_{min} and ℓ_{max} values. It is worth noting in Fig. 2.4 that, ΔV_B is higher for lower angular momentum value. It is relevant to mention here that ΔV_B decreases with increase in energy, being large at lower energies. The detailed description of barrier modification analysis as a function of angular momentum and excitation energy is discussed in the subsequent chapters.

Bibliography

[1] V. M. Strutinsky, Nucl. Phys. A **95**, 420 (1967); Nucl. Phys. A **122**, 1 (1968).

[2] S. Cwiok, J. Dobaczewski, P. H. Heenen, P. Magierski, and W. Nazarewicz, Nucl. Phys. A **611**, 211 (1996).

[3] K. Rutz, M. Bender, T. Burvenich, T. Schilling, P. G. Reinhard, J. A. Maruhn, and W. Greiner, Phys. Rev. C **56**, 238 (1997); J .F. Berger, M. Girod, and D. Gogny, Nucl. Phys. A **428**, 23c (1984).

[4] H. F. Boersma, Phys. Rev. C **48**, 472 (1993).

[5] G. A. Lalazissis, M. M. Sharma, P. Ring, and Y. K. Gambhir, Nucl. Phys. A **608**, 202 (1996).

[6] S. S. Malik and R. K. Gupta, Phys. Rev. C **39**, 1992 (1989).

[7] S. Kumar and R. K. Gupta, Phys. Rev. C **55**, 218 (1997).

[8] S. K. Arun, R. K. Gupta, S. Kanwar, B. B. Singh, and M. K. Sharma, Phys. Rev. C **80**, 034317 (2009).

[9] G. Sawhney, M. K. Sharma, and R. K. Gupta, Phys. Rev. C **83**, 064610 (2011).

[10] R. Kumar and M. K. Sharma, Phys. Rev. C **85**, 054612 (2012).

[11] R. K. Gupta, R. Kumar, N. K. Dhiman, M. Balasubramaniam, W. Scheid, and C. Beck, Phys. Rev. C **68**, 014610 (2003).

[12] M. Balasubramaniam, R. Kumar, R. K. Gupta, C. Beck, and W. Scheid, J. Phys. G: Nucl. Part. Phys. **29**, 2703 (2003).

[13] R. K. Gupta, M. Balasubramaniam, R. Kumar, D. Singh, and C. Beck, Nucl. Phys. A **738**, 479c (2004); R. K. Gupta, M. Balasubramaniam, R. Kumar, D. Singh, C. Beck, and W. Greiner, Phys. Rev. C **71**, 014601 (2005).

[14] B. B. Singh, M. K. Sharma, R. K. Gupta, and W. Greiner, Int. J. Mod. Phys. E **15**, 699 (2006).

[15] B. B. Singh, M. K. Sharma, and R. K. Gupta, Phys. Rev. C **77**, 054613 (2008).

[16] S. Kanwar, M. K. Sharma, B. B. Singh, R. K. Gupta, and W. Greiner, Int. J. Mod. Phys. E **18**, 1453 (2009); S. K. Arun, R. Kumar, and R. K. Gupta, J. Phys. G: Nucl. Part. Phys. **36**, 085105 (2009).

[17] M. K. Sharma, G. Sawhney, S. Kanwar, and R. K. Gupta, Mod. Phys. Lett. A **25**, 2022 (2010); M. K. Sharma, G. Sawhney, R. K. Gupta, and W. Greiner, J. Phys. G: Nucl. Part. Phys. **38**, 105101 (2011).

[18] M. K. Sharma, S. Kanwar, G. Sawhney, R. K. Gupta, and W. Greiner, J. Phys. G: Nucl. Part. Phys. **38**, 055104 (2011); D. Jain, R. Kumar, M. K. Sharma, and R. K. Gupta, Phys. Rev. C **85**, 024615 (2012).

[19] M. Kaur and M. K. Sharma, Phys. Rev. C **85**, 054605 (2012); M. Kaur, M. K. Sharma, and R. K. Gupta, Phys. Rev. C **86**, 064610 (2012).

[20] G. Kaur and M. K. Sharma, Nucl. Phys. A **884**, 36 (2012); G. Kaur and M. K. Sharma, Phys. Rev. C **87**, 044601 (2013).

[21] K. Sandhu and M. K. Sharma, AIP Conf. Proc. **1524**, 123 (2013).

[22] K. Sandhu, M. K. Sharma, A. Kaur, and R. K. Gupta, Phys. Rev. C **90**, 034610 (2014).

[23] K. Sandhu, M. K. Sharma, and R. K. Gupta, Phys. Rev. C **85**, 024604 (2012); K. Sandhu, M. K. Sharma, and R. K. Gupta, Phys. Rev. C **86**, 064611 (2012); K. Sandhu and M. K. Sharma, Braz. J. Phys. **44**, 64 (2014).

[24] R. Kumar, K. Sandhu, M. K. Sharma, and R. K. Gupta, Phys. Rev. C **87**, 054610 (2013).

[25] J. Maruhn and W. Greiner, Phys. Rev. Lett. **32**, 548 (1974).

[26] H. J. Fink, W. Greiner, R. K. Gupta, S. Liran, J. H. Maruhn, W. Scheid, and O. Zohni, in Proceedings of Int. Conf. on Reaction between Complex Nuclei, Nashville, 1974, 21, (Amsterdam: North Holland), pages 2.

[27] R. K. Gupta, W. Scheid, and W. Greiner, Phys. Rev. Lett. **35**, 353 (1975).

[28] S. Yamaji, W. Scheid, H. J. Fink, and W. Greiner, Z. Phys. A **278**, 69 (1976); S. Yamaji, W. Scheid, H. J. Fink, and W. Greiner, J. Phys. G: Nucl. Part. Phys. **2**, L189 (1976); S. Yamaji, K. H. Ziegenhain, H. J. Fink, W. Greiner, and W. Scheid, J. Phys. G: Nucl. Part. Phys. **3**, 1283 (1977).

[29] A. Săndulescu, H. J. Lustig, J. Hahn, and W. Greiner, J. Phys. G: Nucl. Part. Phys. **4**, L279 (1978); H. J. Lustig, J. A. Maruhn, and W. Greiner, J. Phys. G: Nucl. Part. Phys. **6**, L25 (1980).

[30] R. K. Gupta, IANCAS Bull. (India), **6**, 2 (1990).

[31] H. Kröger and W. Scheid, J. Phys. G: Nucl. Part. Phys. **6**, L85 (1980).

[32] R. K. Gupta, N. Singh, and M. Manhas, Phys. Rev. C **70**, 034608 (2004).

[33] G. Audi, A. H. Wapstra, and C. Thibault, Nucl. Phys. A **729**, 337 (2003).

[34] P. Möller, J. R. Nix, W. D. Myers, and W. J. Swiatecki, At. Data Nucl. Data Tables **59**, 185 (1995).

[35] N. J. Davidson, S. S. Hsiao, J. Markram, H. G. Miller, and Y. Tzeng, Nucl. Phys. A **570**, 61c (1994).

[36] P. A. Seeger, Nucl. Phys. **25**, 1 (1961).

[37] S. DeBenedetti, Nuclear Interactions (New York: Wiley) (1964).

[38] G. Audi and A. H. Wapstra, Nucl. Phys. A **595**, 409 (1995).

[39] W. Myers and W. J. Swiatecki, Nucl. Phys. **81**, 1 (1966).

[40] R. K. Gupta, Niyti, M. Manhas, and W. Greiner, J. Phys. G: Nucl. Part. Phys. **36**, 115105 (2009).

[41] Niyti, R. K. Gupta, and W. Greiner, J. Phys. G: Nucl. Part. Phys. **37**, 115103 (2010).

[42] R. K. Gupta, M. Balasubramaniam, R. Kumar, N. Singh, M. Manhas, and W. Greiner, J. Phys. G: Nucl. Part. Phys. **31**, 631 (2005).

[43] M. Münchow, D. Hahn, and W. Scheid, Nucl. Phys. A **388**, 381 (1982); M. J. Rhoades-Brown, V. E. Oberacker, M. Seiwert, and W. Greiner, Z. Phys. A **310**, 287 (1983); C. Y. Wong, Phys. Rev. Lett. **31**, 766 (1973).

[44] J. Blocki, J. Randrup, W. J. Swiatecki, and C. F. Tsang, Ann. Phys. (NY) **105**, 427 (1977).

[45] W. D. Myers and W. J. Swiatecki, Phys. Rev. C **62**, 044610 (2000).

[46] Deryagin, Kolloid Z. **69**, 155 (1934).

[47] W. D. Myers and W. J. Swiatecki, Ann. Phys. **55**, 395 (1969); Nucl. Phys. A **336**, 267 (1980).

[48] C. W. de Jager, H. de Vries, and C. de Vries, At. Data Nucl. Data Tables **14**, 479 (1974); H. de Vries, C. W. de Jager, and C. de Vries, At. Data Nucl. Data Tables **36**, 495 (1987).

[49] B. Nerlo-Pomorska and K. Pomorski, Z. Phys. A **348**, 169 (1994); B. Nerlo-Pomorska and B. Mach, At. Data Nucl. Data Tables **60**, 287 (1995).

[50] S. Kailas (private communication).

[51] G. A. Pik-Pichak, Fiz. Elem. Chastits At. Yadra **44**, 1421 (1986); B. Buck and A. C. Merchant, J. Phys. G: Nucl. Part. Phys. **15**, 615 (1989); A. Sandulescu, R. K. Gupta, W. Greiner, F. Carstoiu, and M. Horoi, Int. J. Mod. Phys. E **1**, 379 (1992).

[52] D. N. Poenaru, M. Ivascu, A. Sandulescu, and W. Greiner, Phys. Rev. C **32**, 572 (1985); D. N. Poenaru, W. Greiner, K. Depta, M. Ivascu, D. Mazilu, and A. Sandulescu, At. Data Nucl. Data Tables **34**, 423 (1986); D. N. Poenaru, R. A. Gherghescu, and W. Greiner, Phys. Rev. Lett. **107**, 062503 (2011); D. N. Poenaru, R. A. Gherghescu, and W. Greiner, Phys. Rev. C **85**, 034615 (2012).

[53] R. Blendowske, T. Fliessbach, and H. Walliser, Nucl. Phys. A **464**, 75 (1987).

[54] R. Blendowske and H. Walliser, Phys. Rev. Lett. **61**, 1930 (1988).

[55] G. Gamov, Z. Phys. **51**, 204 (1928).

[56] M. Greiner and W. Scheid, J. Phys. G: Nucl. Part. Phys. **12**, L229 (1986).

[57] S. Kumar and R. K. Gupta, Phys. Rev. C **55**, 218 (1997).

[58] H. S. Khosla, S. S. Malik, and R. K. Gupta, Nucl. Phys. A **513**, 115 (1990).

[59] R. K. Gupta, S. Kumar, and W. Scheid, Int. J. Mod. Phys. E **6**, 259 (1997).

[60] T. Matsuse, C. Beck, R. Nouiner, and D. Mahboub, Phys. Rev. C **55**, 1380 (1997).

[61] S. J. Sanders, D. G. Kovar, B. B. Back, C. Beck, D. J. Henderson, R. V. F. Janssens, T. F. Wang, and B. D. Wilkins, Phys. Rev. C **40**, 2091 (1989).

[62] S. J. Sanders, Phys. Rev. C **44**, 2676 (1991).

Chapter 3

Neutron-evaporation and magicity effects in the SH-region

In this chapter, first the role of Z=114, 120, 126 and N=184 is evaluated for the decay of $^{296}116^{*}$ [1] and $^{266}\mathrm{Rf}^{*}$ [2] compound nuclei, using sticking (I_S) and non-sticking (I_{NS}) moments of inertia respectively. The high magnitude of the preformation probability, or low values of the fragmentation potential, suggest that among all magic (Z, N) pairs, Z=126 and N=184 are the strongest superheavy magic shell closures required to address the neutron evaporation decay. This observation is in agreement with earlier calculations [3], carried out by using I_S approach for Z=112 nucleus.

In view of the above magicity criteria, Z=126 and N=184 shell closures are used to analyze the $2n$, $3n$ and $4n$ channels of $^{297}117^{*}$ superheavy nuclear system in the framework of the Dynamical cluster decay model (DCM) [1]- [6]. The aim of this work, published in [4], is to investigate the role of deformations in the decay of $^{297}117^{*}$ as the production cross-sections cannot be fitted for spherical considerations of incoming nuclei and/or decay fragments. On the other hand, with inclusion of deformation effects up to quadrupole deformations (β_{2i}), and "optimum" orientations (θ_i^{opt}), the σ_{2n} and σ_{3n} cross-sections are

fitted nicely, but σ_{4n} is still underestimated by about 25% which indicates the possibility of some other competing evaporation residue, like the ^{4}He decay contributing toward $4n$-decay cross-sections. Also, a possible contribution of fusion-fission component is predicted which, together with ^{4}He decay, need experimental verification.

In the following, a brief introduction regarding the present work is reported in Sec. 3.1. On the other hand, Sec. 3.2 presents the results related to magic shell closures required for superheavy mass region. Further, within this section, the decay of $^{297}117^{*}$ is discussed by applying the best suited magic pair. Finally, the results are summarized in Sec. 3.3.

3.1 Introduction

The synthesis of superheavy nuclei is an important and exciting research area of nuclear physics. Since the survival of a superheavy nuclear system against prompt disintegration depends largely on the nuclear properties of proton and neutron quantum states, the existence of superheavy nuclei ($Z \geq$103) contribute immensely towards the basic ideology of nuclear potentials and related nuclear structure effects, which in turn compensates the large Coulomb repulsive interaction. For this, the proper choice of the magic numbers in the superheavy region is extremely important, since superheavy nuclear systems in the vicinity of the closed shells would exhibit considerable increase in nuclear stability against various decay modes. It is relevant to mention here that N=184 is almost an established shell closure (Magic) in superheavy region after N=126. Therefore, reactions involving neutron number closer to 184 are expected to be relatively stable. Unlike, neutron magic number, the status of proton magic in superheavy region is still not clear and Z=114, 120 and 126 [7]- [10] have emerged as most probable candidates among proton shell closures in superheavy region.

In a recent experiment [11], to reach the predicted stable land of superheavy nuclei, two new isotopes ^{293}117 and ^{294}117 were produced in a fusion reaction between ^{48}Ca projectile and radioactive ^{249}Bk target, followed by $4n$ and $3n$ emission, respectively. The production of these daughter nuclei provided an additional experimental support to address the island of stability for superheavy nuclei, as both have high neutron excess (N=176 and 177) and hence are relatively closer to the neutron shell closure N=184.

Following the above discussion, an attempt is made to address the best possible candidates of magic shells for the superheavy mass region by analyzing the decay patterns of ^{296}116* and ^{266}Rf* nuclei in DCM framework [1]- [6]. Further, the application of most suited shell closures is explored to understand the decay of ^{297}117* compound nucleus, for which the neutron evaporation cross-sections of $3n$ and $4n$ channels have been measured at two different compound nucleus excitation energies E^{*}_{CN}=35.3 and 39.3 MeV [11]. More precisely, only σ_{3n} is measured at E^{*}_{CN}=35.3 MeV and σ_{4n} at E^{*}_{CN}=39.3 MeV. Also, some theoretical estimates [12–14] are available for the $2n$ decay, but the contribution of σ_{2n} is not seen in the experiments since the reaction used is apparently a hot fusion reaction.

3.2 Calculations and Results

As stated above, the earlier calculations [3], done for ^{286}112*, suggested that Z=126 and N=184 is the best possible choice for proton and neutron magic numbers for evaluating neutron evaporation decay channels. This observation is limited to the dynamics of only one nucleus i.e. ^{286}112* and the predictions were made mainly for sticking moment of inertia alone. In order to generalize this result, the role of shell closure effect in superheavy region is investigated by understanding the decay of ^{296}116* and ^{266}Rf* nuclei with sticking and non-sticking moments of inertia respectively, using the Dynamical cluster-decay model

(DCM). Calculations are made for three set of magic pairs (a) Z=126 and N=184, (b) Z=120 and N=184, (c) Z=114 and N=184. The effect of each pair is then observed on the fragmentation potential, preformation probability and production cross-sections of the superheavy nuclei.

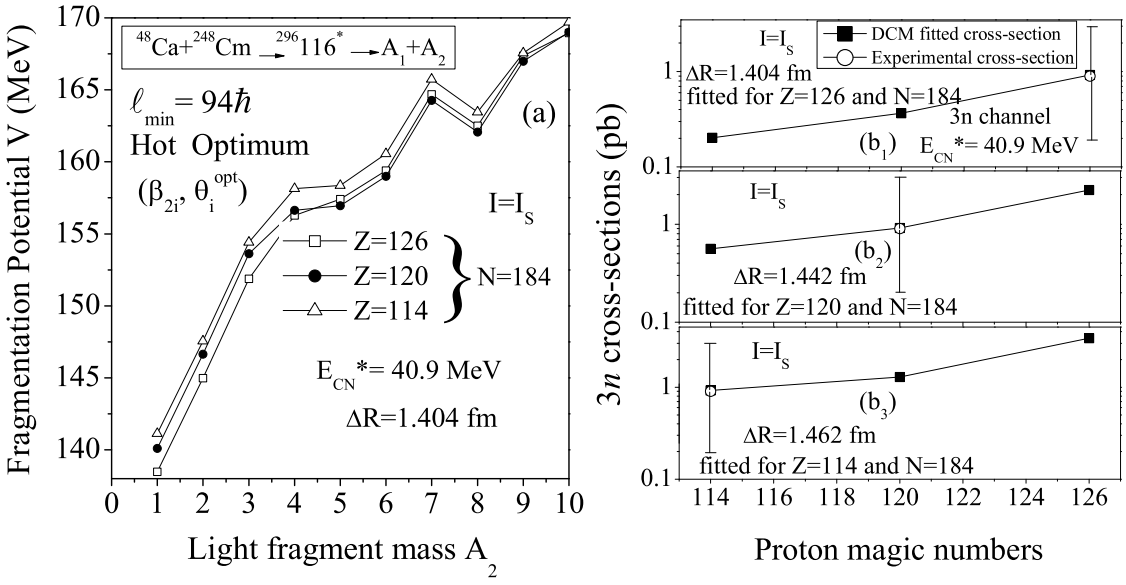

Figure 3.1 (a) Comparison of fragmentation potential as a function of light fragment mass for three choices of magic numbers Z=126, 120, 114 and N=184, same value of ΔR is taken for all the magic shell cases. (b) Measured and calculated 3*n*-cross-sections as function of proton magic numbers. Calculations are done for three set of magic pairs, using sticking (I_S) moment of inertia. In each panel, the ΔR is kept same for the remaining two cases.

In order to explore the effect of magic pairs on the fragmentation potential of $^{296}116^{*}$, Fig. 3.1 (a) is plotted as the function of light fragment mass (A_2) for all the three magic shell closures at E^{*}_{CN}= 40.9 MeV, by including deformations upto β_{2i} within 'optimum orientation' approach. The reported ΔR=1.404 fm, corresponds to the best fitted value for Z=126 and N=184 case and is kept same for other two proton magic numbers i.e. Z=114 and 120 for the sake of comparison. Fig. 3.1 (a) shows that neutron evaporation of 1*n*, 2*n*, 3*n* and 4*n* neutron clusters (i.e. ER channels) lie highest in energy for the case of Z=114 and N=184, and lowest for Z=126 and N=184. Due to lower fragmentation

potential, Z=126 and N=184 can probably be taken as the better magic pair among others to address the neutron decay of $^{296}116^{*}$ nucleus.

In addition to this, Fig. 3.1 (b) is plotted which shows the calculated $3n$-evaporation residue cross-sections of $^{296}116^{*}$, compared with the experimental data [15] at E^{*}_{CN}= 40.9 MeV, with fitted values of ΔR for all the magic shell closures. In Fig. 3.1 (b_1), the value of ΔR is taken fixed for the case of Z=126 and N=184, and at same value of ΔR, the cross-sections for Z=120 and N=184, Z=114 and N=184 are calculated. This step is repeated for Z=120 and Z=114 magic shells respectively in Fig. 3.1 (b_2) and 3.1 (b_3). Interestingly, the $3n$- cross-sections remains lowest for the case of Z=114 and N=184, and highest for the case of Z=126 and N=184 for all the three considerations. This supports the result of lower fragmentation potential in Fig. 3.1 (a) for Z=126 and N=184 magic shell closures, since deeper minima leads to higher magnitude of cross-sections.

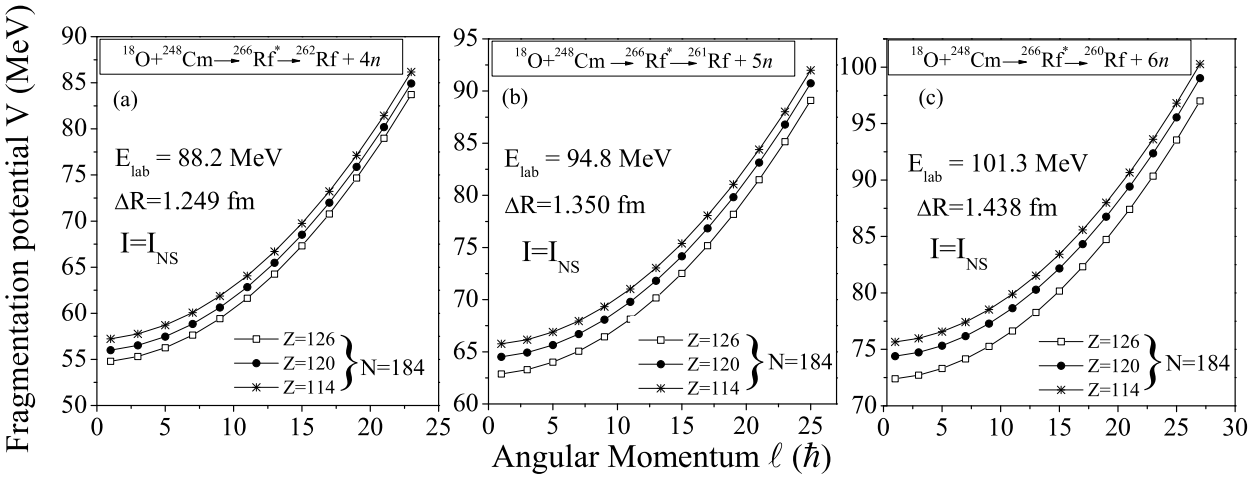

Figure 3.2 Variation of fragmentation potential as a function of angular momentum, using non-sticking moment of inertia (I_{NS}) for (a) $4n$, (b) $5n$ and (c) $6n$ decay channels, at different E_{lab} energies, using Z=126, 120, 114 and N=184 magic shell pairs.

To generalize this concept for the whole superheavy mass range, the $4n$, $5n$ and $6n$ decay of much lighter superheavy nucleus ^{266}Rf* [16] is also worked out to confirm the dominance of Z=126 and N=184 on the other magic pairs. The calculations are carried for

β_{2i}-deformations with 'hot optimum' orientations, same as that of $^{296}116^*$ nuclei, but for the use of non-sticking moment of inertia (I_{NS}). For the decay of $^{266}Rf^*$ compound nucleus, the fragmentation potential plotted as a function of angular momentum in Fig. 3.2 shows lesser magnitude for Z=126 and N=184 magic shells in $4n$, $5n$ and $6n$ channels reported at beam energies E_{Lab}= 88.2, 94.8 and 101.3 MeV . This observation is further supported in Fig. 3.3 which shows the variation of preformation probability (P_0) as the function of light fragment mass (A_2) at ℓ_{min}=15$\hbar$, 16$\hbar$ and 18$\hbar$. It is evident from Fig. 3.3 that at ℓ_{min}, the preformation probability remains highest for Z=126 and N=184 superheavy magic pair, which is in agreement with the results of Fig. 3.2 for the fragmentation potential. Hence, it seems appropriate to say that proton magic Z=126 and neutron magic N=184 are the best superheavy magic numbers amongst the Z=126, 120, 114 and N=184, to address neutron evaporation channel.

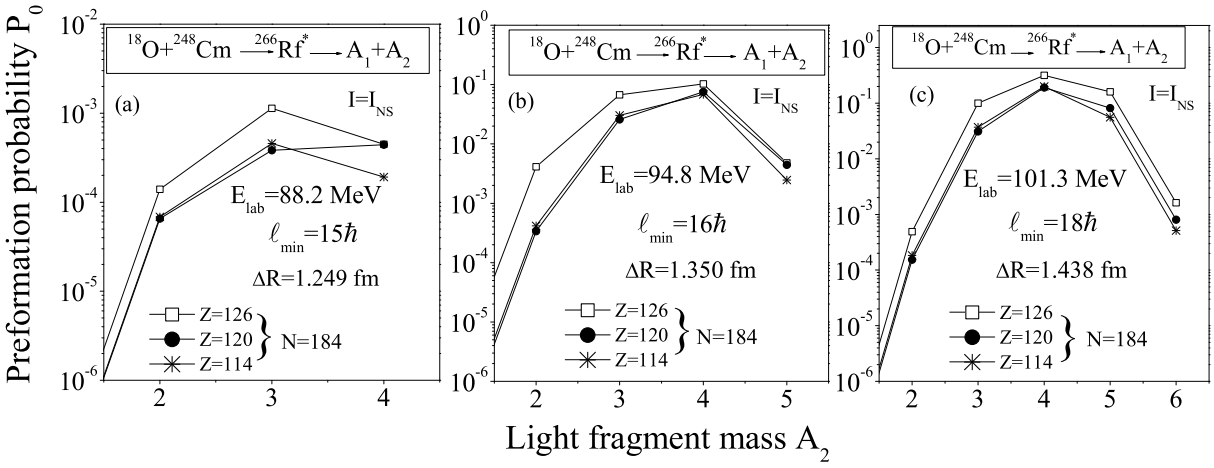

Figure 3.3 Variation of preformation probability (P_0) as a function of light fragment mass at $\ell = \ell_{min}$ for Z=126, 120, 114 and N=184 magic pairs at (a) 88.2 MeV (b) 94.8 MeV and (c) 101.3 MeV beam energies for the decay of $^{266}Rf^*$ nucleus. For all the three cases of magic pairs, the magnitude of ΔR is taken same.

Following the above discussion, the magic shell closures Z=126 and N=184 are applied to study the dynamics of various superheavy nuclei such as $^{297}117^*$ [4],$^{291}115^*$ [5] and

$^{290,292}114^{*}$ [6], to address neutron evaporation channels. In this chapter, the application of Z=126 and N=184 magic shell closures is tested to understand the $2n$, $3n$ and $4n$- decay channels of $^{297}117^{*}$ CN formed in ^{48}Ca+^{249}Bk reaction, the results of other superheavy systems are discussed in the subsequent chapters. In the decay analysis of $^{297}117^{*}$ following points are investigated: (i) The role of β_{2i}-deformations in the decay process, (ii) the role of temperature and angular momentum in the fragmentation process, (iii) barrier modification effects in Z=117 nucleus for the nuclear proximity potential used.

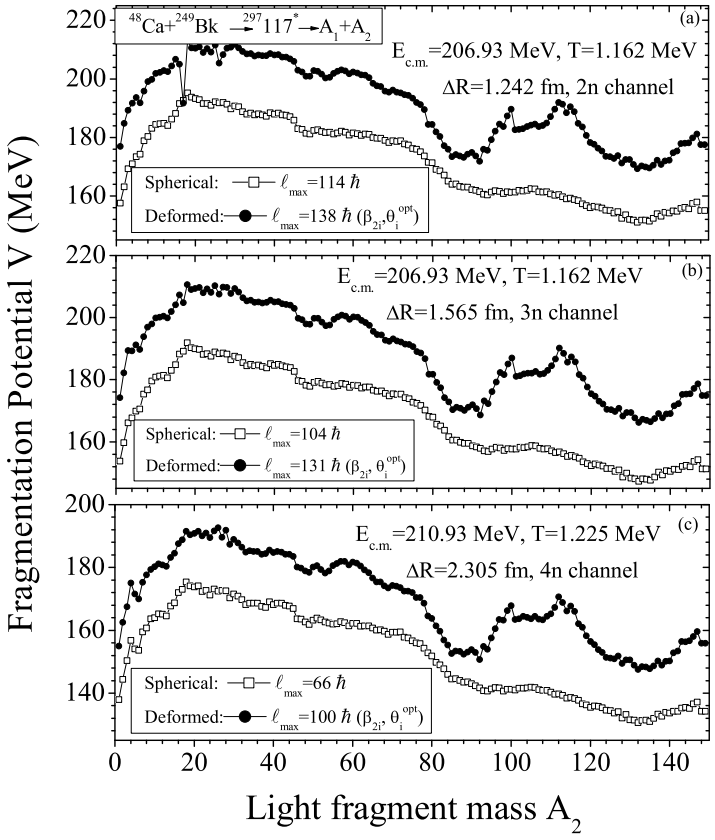

Figure 3.4 Fragmentation potentials for the decay of $^{297}117^{*}$ compound nucleus as a function of light fragment mass (A_2) for spherical and β_{2i}-deformed case at ℓ_{max} values. The fragmentation path is plotted at the neck length (ΔR) parameters of $2n$, $3n$ and $4n$ decay channels, fitted for the deformed case.

First of all, in order to investigate the role of deformations in the decay of Z=117 nucleus, the fragmentation potentials $V(A_2)$ are calculated for spherical nuclei (illustrated in Fig. 3.4, open squares, for xn, x=2, 3 or 4, decays, at the ℓ_{max}-values), and attempted

to fit the only parameter of the model, the neck length ΔR, to the measured cross-sections at both $E_{c.m.}$=206.93 and 210.93 MeV. Interestingly, the measured values of σ_{3n} and σ_{4n} cannot be achieved for any reasonable choice of ΔR. Faced with this situation, the deformations of nuclei up to quadrupole (β_{2i}) deformations are included, allowing "optimum" orientations (θ_i^{opt}). The resulting fragmentation potentials to address $2n$ and $3n$ decays at $E_{c.m.}$=206.93 MeV, and $4n$ decay at $E_{c.m.}$=210.93 MeV for the best fitted ΔR and ℓ_{max} values, are plotted in Fig. 3.4 (solid circles), compared with the $V(A_2)$ for spherical nuclei at the same neck length parameter (open squares).

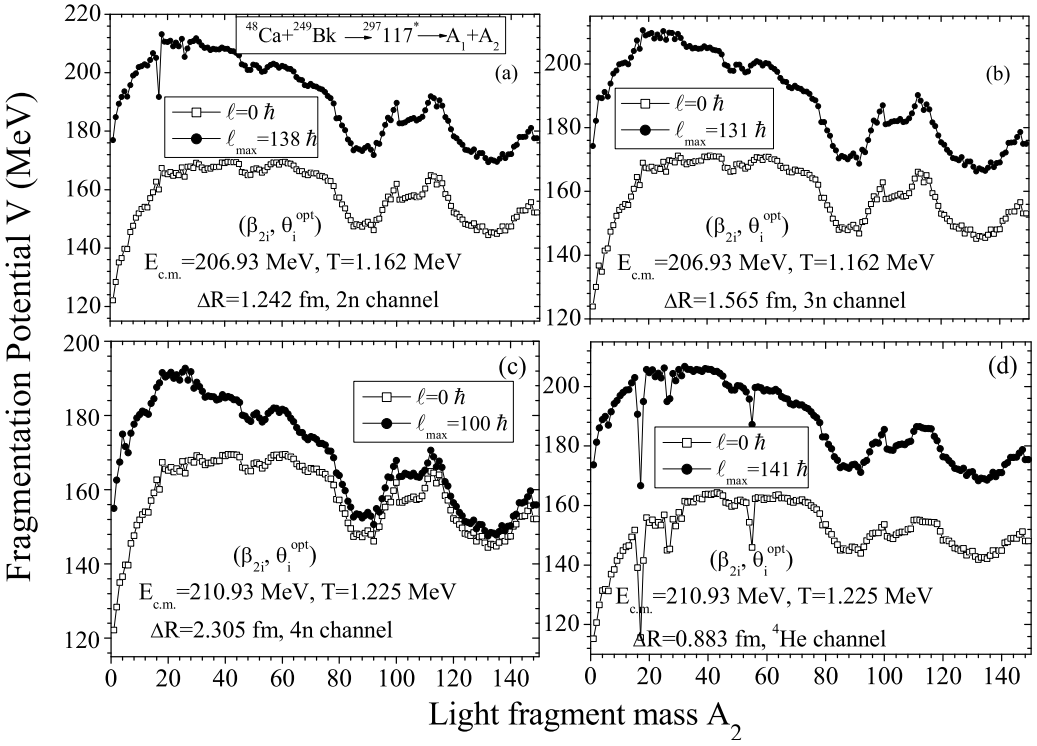

Figure 3.5 Same as Fig 3.4, but for only deformed and oriented nuclei at ℓ=0 and ℓ_{max} values, and for ^{4}He decay channel also.

It is noticed in Fig. 3.4 that whereas the potential energy surfaces with deformations and orientations included show interesting structure with maxima and minima, the surfaces for spherical nuclei are smooth, although the two surfaces (with and without deformations) are similar for the evaporation decay channels $2n$, $3n$ and $4n$. For the

deformed case, two strong minima are seen nearly at A_2 =82-95 and A_2 =122-143, which refer to the (not yet observed) possible fusion-fission channel in the decay of $^{297}117^*$ CN. Another point of difference to note is that the ℓ_{max} for the spherical case is relatively small, compared to the same for deformed nuclei, and independent of deformation effects, the ℓ_{max} value decreases as the number of neutrons in the decay channel increases. Next, to see the effect of changing the ℓ value, the fragmentation potentials at two extreme ℓ-values, ℓ=0 and ℓ_{max} is plotted in Fig. 3.5, with deformation and orientation effects included for the decay of $^{297}117^*$ nuclei. The fragmentation potentials are plotted at the best fit values of the neck-length parameters, associated with the $2n$, $3n$, $4n$ and ^{4}He decay channels. The relevance of ^{4}He decay channel is discussed later in Table 3.1 and Fig. 3.8. Interestingly, the structure of $V(A_2)$ is nearly independent of the ℓ-value for all evaporation channels and fusion-fission decay channels.

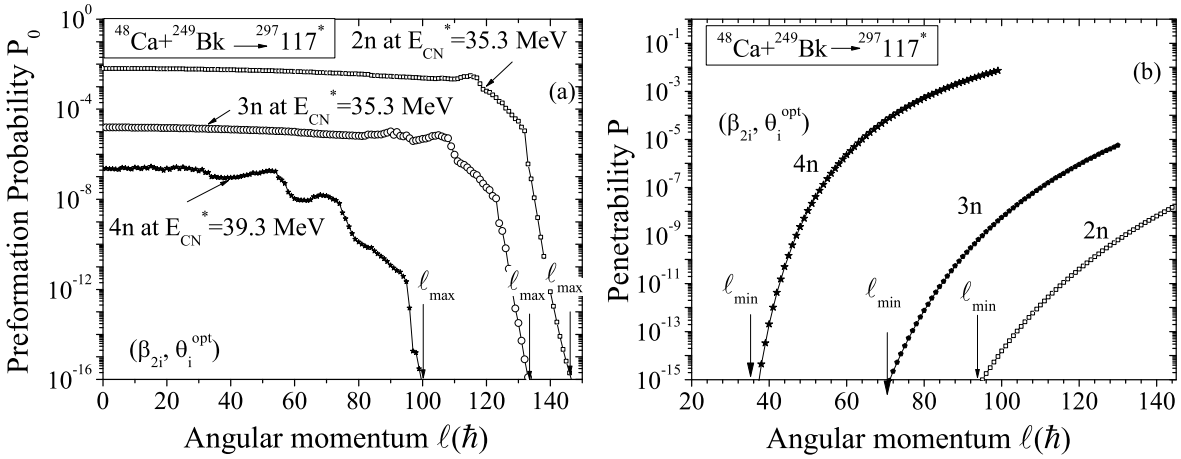

Figure 3.6 (a) The variation of preformation probability (P_0) with angular momentum (ℓ) in the reaction ^{48}Ca+^{249}Bk$\rightarrow^{297}117^*$, for the case with effects of deformations and orientations included. (b) Same as (a), but for the WKB penetration probability (P).

As the compound nucleus (CN) decay cross-section in DCM depends on the preformation probability (P_0) and penetrability (P), first one may observe how these two quantities contribute to the decay process of Z=117 CN. The preformation probability (P_0) helps

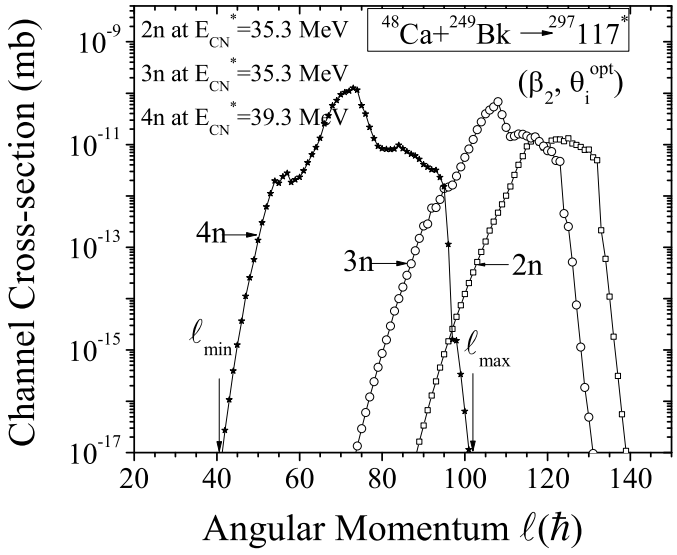

Figure 3.7 Channel cross-section (σ_{xn}) plotted as the function of angular momentum (ℓ). The minimum and maximum angular momentum values ℓ_{min} and ℓ_{max}, respectively, illustrated for $4n$-decay channel.

to fix the maximum value of angular momentum (ℓ_{max}), used for calculating the reaction cross-section. Fig. 3.6 (a) shows P_0 as a function of ℓ, and ℓ_{max} is decided where the P_0 for light particles (evaporation residues) tends to zero. The ℓ_{max}-values are 145 $\hbar$, 131 $\hbar$, and 100 $\hbar$ respectively for $2n$, $3n$ and $4n$ decays. Clearly, P_0 contributes significantly up to a certain ℓ-state and then drops sharply near the ℓ_{max} value. Also note that, as expected from our earlier result from Fig. 3.4, the $4n$-decay corresponds to lower ℓ_{max} state, as compared to the $3n$ and $2n$ decay channels. Next the penetrability (P) is also plotted as function of angular momentum (ℓ) in Fig. 3.6 (b) for $2n$, $3n$ and $4n$ clusters. It is observed that the P goes on increasing as ℓ increases, and a lower limit of $\ell = \ell_{min}$ can be set, which simply means that all ℓ states with ℓ-values less than the ℓ_{min}-value do not contribute significantly to the cross-section because the penetrability (P) is then very small. From Fig. 3.6 (b), the ℓ_{min}=95 $\hbar$, 72 $\hbar$ and 38 $\hbar$ can be calculated, respectively, for $2n$, $3n$ and $4n$ decays. Note that, like ℓ_{max}, ℓ_{min} is also the largest for the $2n$-decay, followed by $3n$ and $4n$ decays. Thus, there is a range of ℓ between ℓ_{min} and ℓ_{max} where both the

preformation probability (P_0) and penetrability (P) contribute significantly. Comparison of Fig. 3.6 (a) with Fig. 3.6 (b) clearly shows that the lower ℓ states contribute more to P_0 and the larger ones contribute effectively to P.

Having defined contributing ℓ-window as $\ell_{min} \leq \ell \leq \ell_{max}$ from P_0 and P, one can calculate the cross-sections for various evaporation residue channels and re-fix the limiting values again for each decay. This is depicted in Fig. 3.7, where x-neutron (x=2, 3 and 4) cross-sections are plotted as function of ℓ for the CN $^{297}117^*$. The cross-sections are significant only in the range of ℓ between 90 $\hbar$ and 138 $\hbar$, 74 $\hbar$ and 131 $\hbar$ and 41 $\hbar$ and 100 $\hbar$, respectively, for $2n$, $3n$ and $4n$ decays. Note that, since the cut-off point is arbitrary, ℓ values can change by ± 2 units, but the change in total cross-section is insignificant.

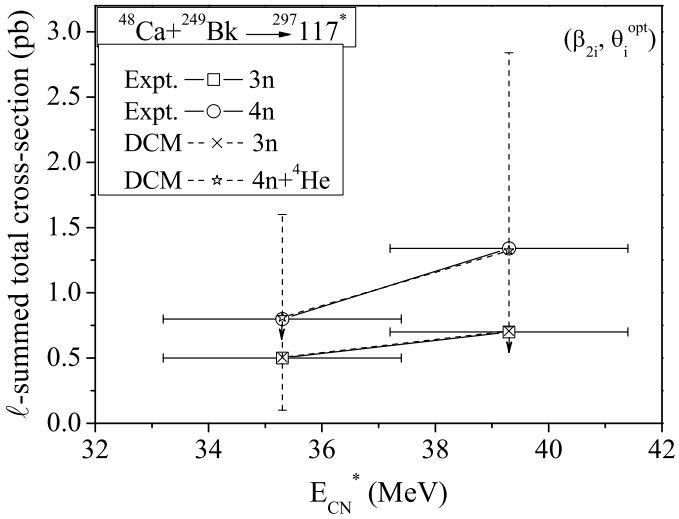

Figure 3.8 Total DCM calculated cross-sections σ_{3n} and σ_{4n+^4He} for the decay of $^{297}117^*$, plotted as the function of E^*_{CN}, and compared with experimental data [11]. The lower limits of data are shown by downwards arrows.

The total decay cross-sections calculated in the DCM are compared, in Fig. 3.8 and Table 3.1, with experimental values [11] and other available calculations [12–14] for $2n$, $3n$ and $4n$ decay channels at the two excitation energies. Table 3.1 clearly shows that DCM calculated $2n$ and $3n$ cross-sections compare nicely with the experimental as well as theoretical data, but the $4n$ cross-sections are underestimated by about 25%, which

Table 3.1 Experimental and DCM calculated evaporation residue cross-sections σ_{xn}, x=2, 3 and 4, in the decay of $^{297}117^{*}$ formed in the ^{48}Ca+^{249}Bk reaction, compared with other available results.

						σ_{xn} (pb)			
E^*_{CN} (MeV)	T (MeV)	xn	ℓ_{max} ($\hbar$)	ΔR (fm)	Expt. [11]	DCM	[12]	[13]	[14]
35.3 ± 2.1	1.162	2n	138	1.242	-	0.2	0.2	0.01	-
		$3n$	131	1.565	$0.5\pm^{1.1}_{0.4}$	0.506	0.9	0.8	1.2
		$4n$	91	2.420	≤ 0.8	0.463	0.1	0.1	0.7
		^{4}He	140	0.889	-	0.349	-	-	-
		$4n$+^{4}He				0.812			
39.3 ± 2.1	1.225	2n	141	1.238	-	0.299	0.3	-	-
		$3n$	132	1.551	≤ 0.7	0.707	2	0.3	0.6
		$4n$	100	2.305	$1.3\pm^{1.5}_{0.6}$	1.02	1	0.3	0.8
		^{4}He	141	0.883	-	0.304	-	-	-
		$4n$+^{4}He				1.324			

indicates the possibility that some other competing decay channel, like the ^{4}He decay, is contributing towards the $4n$-decay cross-sections. Interestingly, if the ^{4}He contribution is included in DCM (also shown in Fig. 3.8), i.e., $\sigma_{4n} + \sigma_{^4He}$ is calculated, the available data is fitted quite nicely.

Finally, the "barrier lowering" parameter (ΔV_B) as a function of E^*_{CN} is plotted in the Fig. 3.9 (a), for neutron evaporation residues at $\ell = \ell_{max}$. Apparently, ΔV_B for each neutron decay channel remains almost constant, nearly independent of the compound nucleus excitation energy. The barrier modification is minimum for $4n$ decay, the case of lowest ℓ_{max} value, followed by $3n$ ($2n$) decay channel, having larger (largest) ℓ_{max} value. Also, the variation of barrier lowering parameter (ΔV_B) with angular momentum is studied for the $3n$ decay channel at E^*_{CN}=35.3 MeV and the $4n$ channel at E^*_{CN}=39.3 MeV. Fig. 3.9 (b) shows that ΔV_B depends strongly on angular momentum (ℓ). It decreases with increase in ℓ, independent of decay channel, i.e., larger barrier modification is needed for lower angular momentum states.

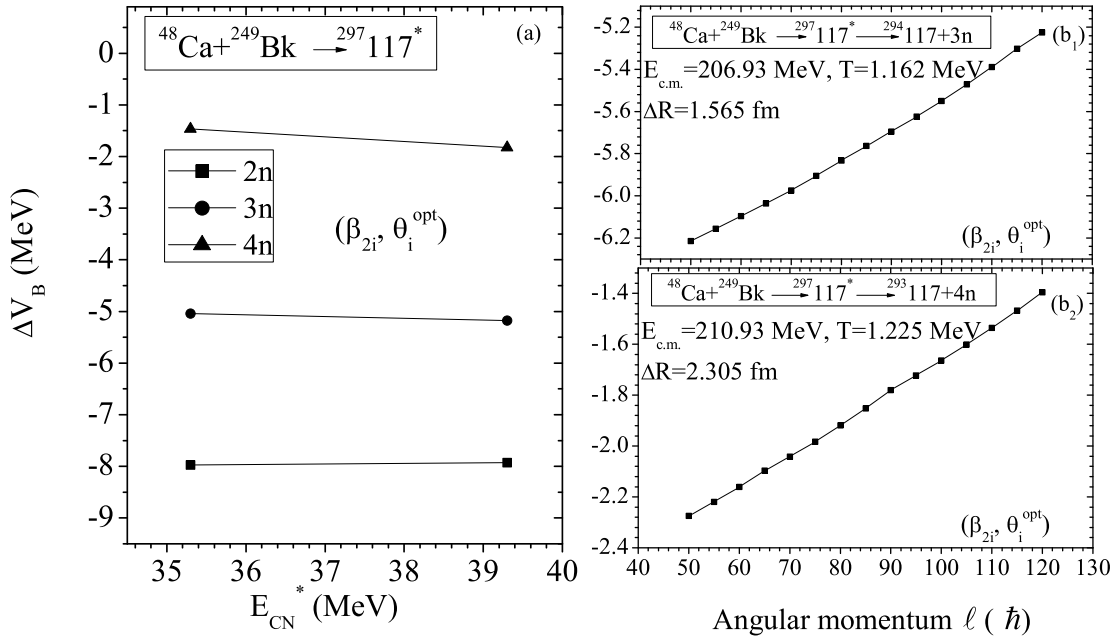

Figure 3.9 (a) Variation of ΔV_B as a function of E^*_{CN} for the xn decay of $^{297}117^*$, for $\ell = \ell_{max}$ case.(b) Variation of ΔV_B as function of ℓ for (b_1) $3n$ decay at E^*_{CN}=35.3 MeV, and (b_2) $4n$ decay at E^*_{CN}=39.3 MeV.

3.3 Summary

The decay analysis of $^{296}116^*$ and $^{266}Rf^*$ compound nuclei suggest that out of Z=126, 120, 114 and N=184 magic candidates, Z=126 and N=184 is the best suited magic pair to analyze the neutron evaporation channels. Following this, the $2n$, $3n$ and $4n$ decay cross-sections for $^{48}Ca+^{249}Bk \rightarrow ^{297}117^*$ reaction are calculated by using the Dynamical cluster-decay model (DCM) with proton magic Z=126 and neutron magic N=184. The measured and/ or theoretical data of $^{297}117^*$ CN could not be fitted for spherical choice of decaying fragments. However, with the inclusion of deformations up to β_{2i} and optimum orientations (θ_i^{opt}), the available data on $2n$ and $3n$ decay cross-sections could be fitted quite nicely, but the $4n$ decay cross-section required us to invoke ^{4}He decay as the competing residue in this case, which need experimental verification. Also, a possible contribution of the, not yet observed, fusion-fission process is indicated.

Other interesting results are: (i) the angular momentum does not seem to influence the fragmentation path in this reaction, independent of $2n$, $3n$ or $4n$ decay channel; (ii) ℓ_{min} and ℓ_{max} are reported to be the least for the heaviest neutron decay channel, i.e., $4n$ cluster, followed by $3n$ and $2n$; (iii) The barrier lowering parameter (ΔV_B) is shown to be almost independent of the compound nucleus excitation energy, and is reported to be least for the higher angular momentum states and the heaviest neutron cluster. In addition to neutron evaporation, an effort is made to address the α-decay and heavy cluster emission in superheavy region. The results are discussed in chapter 4.

Bibliography

[1] K. Sandhu and M. K. Sharma, AIP Conf. Proc. **1524**, 123 (2013).

[2] K. Sandhu, M. K. Sharma, A. Kaur, and R. K. Gupta, Phys. Rev. C **90**, 034610 (2014).

[3] R. K. Gupta, Niyti, M. Manhas, and W. Greiner, J. Phys. G: Nucl. Part. Phys. **36**, 115105 (2009).

[4] K. Sandhu, M. K. Sharma, and R. K. Gupta, Phys. Rev. C **85**, 024604 (2012).

[5] R. Kumar, K. Sandhu, M. K. Sharma, and R. K. Gupta, Phys. Rev. C **87**, 054610 (2013).

[6] K. Sandhu and M. K. Sharma, Braz. J. Phys. **44**, 64 (2014).

[7] S. G. Nilsson, C. F. Tsang, A. Sobiczewski, Z. Szymanski, S. Wycech, C. Gustafson, I.-L. Lamm, P. Möller, and B. Nilsson, Nucl. Phys. A **131**, 1 (1969).

[8] Z. Patyk and A. Sobiczewski, Nucl. Phys. A **533**, 132 (1991).

[9] K. Rutz, M. Bender, T. Bürvenich, T. Schilling, P.-G. Reinhard, J. A. Maruhn, and W. Greiner, Phys. Rev. C **56**, 238 (1997); M. Bender, K. Rutz, P.-G. Reinhard, J. A. Maruhn, and W. Greiner, Phys. Rev. C **60**, 034304 (1999).

[10] A. T. Kruppa, M. Bender, W. Nazarewicz, P. -G. Reinhard, T. Vertse, and S. Cwiok, Phys. Rev. C **61**, 034313 (2000).

[11] Yu. Ts. Oganessian *et al.*, Phys. Rev. C **83**, 054315 (2011).

[12] V. Zagrebaev and W. Greiner, Phys. Rev. C **78**, 034610 (2008).

[13] C. Shen, Y. Abe, D. Boilley, G. Kosenko, and E. Zhao, Int. J. Mod. Phys. E **17**, 66 (2008).

[14] Z. H. Liu and J.-D. Bao, Phys. Rev. C **80**, 034601 (2009).

[15] S. Hofmann *et al.*, Eur. Phys. J. A **48**, 62 (2012).

[16] M. Murakami *et al.*, Phys. Rev. C **88**, 024618 (2013).

Chapter 4

Alpha(α)-decay and heavy particle radioactivity (HPR)

In the previous chapter, the magicity effects were addressed in context of SH region and the same were employed to investigate the neutron evaporation process. As an illustrative example, the role of deformations in the decay of $^{297}117^*$ compound nucleus formed in the ^{48}Ca+^{249}Bk reaction was explored using DCM [1]- [6]. The measured data could be fitted only with the inclusion of β_{2i}-deformed fragmentation approach, hence the deformation (β_{2i}-static) effects seem indispensable for $^{297}117^*$ nucleus. With the aim to explore such effects extensively, the $2n$, $3n$ and $4n$ evaporation channels of $^{291}115^*$ compound nucleus are investigated in the excitation energy range E^*_{CN}=31-47 MeV. A comparative analysis of spherical *vs* static and dynamic deformations is made explicitly for the $2n$-evaporation residue, as only $2n$ decay responds to spherical fragmentation approach. The higher neutron clusters such as $3n$ and $4n$ can only be fitted after the inclusion of deformation effects. Also unlike $^{297}117^*$, the suppression in the $4n$-cross-section is not observed for the decay of $^{291}115^*$ CN. Furthermore, the evaporation cross-sections of $2n$, $3n$ and $4n$-channels are also estimated at Bass barrier by interpolating the neck-length parameters

fixed in reference to available data at above barrier energies. This work is published in [5].

Subsequent to neutron evaporation, the ground state decays such as α-emission and heavy particle radioactivity (HPR) are also discussed in this chapter to understand the overall decaying scenario of superheavy nuclei. The excited state and ground state mechanisms are worked out respectively in the framework of Dynamical cluster decay model (DCM) [1]- [6] and Preformed cluster model (PCM) [7]- [10]. The α-decay chains of Z=115 isotopes and HPR observed for Z=113, 115 and 117 superheavy nuclei are addressed using "hot" optimum orientations of nuclei. In the study of the α-decay chains a constant empirical factor in penetrability is proposed, whereas the HPR is analyzed by employing different proximity potentials such as Prox-77 [11] and Prox-00 [12] to calculate the decay half lives.

The organization of the chapter is as follows: The introduction regarding excited and ground state decays is described in Sec. 4.1. The results of DCM based calculations for the decay of $^{291}115^{*}$ are discussed in Sec. 4.2. The α-decay and heavy particle radioactivity (HPR), studied in the framework of PCM are also discussed within the same section. Finally the results are summarized in Sec. 4.3.

4.1 Introduction

The advancement in the heavy ion reactions to explore the dynamics of superheavy mass region is mainly achieved through the hot fusion process, compared to reactions based on doubly magic ^{208}Pb and ^{209}Bi. Through this process, SHEs upto Z=118 have been synthesized by using various combinations of actinide targets (U, Pu, Am, Cm, Bk and Cf) and ^{48}Ca projectile [13, 14]. Recently, some experiments were performed using the fusion reaction of radioactive target nucleus ^{243}Am and the doubly magic ^{48}Ca beam [15], in order

to synthesize a chemical element with atomic number Z=115. Earlier in 2003 [16,17], the element Z=115 was observed for first time in the same reaction. The work presented in [15] is mainly based upon the production and decay properties of ^{289}115, ^{288}115 and ^{287}115 nuclei. Significant amount of data for $2n$, $3n$ and $4n$ decay channels is made available over a wide range of incident energies above the Bass barrier and the same is tested in the framework of DCM [1]- [6].

In addition to the channel cross-sections, the consecutive α-decay chains of Z=115 isotopes are also reported in [15], as α- emission gives an important information about the influence of nuclear structure on the decay properties of nuclei. It is to be noted that, due to their long lived decay chains, the synthesis of SHE with odd-Z give more detailed information than the even-Z nuclei. More specifically, the relatively high stability of α-decaying isotopes of element 115, against spontaneous fission, is associated with the strong influence of spherical nuclear shells at Z>82 and N>126, which require an appropriate theoretical interpretation. The Preformed cluster model (PCM) [7]- [10] is applied to understand the various α-decay chains of ^{287}115, ^{288}115 and ^{289}115 nuclei.

Apart from the basic α-decay mode of the superheavy mass region, Poenaru *et al.* [18] have also suggested another ground state decay phenomenon known as heavy particle radioactivity (HPR). Theoretically, it is mainly observed for the superheavy nuclei Z_{parent}>110 via spontaneous emission of heavy clusters ($Z_{cluster}$>28) with corresponding daughter nuclei around the doubly magic ^{208}Pb. With an aim to address the HPR within collective clusterization process in PCM [7]- [10], the cluster decay in the ground states of ^{278}113, $^{287-289}$115 and ^{293,294}117 isotopes is investigated, leading to doubly magic ^{208}Pb or its neighboring nuclei. These nuclei [15, 19, 20] have been observed in the evaporation channels produced in a cold fusion reaction using a beam of ^{70}Zn on ^{209}Bi target and hot fusion reactions induced by ^{48}Ca projectile with actinide targets ^{243}Am and ^{249}Bk,

respectively.

4.2 Calculations and Results

In the present work, first in Sec. 4.2.1 the DCM is applied to calculate the $2n$, $3n$ and $4n$ cross-sections of $^{291}115^{*}$ compound nucleus in reference to the experimental data [15]. In view of the earlier calculations of DCM [3, 4], the magic shell closures Z=126 and N=184 are used to understand the neutron evaporation channels of $^{291}115^{*}$ CN. The role of β_{2i} (static and dynamic) deformations is discussed for the production cross-sections of Z=115 isotopes. It is worth mentioning here that the comparison of β_{2i} (static) [21] and β_{2i} (dynamic) [22,23] is carried out by making static deformation $\beta_{2i}(0)$ temperature dependent, through the relation:

$$\beta_{2i}(T) = exp(-T/T_0)\beta_{2i}(0)$$

where T_0 is the temperature of the nucleus at which shell effects start to vanish, and is approximately taken as 1.5 MeV.

Sec. 4.2.2 is presented to depict the results of α-decay half lives of $^{287}115$, $^{288}115$ and $^{289}115$ nuclei using PCM, applied for spherical and deformed fragmentation approach. The application of the PCM is further tested in Sec. 4.2.3 to observe the heavy particle radioactivity (HPR) of the superheavy nuclei with Z=113, 115 and 117. It is relevant to mention that this work is carried out in continuation to the chapter 1 to understand the role of deformations in excited and ground state decay mechanisms in context of the chosen reactions.

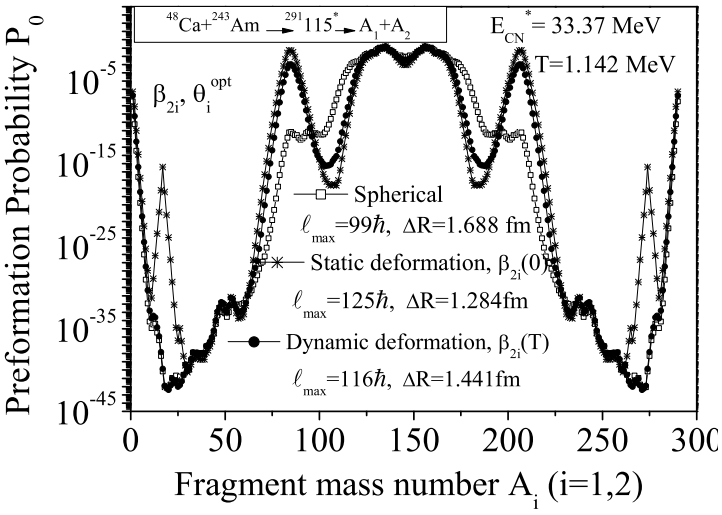

Figure 4.1 Preformation probability for the decay of $^{291}115^{*}$ compound system formed in the ^{48}Ca+^{243}Am reaction for spherical and deformed choices of fragments with optimum hot orientations ($\theta_i^{opt.}$) at E_{CN}^{*}=33.37 MeV and respective ℓ_{max}-values. The deformations are taken up to quadrupole (β_{2i}), with both the static and dynamic choices.

4.2.1 Neutron evaporation cross-sections of $^{291}115^{*}$ CN

Fig. 4.1 shows the preformation probability (P_0) in reference to $2n$-evaporation cross-section data at E_{CN}^{*}=33.37 MeV. In order to understand the role of deformations in the decay of the $^{291}115^{*}$ compound nucleus, Fig. 4.1 is plotted for the cases of spherical, β_{2i}-static and β_{2i}-dynamic choices of deformations. The preformation probability (P_0) is the probability with which the cluster or fragment is preformed before it comes out of the compound system by penetrating the potential barrier. It is a relative quantity, i.e., a slight change in the potential for any one of the fragments leads to redistribution of P_0 among all the fragments. The PES (equivalently the preformation path) for the spherical case indicates symmetric fission, where as the same for deformed choice gives asymmetric peaks in heavy mass fragment (HMF) region. The preformation probability remains almost identical for static and dynamic choices of deformations, except that, for the static case, higher ℓ_{max} and smaller neck-length parameter (ΔR) values are required for a best fit of the data. This happens because the temperatures involved are quite small (T=1.1-

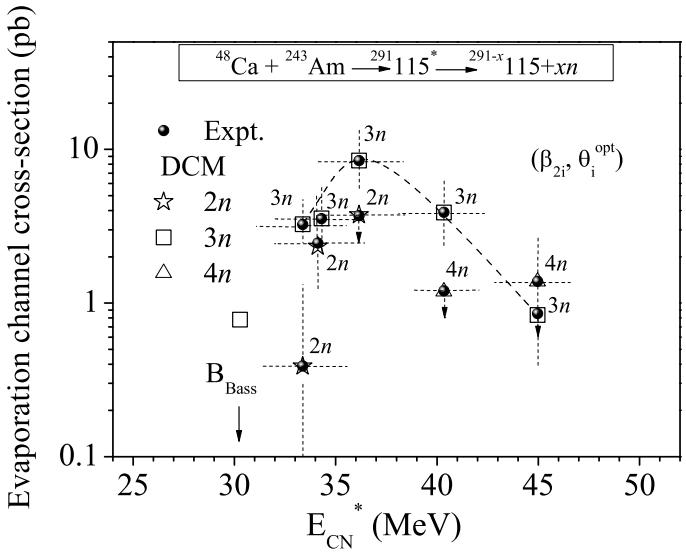

Figure 4.2 Calculated cross- sections for $2n$, $3n$ and $4n$ evaporation channels of the ^{48}Ca+^{243}Am reaction as a function of E^*_{CN}, compared with experimental data [15]. The error bars are also shown. The deformations are up to β_{2i}, along with optimum hot orientations. The Bass barrier [24] is also shown as a downward arrow. The dashed line is to guide the eye.

1.3 MeV), and hence further analysis is made in the context of static deformations only. It is relevant to mention here that spherical fragmentation works only for the $2n$ decay, and the $3n$ and $4n$ decay channels can be fitted only after the inclusion of deformation effects. In other words, the deformations of fragments play an extremely important role in the decay of the $^{291}115^*$ nuclear system.

Fig. 4.2 shows the comparison of the DCM calculated cross-sections for xn-evaporation channels of the ^{48}Ca+^{243}Am reaction with the experimental data [15]. A nice fitting of data is obtained for all the channels at different excitation energies. Note that all the measured evaporation residue cross-sections are above the Bass (B_{Bass}) barrier. For $3n$-evaporation channel, the cross-section is maximum at E^*_{CN}=36.15 MeV, and it is predicted to reduce systematically at the Bass energy. The calculated $3n$ cross-section at the B_{Bass} energy is obtained by interpolating the neck-length parameter (ΔR) by a second order polynomial

$$\Delta R = -6.66 \times 10^{-4} + 0.09506 E_{CN} - 0.0014 E^2_{CN},$$

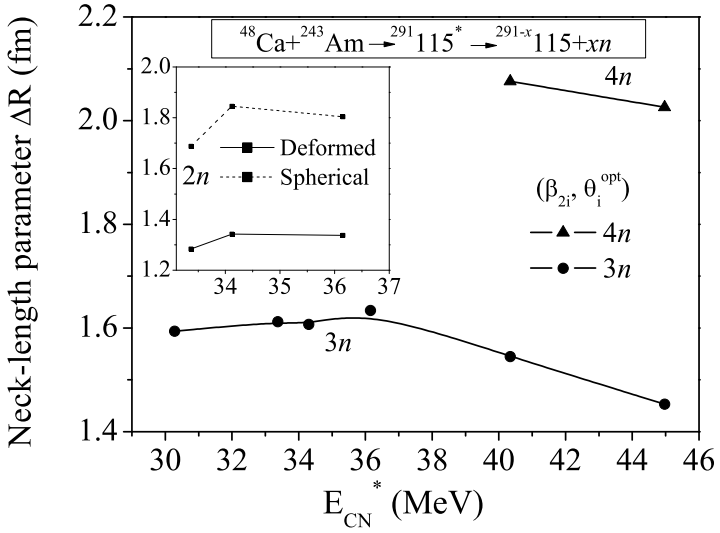

Figure 4.3 Variation of the neck-length parameter (ΔR) with E^*_{CN}, obtained for the best fit to neutron fusion-evaporation data [15] for the ^{48}Ca+^{243}Am reaction, using the DCM. The inset shows the comparison of neck-lengths of the $2n$ channel for spherical and deformed choices of nuclei.

obtained by fitting of the calculated points (see Fig. 4.3). The same procedure cannot be applied for the predictions of $2n$ and $4n$ channels because enough data points are not available for these channels. However, using the systematics of ΔR in Fig. 4.3, the $4n$ cross-section is obtained to be 0.0418 pb and the $2n$ cross-section is almost negligible at the Bass barrier energy. Fig. 4.3 shows the variation of neck-length parameter (ΔR) with excitation energy (E^*_{CN}). A comparison of neck-lengths for $2n$ channel is also shown in the inset of this figure for deformed and spherical choices of fragments. The neck-length comes out to be greater for spherical case than for the deformed one. For $2n$ and $3n$ channels, the variation of ΔR follows the same trend as that of the cross-section but for $4n$-channel, it becomes maximum, thereby indicating higher reaction time.

4.2.2 α-decay chains of ^{291}115*-xn using the PCM

The neutron evaporation decay of ^{291}115* compound nucleus results in the production of three isotopes of element 115, with mass numbers 287, 288, and 289. Various α-decay

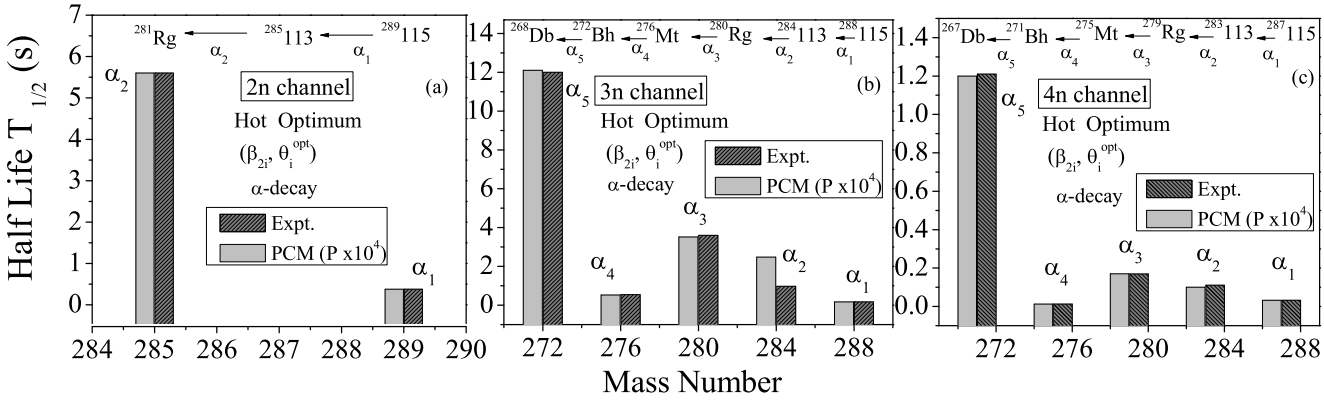

Figure 4.4 Comparison of experimental and PCM calculated half-lives of α-decay chains from (a) $2n$ (b) $3n$ and (c) $4n$-decay channels of $^{291}115^{*}$ formed in the ^{48}Ca+^{243}Am reaction. The hot optimum orientations are used with in the framework of the PCM.

chains are further detected from these isotopes, and the corresponding half-lives are measured. Fig. 4.4 shows the calculated half-lives of α-decay chains by using the Preformed cluster model (PCM), compared with experimental data [15]. It is clear from the figure that the calculations agree nicely with experiments within a constant empirical factor. In the calculations, deformations are included up to β_{2i}, with optimum "hot" orientations. This means that both preformation probability (P_0) and penetrability (P), involving fragmentation potential $V(\eta)$ and scattering potential $V(R)$, respectively, are calculated for use of "hot" optimum orientations of the ℓ=0 case, with the required assault frequency (ν_0) calculated by Eq.(2.43) of chapter 2. The half-lives ($T_{1/2}$), preformation probability (P_0), penetrability (P), impinging (assault) frequency (ν_0), neck-length parameter (ΔR), and Q_{out} values for the α-decay chains from $2n$, $3n$ and $4n$ decays of $^{291}115^{*}$ formed in the ^{48}Ca+^{243}Am are also presented in Table 4.1. For a best fit to data, the penetrability P is normalized by a constant factor of 10^4 for all the three n-channels, which accounts for either the de-excitation probability W_i, taken as one (same as for heavy clusters) or the change in penetrability contributions P_i and P_b (see Fig. 2.3 of chapter 2). In the present α-decay process, the subsequent daughters are not in the ground state and hence

Table 4.1 The experimental and PCM calculated half-lives ($T_{1/2}$), together with the corresponding preformation probability (P_0), penetrability (P), impinging frequency (ν_0), neck-length parameter (ΔR), and Q-values ($Q_{out.}$) [21] for the α-decay chains after $2n$, $3n$ and $4n$ decays of $^{291}115^*$ formed in the ^{48}Ca+^{243}Am reaction.

α-decay	P_0	P($\times10^4$)	ν_0	ΔR	$Q_{out.}$	$T_{1/2}^{PCM}$	$T_{1/2}^{Expt.}$
			$2n$-channel				
$^{289}115 \rightarrow ^{285}113$	1.22×10^{-10}	5.28×10^{-12}	2.811×10^{21}	1.796	10.026	0.38	$0.38^{+0.18}_{-0.10}$
$^{285}113 \rightarrow ^{281}$Rg	1.80×10^{-10}	2.56×10^{-13}	2.673×10^{21}	1.217	8.976	5.60	$5.60^{+2.2}_{-1.2}$
			$3n$-channel				
$^{288}115 \rightarrow ^{284}113$	1.85×10^{-10}	7.75×10^{-12}	2.828×10^{21}	1.846	10.126	0.17	$0.17^{+0.042}_{-0.028}$
$^{284}113 \rightarrow ^{280}$Rg	1.02×10^{-10}	1.01×10^{-12}	2.701×10^{21}	0.900	9.146	2.48	$0.97^{+0.25}_{-0.17}$
^{280}Rg $\rightarrow ^{276}$Mt	1.43×10^{-12}	4.82×10^{-11}	2.858×10^{21}	1.867	10.136	3.52	$3.60^{+0.9}_{-0.6}$
^{276}Mt $\rightarrow ^{272}$Bh	4.64×10^{-12}	1.01×10^{-10}	2.843×10^{21}	1.615	9.926	0.52	$0.54^{+0.14}_{-0.09}$
^{272}Bh $\rightarrow ^{268}$Db	2.06×10^{-11}	1.03×10^{-12}	2.704×10^{21}	1.498	8.886	12.10	$12.0^{+3.1}_{-2.1}$
			$4n$-channel				
$^{287}115 \rightarrow ^{283}113$	2.76×10^{-10}	2.69×10^{-11}	2.848×10^{21}	1.670	10.246	0.0326	$0.032^{+0.058}_{-0.013}$
$^{283}113 \rightarrow ^{279}$Rg	7.39×10^{-10}	3.08×10^{-12}	2.735×10^{21}	1.075	9.356	0.111	$0.1^{+0.49}_{-0.045}$
^{279}Rg$\rightarrow ^{275}$Mt	1.77×10^{-13}	7.75×10^{-9}	2.971×10^{21}	1.540	10.926	0.1695	$0.17^{+0.81}_{-0.08}$
^{275}Mt$\rightarrow ^{271}$Bh	2.92×10^{-11}	6.70×10^{-10}	2.866×10^{21}	1.320	10.066	0.0123	$0.012^{+0.023}_{-0.005}$
^{271}Bh$\rightarrow ^{267}$Db	1.97×10^{-10}	1.09×10^{-12}	2.672×10^{21}	1.134	8.656	1.21	$1.2^{+5.9}_{-0.5}$

"hot" process is preferred over "cold" one, which means that the Q_{out} value gets modified due to vibrational and excitation energy, which in turn changes the magnitude of penetrability (P). The same factor in the penetration probability (P) is required when the spherical fragmentation approach is applied to study the α-decay chains of Z=115 isotopes, as discussed in [6].

4.2.3 Heavy particle radioactivity of Z=113, 115 and 117 superheavy isotopes

The analysis of cluster decay calculations, considered with atomic number $2<Z_{cluster}\leq20$ within the PCM, is extended to heavier clusters in superheavy region with $Z_{cluster}^{max}$ = Z_{parent}-82, to learn about the most probable cluster emitted across doubly magic daugh-

ter ^{208}Pb, or nearby stable nucleus. The effects of deformations are considered up to quadrupole (β_{2i}) in reference to optimum orientation criteria as suggested in [1]. Different versions of proximity potentials are employed in this work to study the heavy particle radioactivity (HPR) of ^{278}113 [19], $^{287-289}$115 [15] and ^{293,294}117 [20] systems. This work is published in [10].

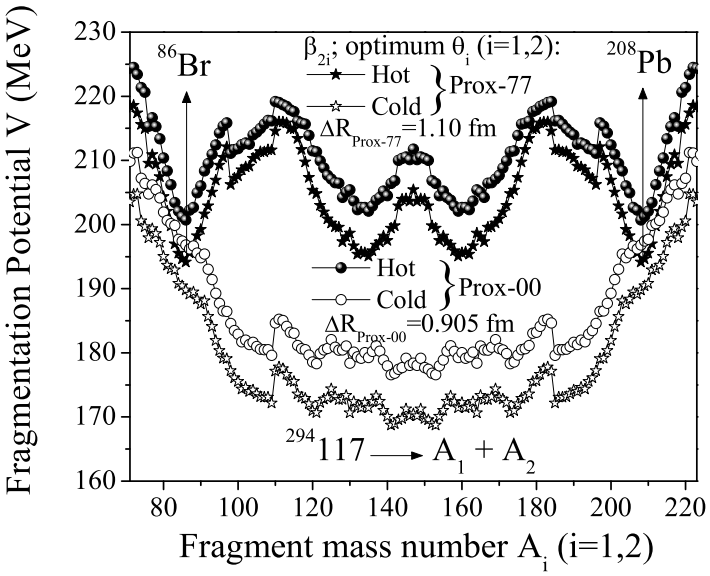

Figure 4.5 Fragmentation potential for the parent nucleus ^{294}117 using proximity potentials Prox-77 and Prox-00 for β_{2i} deformed choice of nuclei with optimum (θ_i^{opt}) orientations forming hot compact (filled symbols) and cold elongated (open symbols) configuration, taking into account all possible fragments.

First of all, one may look at the behavior of fragmentation potentials, illustrated in Fig. 4.5, for the parent nucleus ^{294}117, calculated for the fragments with quadrupole deformations (β_{2i}) and optimum orientations (θ_i^{opt}). The role of 'hot compact' and 'cold elongated' configurations of orientations are also worked out in this figure. Note that the orientations are uniquely fixed (optimized) on the basis of the signs of β_{2i} alone which manifests in the form of 'hot compact' and 'cold elongated' configuration [1]. The calculations are done using nuclear proximities Prox-77 [11] and Prox-00 [12] at fixed value of internuclear separation distances. Despite the use of different nuclear proximity potentials, our anal-

ysis of Fig. 4.5 clearly shows that ^{86}Br is the most probable cluster (showing strongest minimum in potential energy surface) with corresponding ^{208}Pb daughter for the choice of 'hot' in comparison to 'cold' configuration. In other words, the region for heavy particle radioactivity is more favorable, and hence show a clear preference in the fragmentation potential, for 'hot compact' in comparison to 'cold elongated' configuration.

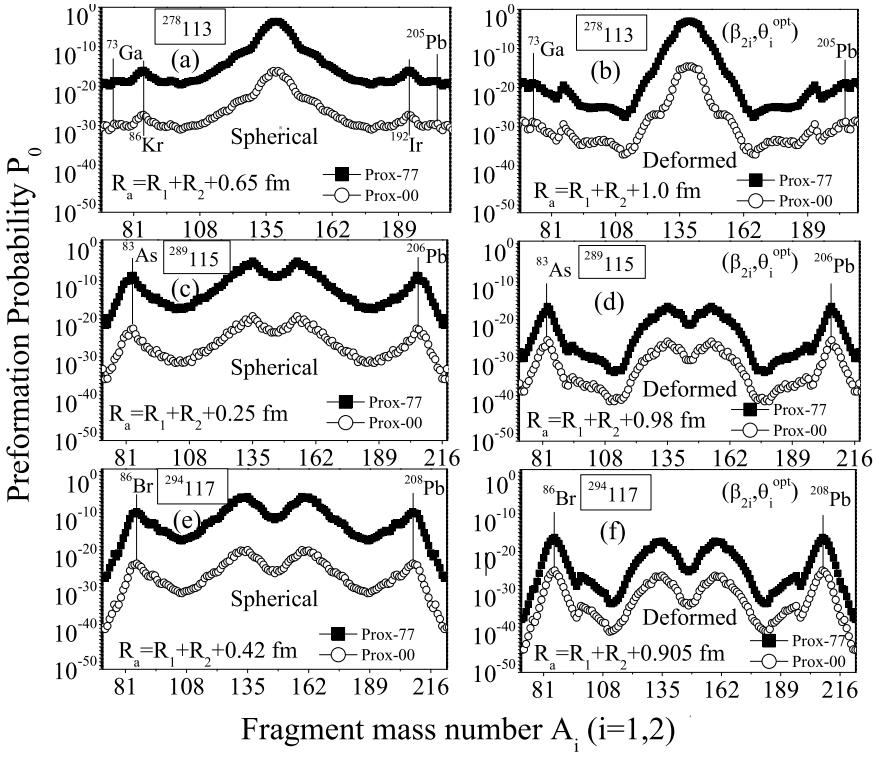

Figure 4.6 Preformation probability (P_0) for the decay of ^{278}113, ^{289}115 and ^{294}117 nuclei using nuclear potentials Prox-77 and Prox-00 for spherical [panels (a), (c), and (e)] and deformed [panels (b), (d) and (f)] choices of nuclei. The most probable cluster corresponding to Pb daughter is pointed out with solid lines.

Fig. 4.6 presents the calculated preformation probability (P_0) as a function of fragment mass number (A_i, i=1, 2) for the parent nuclei ^{278}113, ^{289}115, and ^{294}117 using both the proximity potentials. The specific role of deformations is studied in this figure, where the calculations have been done using spherical consideration as well as for β_{2i}-deformed choice of fragments. In order to look for the exclusive role of interaction potentials, the

calculations have been made at the same neck length parameter (ΔR), chosen in reference to Prox- 00 and is clearly depicted in Fig. 4.6 for ^{278}113, ^{289}115, and ^{294}117 nuclei. It is evident from Fig. 4.6 that the inclusion of deformation and orientation effects of the decay fragments change the potential energy surface (PES) which in turn affects the decay constant and half life time accordingly. A solid vertical line is drawn in order to point out the most probable ^{73}Ga, ^{83}As and ^{86}Br clusters and their respective ^{205}Pb, ^{206}Pb and ^{208}Pb daughters emitted from ^{278}113, ^{289}115 and ^{294}117 parent nuclei. Interestingly, the emergence of ^{86}Kr cluster and its complement ^{192}Ir seems to be more prominent in the fragmentation of ^{278}113, irrespective of spherical or deformed configuration [see Fig. 4.6 (a) and 4.6 (b)]. However, if one refers only to Pb radioactivity, then ^{73}Ga may be considered as the most preferred cluster. Hence three important results can be extracted from Fig. 4.6: (i) Except for the change in the magnitude, no noticeable change in the structure of PES is observed while going from Prox-77 to Prox- 00 with spherical as well as deformed fragments; (ii) the status of the preferred cluster remains intact, independent of the choice of nuclear proximity potential and deformation used; (iii) the favorable clusters shift toward the heavier mass region with the increase in mass number of parent nuclei.

It is to be noted that PCM based calculations are sensitive to the choice of neck-length parameter (ΔR) which in turn, plays an important role in the estimation of decay half-life. Therefore, an attempt have been made in Fig. 4.7 to predict a range of cluster decay half-lives for the considered parents with effects of deformations and orientations included. Also shown in this figure are the predictions of Poenaru *et al.* [18] based on analytical super-asymmetric fission model (ASAFM), obtained by using different (AME11 [25], LiMaZe01 [26, 27] and KTUY05 [28]) mass tables. From Fig. 4.7, one may observe that half-life time is influenced by the variation in ΔR; the only parameter of the model which decides the entry point of barrier penetration as well as of the clusters preformation.

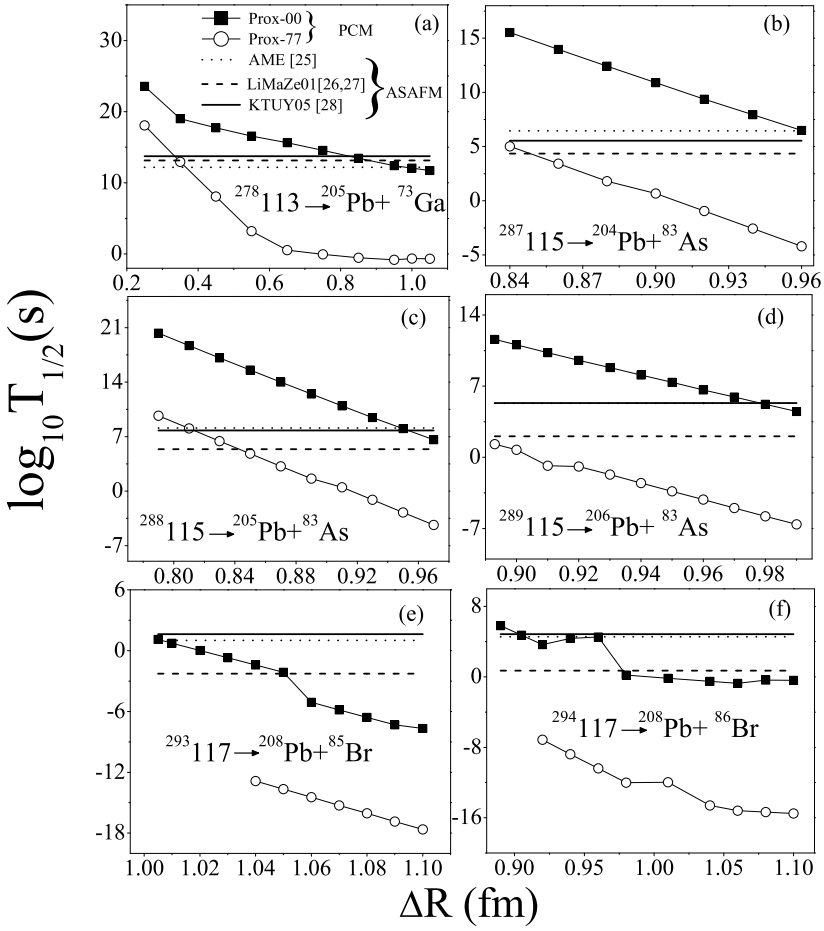

Figure 4.7 PCM predicted decay half-lives for the most probable cluster emitted from $^{278}113$, $^{287-289}115$ and $^{293,294}117$ isotopes over a range of neck-length parameter (ΔR) for the use of β_{2i}-deformed decay products.

At a given ΔR value, $\log_{10}T_{1/2}$ is relatively larger for the choice of Prox-00 in comparison to Prox-77. Apart from providing nice agreement with the results of ASAFM, the PCM predicted half-lives over a wide range of neck values, which may provide a testing ground for the future experiments on cluster decay studies.

Finally, the possible role of shell corrections is investigated for understanding the cluster dynamics in the SHE region, taking $^{289}115 \longrightarrow A_1 + A_2$ as an example, with deformations upto β_{2i} and for the case of Prox-00 only. Fig. 4.8 (a) is plotted to check dependance of P_0 on shell corrections, by taking δU=0 and compare it with the case of δU$\neq$0. Fig. 4.8 (a) clearly shows that the maximum yield (P_0) is obtained for ^{83}As fragment, and

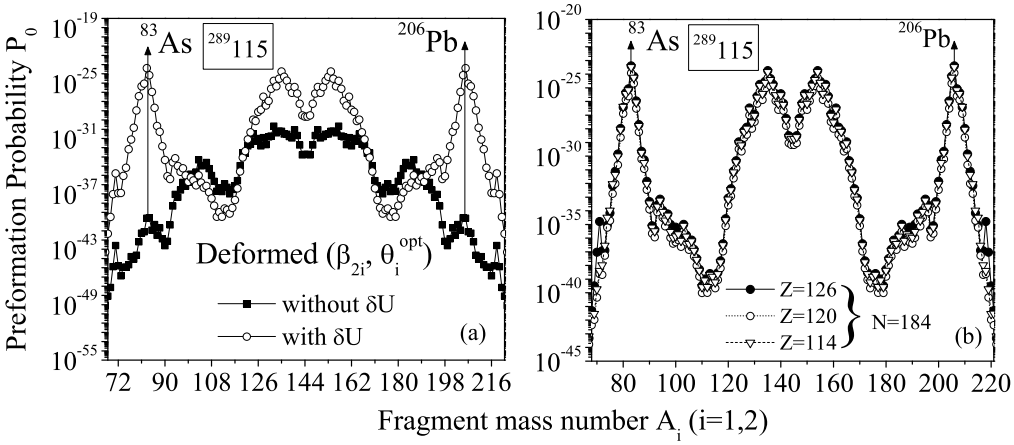

Figure 4.8 (a) Role of shell corrections δU, illustrated for ^{289}115 by plotting the preformation factor (P_0) as a function of both the cluster and daughter masses, using Z=126 and N=184. (b) The same as (a), plotted by considering the different magic shell closures Z=126, 120, 114 and N=184 for the use of Prox-00. ΔR=0.98 fm, having kept the same in all the three cases for comparison.

its complementary heavy residue ^{206}Pb, only when the shell corrections δU are added to the liquid drop part of the binding energy term. The above observation clearly suggests that shell corrections play an important role and hence are essential to make concrete and explicit predictions of the clusterization process in SHE region. In order to investigate the role of different superheavy magic shell closures, the variation of P_0 is shown in Fig. 4.8 (b) for all the three choices of magic pairs i.e. Z=114, 120, 126 and N=184, within the deformed fragmentation approach. The shell corrections for the above magic numbers are calculated by using the empirical formula [29] and accordingly the liquid drop energies are calculated [3, 4] to give the experimental binding energies. The comparative analysis with different superheavy magic pairs is carried out at the same neck length parameter (ΔR) of Z=126 and N=184. Apparently, the emergence of heavy cluster ^{83}As and the corresponding ^{206}Pb daughter is found equally favored, i.e., nearly indistinguishable for the three magic pairs of Z, N which in turn, seem to suggest that HPR emission does not depend on the choice of proton magicity in SHE region.

4.3 Summary

The xn-decay cross-sections of $^{291}115^*$ CN formed in the ^{48}Ca+^{243}Am reaction is studied by using the Dynamical cluster-decay model (DCM) at excitation energies E^*_{CN}=31-47 MeV. The effects of static and dynamic deformations up to β_{2i} are studied on the fragmentation process of xn evaporation channels. It is shown that the spherical case of fragments prefer symmetric fission, where as the same for deformed choice give asymmetric peaks in heavy fragment mass region. Only the 2n-cross-sections could be fitted with the spherical choice of fragments, but the same did not work for 3n and 4n channels. In other words, deformations play a significant role in understanding the dynamics involved in the decay of $^{291}115^*$ compound nucleus. The xn evaporation cross-sections are also predicted at Bass barrier, which could be of interest for the future experiments.

The α-decay chains from the three isotopes of element 115 with masses 287, 288, and 289 are investigated by using the Preformed cluster model (PCM), with effect of deformation and "hot" optimum orientation included. A nice fitting of the experimentally observed half-lives are obtained with in a constant scaling factor in penetration probability (P). An interesting result of this calculation is that half-lives of α-decay chains prefer "hot" optimum orientations within the PCM, rather than the usual "cold" optimum orientations for spontaneous α-decays. Also the heavy particle radioactivity (HPR) follows same orientation approach i.e. "hot-optimum" within the collective clusterization process. For HPR, the effect of different nuclear proximity potentials on cluster decay half-lives ($T_{1/2}$) and preformation probability (P_0), along with the possible role of magic shells are investigated in order to extract a clear picture of the dynamics involved. The calculations are further shown to be extremely sensitive to the choice of neck-length parameter (ΔR) and hence an effort is made to predict a range of $T_{1/2}$ values which could possibly provide new directions for cluster decay measurements.

After making an extensive effort to address the role of static and dynamic deformations in the excited state and ground state decay mechanisms of superheavy nuclei in chapters 3 and 4. It is of further interest to investigate the relevance of orientation degree of freedom in the dynamics of heavy ion induced reaction pertaining to superheavy region. These results are discussed in chapter 5.

Bibliography

[1] R. K. Gupta, M. Balasubramaniam, R. Kumar, N. Singh, M. Manhas, and W. Greiner, J. Phys. G: Nucl. Part. Phys. **31**, 631 (2005).

[2] B. B. Singh, M. K. Sharma, and R. K. Gupta, Phys. Rev. C **77**, 054613 (2008).

[3] R. K. Gupta, Niyti, M. Manhas, and W. Greiner, J. Phys. G: Nucl. Part. Phys. **36**, 115105 (2009).

[4] K. Sandhu and M. K. Sharma, AIP Conf. Proc. **1524**, 123 (2013); K. Sandhu, M. K. Sharma, A. Kaur, and R. K. Gupta, Phys. Rev. C **90**, 034610 (2014).

[5] R. Kumar, K. Sandhu, M. K. Sharma, and R. K. Gupta, Phys. Rev. C **87**, 054610 (2013).

[6] R. Kumar, M. K. Sharma, K. Sandhu, and R. K. Gupta, EPJ Web of Conferences **66**, 03050 (2014).

[7] S. S. Malik and R. K. Gupta, Phys. Rev. C **39**, 1992 (1989).

[8] G. Sawhney, M. K. Sharma, and R. K. Gupta, Phys. Rev. C **83**, 064610 (2011).

[9] R. Kumar and M. K. Sharma, Phys. Rev. C **85**, 054612 (2012).

[10] G. Sawhney, K. Sandhu, M. K. Sharma, and R. K. Gupta, Eur. Phys. J. A **50**, 175 (2014).

[11] J. Blocki, J. Randrup, W. J. Swiatecki, and C. F. Tsang, Ann. Phys. (NY) **105**, 427 (1977).

[12] W. D. Myers and W. J. Swiatecki, Phys. Rev. C **62**, 044610 (2000).

[13] S. Hofmann and G. Münzenberg, Rev. Mod. Phys. **72**, 733 (2000).

[14] Yu. Ts. Oganessian, J. Phys. G: Nucl. Part. Phys. **34**, R165 (2007).

[15] Yu. Ts. Oganessian *et al.*, Phys. Rev. Lett. **108**, 022502 (2012); Phys. Rev. C **87**, 014302 (2013).

[16] Yu. Ts. Oganessian *et al.*, Phys. Rev. C **69**, 021601(R) (2004).

[17] Yu. Ts. Oganessian *et al.*, Phys. Rev. C **72**, 034611 (2005).

[18] D. N. Poenaru, R. A. Gherghescu, and W. Greiner, Phys. Rev. Lett. **107**, 062503 (2011); D. N. Poenaru, R. A. Gherghescu, and W. Greiner, Phys. Rev. C **85**, 034615 (2012).

[19] K. Morita *et al.*, J. Phys. Soc. Jpn. **81**, 103201 (2012).

[20] Yu. Ts. Oganessian *et al.*, Phys. Rev. C **83**, 054315 (2011).

[21] P. Möller, J. R. Nix, W. D. Myers, and W. J. Swiatecki, At. Data Nucl. Data Tables **59**, 185 (1995).

[22] M. Muenchow and W. Scheid, Phys. Lett. B **162**, 265 (1985); Nucl. Phys. A **468**, 59 (1987).

[23] M. Rashdan, A. Faessler, and W. Wadia, J. Phys. G: Nucl. Part. Phys. **17**, 1401 (1991).

[24] R. Bass, in *Proceedings of the Symposium on Deep Inelastic and Fusion Reactions with Heavy Ions*, Lecture Notes in Physics, Vol. **117**, edited by W. von Oertzen, (Springer-Verlag, Berlin), p.281 (1980).

[25] G. Audi and W. Meng (private communication, quoted in Ref. [18]).

[26] S. Liran, A. Marinov, and N. Zeldes, Phys. Rev. C **62**, 047301 (2000).

[27] S. Liran, A. Marinov, and N. Zeldes, Phys. Rev. C **66**, 024303 (2002).

[28] H. Koura, T. Tachibana, M. Uno, and M. Yamada, Prog. Theor. Phys. **113**, 305 (2005).

[29] W. Myers and W. J. Swiatecki, Nucl. Phys. **81**, 1 (1966).

Chapter 5

Orientation effects across the Coulomb barrier

In addition to the deformations of nuclei, the role of orientation degree of freedom is also essential for overall understanding of superheavy reactions. Keeping this in mind, the dynamics of ^{30}Si+^{238}U$\rightarrow^{268}$Sg* reaction is studied using hot and cold 'optimum' orientations [1]. In the previous chapter, the orientation effects were investigated for the ground state emission such as α-decay and heavy particle radioactivity (HPR). The same are applied here to calculate the neutron evaporation residue and fission cross-sections of ^{268}Sg* nucleus in reference to the available data [2] by including β_{2i}-deformations. The calculations at above barrier energies are performed by considering the hot equatorial configuration, for which symmetric distribution of fragments can be seen. On the other hand, asymmetric fragmentation is observed at below/or sub barrier energies for cold polar configuration. In addition to this, at highest energy ($E_{c.m.}$=169 MeV), the comparison of spherical, β_{2i}-static and dynamic deformed fragmentation is carried out to understand the effect of temperature independent and dependent deformations on the decay mass fragments. This work is published in [3].

In the following, a brief introduction regarding the present work is reported in Sec. 5.1. The hot versus cold configuration results are discussed in Sec. 5.2 and the same are summarized in Sec. 5.3.

5.1 Introduction

The use of actinide target induced reactions for the superheavy synthesis is immensely desirable as it provides an opportunity to explore the reaction dynamics across the Coulomb barrier. Due to prolate nature of actinide targets, the collision probability of projectile towards an equatorial orientation of the deformed (target) nucleus is significantly enhanced. Hence the most compact starting configuration gets developed on way to the compound nucleus formation and/or subsequent decay [1]- [4]. This process is more viable at energies higher than the Coulomb barrier. Therefore the actinide targets achieve the maximum neutron excess in such configurations, and consequently result in higher fusion probability. The situation changes drastically when the energy is reduced to the sub-barrier region. The cross-sections drop rapidly in this region as the interactions are limited along the polar axis where the re-separation of the reaction partners is relatively large (elongated configuration) [1]- [4]. Hence, it seems reasonable that the former configuration would more likely result in fusion-fission, and the later in quasi-fission.

In view of all above, the main aim of this work is to investigate the role of deformations and orientations affecting the dynamics of ^{30}Si+^{238}U$\rightarrow^{268}$Sg* reaction. In addition to deformations, the motivation behind the exploration of orientation degree of freedom is to observe the drastically changed potential energy surfaces (PES) from asymmetric to symmetric mass distribution, at below and above the Coulomb barrier, respectively. It is important to mention that in DCM based calculations, the optimum orientations are fixed

for cold polar (elongated) and hot equatorial (compact) configurations [1], respectively, for the configurations corresponding to largest interaction radius with lowest barrier and smallest interaction radius with highest barrier

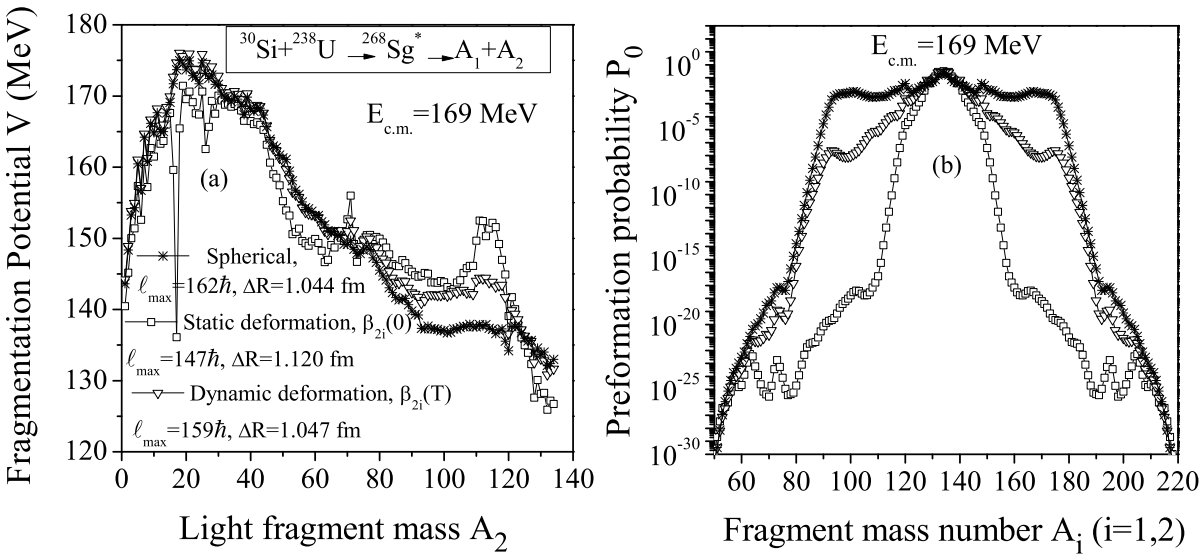

Figure 5.1 (a) Fragmentation potential for the ^{30}Si+^{238}U→^{268}Sg* reaction as a function of light fragment mass for spherical, β_{2i} -static and dynamic deformations with "optimum" orientations (θ_i^{opt}) at ℓ_{max} values. (b) Same as that of (a) but plotted for the preformation probability.

5.2 Calculations and Results

The decay of compound nucleus ^{268}Sg* in DCM [3]- [8] has been studied over a wide range of center-of-mass energies $E_{c.m.}$=125-169 MeV across the barrier, where both neutron evaporation channels ($3n$, $4n$ and $5n$) and fission cross-sections are measured [2]. The calculations are performed by considering the static β_{2i}-deformations within the 'optimum' orientation approach. In the present analysis, first to understand the deformation effects on the potential energy surfaces (PES) of the decay fragments, the fragmentation potential $V(A_2)$, shown in Fig. 5.1 (a), is plotted at the highest value of center-of-mass energy $E_{c.m.}$=169 MeV and at $\ell = \ell_{max}$ for spherical, β_{2i}-static and dynamic deformed

configurations. It can be seen from Fig. 5.1 (a) that the fragment mass distribution remains nearly identical for light particles (LPs) and intermediate mass fragments (IMFs) for all three cases. However, significant difference in the PES for the fission region is observed with the inclusion of β_{2i}-static/dynamic deformations. A strong variation can be seen in the decay path of β_{2i}-static choice of fragmentation, which otherwise remains relatively smooth for the spherical fragmentation approach. The β_{2i}-dynamic deformations exhibit an intermediate structural behavior. The occurrence of prominent minima in Fig. 5.1 (a) at A_2 =17 may be due to the inappropriate values of optimized β_{2i}- deformations used in the calculations and occur mainly because of the proximity (V_P) part of the fragmentation potential.

A similar trend can be seen in Fig. 5.1 (b) where the preformation probability (P_0) is plotted as a function of fragment mass by considering the nuclei as spherical, β_{2i}-static and β_{2i}-dynamic deformed. It is relevant to mention here that the maximum preformation probability (P_0) corresponds to minima in the fragmentation potential. Hence, Fig. 5.1 (b) clearly shows the emergence of differences for the same mass region $70 \leq A_2 \leq 130$, similar to one observed in the case of fragmentation plot (Fig. 5.1 (a)). Another point of difference between spherical and deformed choices of fragmentations lies in the fact that for spherical choice, the dominant fragments required for calculating the fission cross-sections are lying in the mass range $(A/2) \pm 42$, while a comparatively lesser number of fragments are contributing toward fission cross-sections with inclusion of deformation effects (β_{2i}-static and β_{2i}-dynamic). The dominant fission fragments for dynamic deformations are $(A/2) \pm 14$ which further reduces to $(A/2) \pm 9$ for static deformations. Hence, the huge difference in the fission fragmentation can be seen in going from spherical to β_{2i}-static deformed choice of fragmentation. Evidently, the β_{2i}-dynamic distribution lies in between that of spherical and β_{2i}-static cases of fragmentation.

Table 5.1 Experimental and DCM calculated evaporation residue cross-sections (σ_{xn}, x= 3, 4 and 5) of ^{268}Sg* CN, fitted for hot equatorial configuration.

$E_{c.m.}$(MeV)	xn	T (MeV)	ℓ_{max} ($\hbar$)	ΔR (fm)	σ_{xn}^{DCM}(pb)	$\sigma_{xn}^{Expt.}$(pb)
128	3n	1.207	120	1.536	14.7	15 upper limit
133	4n	1.291	113	1.850	10.2	$10 \pm^{10}_{6}$
144	5n	1.458	107	2.235	66.2	$67\pm^{67}_{37}$

Table 5.2 Experimental and DCM calculated fission cross-sections ($\sigma_{fission}$) in the decay of ^{268}Sg* formed in the ^{30}Si+^{238}U reaction by considering hot equatorial configuration.

$E_{c.m.}$(MeV)	T (MeV)	ℓ_{max} ($\hbar$)	ΔR (fm)	$\sigma_{fission}^{DCM}$(mb)	$\sigma_{fission}^{Expt.}$(mb)
169	1.778	147	1.120	792	792
159	1.658	142	1.076	594	597
154	1.594	139	1.058	382	390
149	1.528	136	1.049	268	269
144	1.458	134	1.029	156	156.5
139	1.385	133	0.997	65.6	65.9
134	1.307	131	0.964	19.8	20.0
129	1.225	128	0.944	3.18	3.25
125	1.154	126	0.905	0.129	0.123

Finally by using static-deformations upto β_{2i} with hot compact equatorial configuration, the fission and evaporation residue cross-sections are calculated at above and below barrier energies in the framework of DCM. Fig. 5.2 (a), alongwith tabulated results of Tables 5.1 and 5.2, clearly show a nice comparison of experimental and DCM fitted cross-sections. The disagreement at lowest incident energy for the use of cold polar configuration, shown in Fig. 5.2(b), is discussed in subsequent discussion.

Next, the role of equatorial and polar orientations (hot and cold configurations) is also worked out in the framework of DCM. Actually, the orientation degree of freedom plays extremely important role since polar, non-compact and equatorial, compact configurations are obtained, respectively, corresponding to largest interaction radius with lowest interaction barrier and the smallest interaction radius with highest interaction barrier.

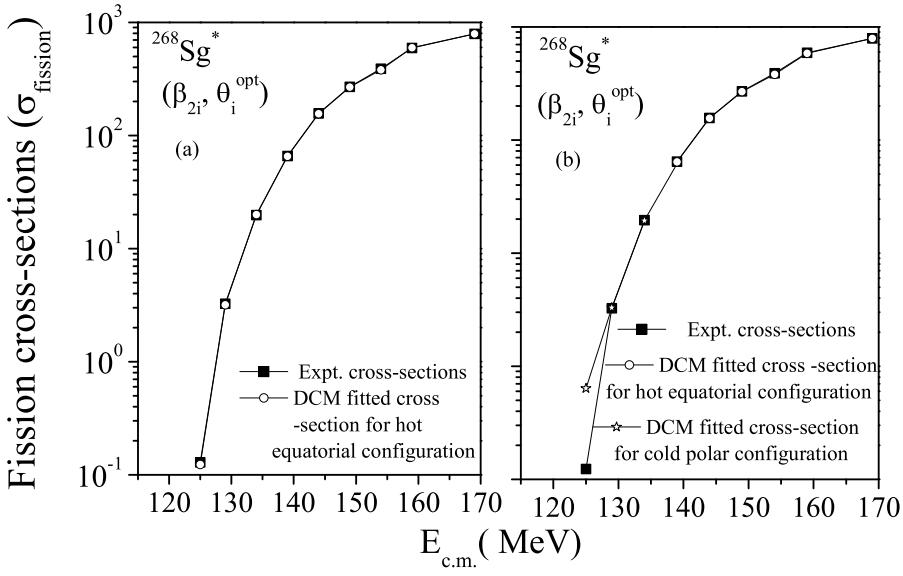

Figure 5.2 DCM calculated fission cross-sections for the decay of ^{268}Sg* (in hot equatorial and cold polar configurations), plotted as the function of $E_{c.m.}$, compared with the experimental data of Ref. [2].

Table 5.3 Experimental and DCM calculated fission cross-sections ($\sigma_{fission}$) in the decay of ^{268}Sg* formed in the ^{30}Si+^{238}U reaction by considering cold polar configuration.

$E_{c.m.}$(MeV)	T (MeV)	ℓ_{max} ($\hbar$)	ΔR (fm)	$\sigma_{fission}^{DCM}$(mb)	$\sigma_{fission}^{Expt.}$(mb)
134	1.307	144	0.524	19.5	20.0
129	1.225	133	0.345	3.30	3.25
125	1.154	130	0.000	0.638	0.123

Following this prescription, further calculations at sub-barrier energies with $E_{c.m.}$=125 to 134 MeV are done by considering polar configuration. From Fig. 5.2 (b) and Table 5.3, one may observe that for polar interactions, the DCM based cross-section at lowest energy is overestimated with respect to the experimental data. It might be due to the fact that with polar configuration the barrier height decreases and hence cross-section is overestimated. In order to see the comparative effect of equatorial and polar orientations on the nuclear dynamics, Fig. 5.3 is plotted in which the variation of the fragmentation potential as a function of light fragment mass is shown. This figure clearly shows a significant difference in the fragmentation paths of hot compact configuration and cold non-compact

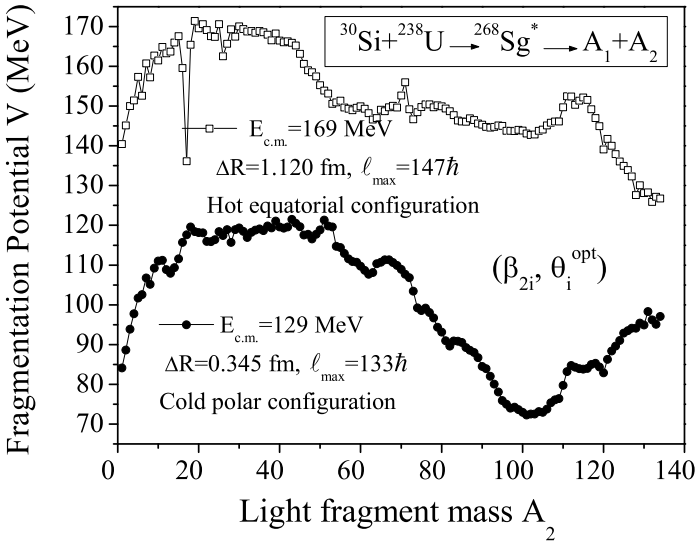

Figure 5.3 Variation of fragmentation potential V (MeV) as a function of light fragment mass (A_2) for the decay of $^{268}Sg^{*}$ CN, using hot-compact and cold non-compact configurations.

configuration, respectively, at 169 MeV and 129 MeV. No change in light particle (LP) region is observed, whereas a significant change in the fragmentation behavior for heavy mass fragments (HMFs) and fission fragments can be seen which is clarified further in Fig. 5.4, where detailed description of potential energy surfaces (PES) is represented. The fission mass distribution is plotted in Fig. 5.4, which shows the modified behavior of the potential energy surfaces (PES) at sub-barrier energies ($E_{c.m.}$=134, 129, and 125 MeV). The preformation probability remains symmetric for above barrier energies, represented in Figs. 5.4(a)- 5.4(f) with $E_{c.m.} > 134$ MeV, where equatorial configuration is taken into account. It becomes dominantly asymmetric when equatorial configuration is substituted by polar configuration at sub-barrier energies shown in Figs. 5.4(g)- 5.4(i). It is relevant to mention here that the asymmetric peaks are not due to any magic shell closures, it may arise due to some competing process like the quasi-fission at near or below barrier energies.

The above observations may be associated with results of Fig. 5.2 (b) and Table 5.3, where enhancement in the fission cross-section at deep sub-barrier energy $E_{c.m.}$=125 MeV

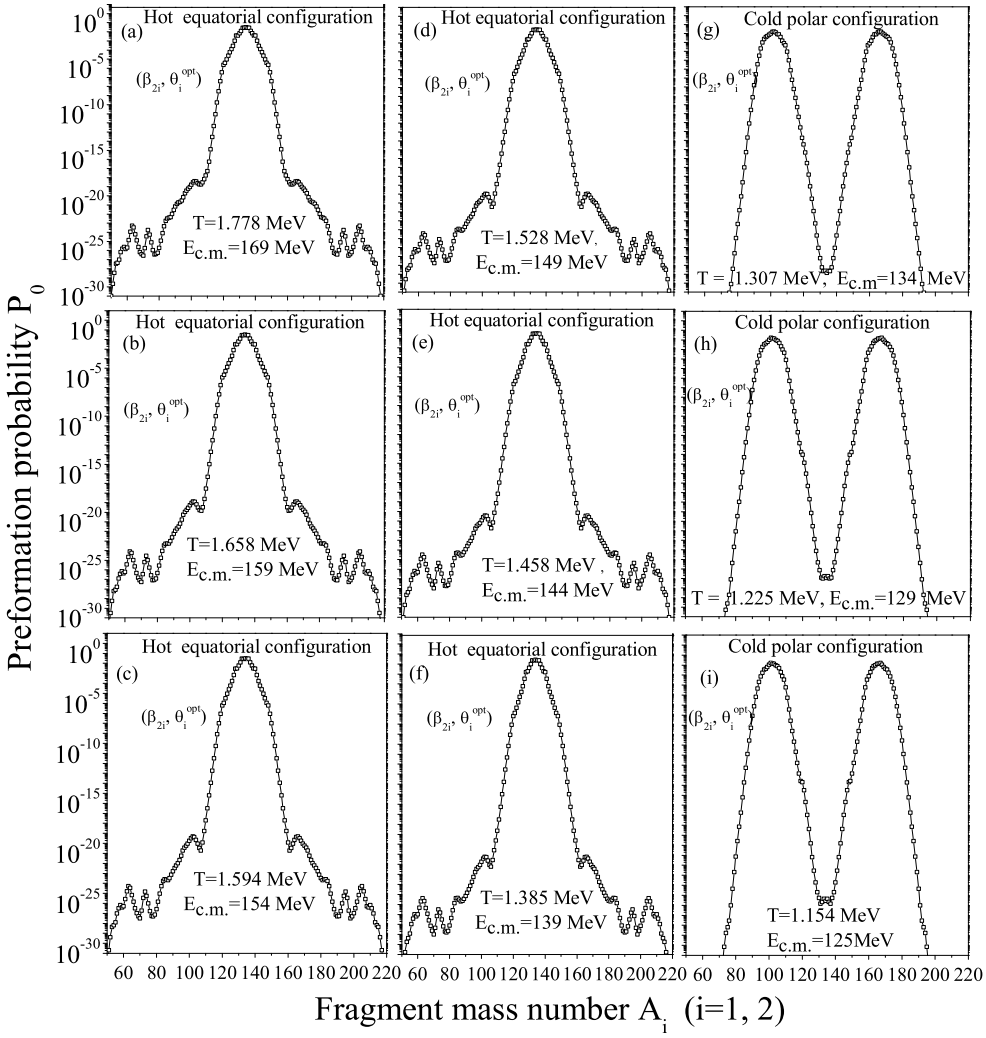

Figure 5.4 Preformation probability (P_0) for the ^{30}Si+^{238}U$\rightarrow^{268}$Sg* reaction varies as a function of fragment mass number at highest value of angular momentum (ℓ_{max}), for the neck length parameter (ΔR) fitted to the case of deformed nuclei.

is reported. This enhancement indicates that fusion is not the main process after the projectile is captured inside the Coulomb barrier. Interestingly, the evaporation residue cross-sections in the sub-barrier region with polar orientations are not fitted nicely, hence the possibility of some competing decay channel at sub-barrier energy region seems justified.

To explore this aspect further the barrier modification parameter (ΔV_B) is plotted in Fig. 5.5 as a function of angular momentum (ℓ) at two energies 169 and 129 MeV, respectively, for equatorial compact and polar non-compact configurations. The barrier

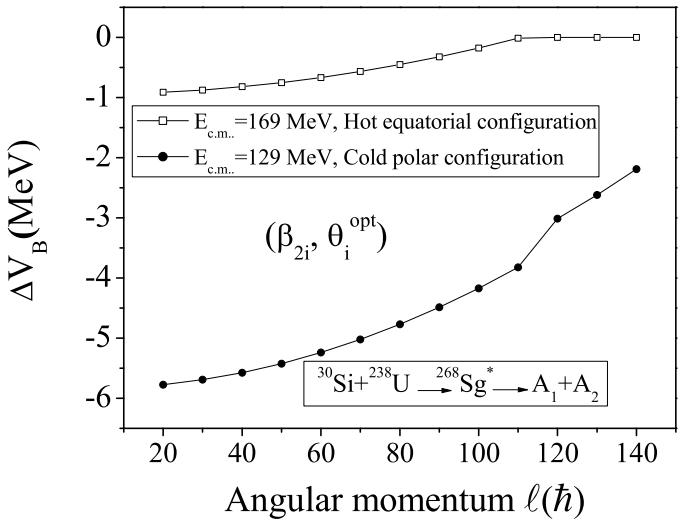

Figure 5.5 Variation of ΔV_B as function of angular momentum (ℓ) for the decay of the compound nucleus ^{268}Sg*, considering the hot compact and cold non-compact configurations, respectively at $E_{c.m.}$=169 MeV and $E_{c.m.}$=129 MeV.

modification (ΔV_B) is much higher for polar configuration than that for equatorial one. Also, the ΔV_B seems to be of greater importance at lower ℓ- values, as its magnitude decreases with increase in angular momentum.

Fig. 5.6 is plotted to see the effect of angular momentum on the barrier height (V_B), plotted as the function of fragment mass (A_2), which plays an important role for compact and non-compact configurations. It is clear from Fig. 5.6 that (i) the barrier-height increases for both the equatorial and polar configurations, respectively, at $E_{c.m.}$=169 MeV and 129 MeV with increase in fragment mass and angular momentum. The increasing behavior of V_B is same as that for the heavier nuclear system like ^{215}Fr [7]. It is relevant to mention here that the lighter nuclear system like ^{48}Cr [5] shows just opposite trend where the barrier height decreases with increase in ℓ-values. (ii) the magnitude of V_B is smaller for polar non-compact configuration as compared to equatorial compact configuration, which signifies that barrier height decreases for the use of polar orientation.

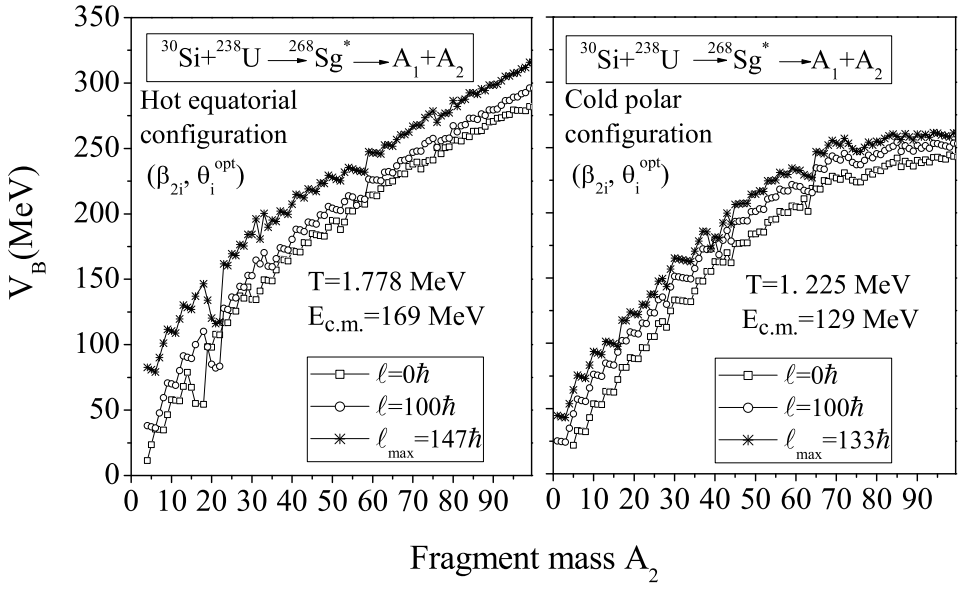

Figure 5.6 Variation of barrier height (V_B) as function of fragment mass (A_2) for the decay of ^{268}Sg* compound nucleus, using hot equatorial and cold polar configurations, at different values of angular momentum (ℓ).

5.3 Summary

The fission and neutron evaporation residue cross-sections for the ^{30}Si+^{238}U→^{268}Sg* reaction are calculated by using the Dynamical cluster decay model (DCM) at both above and below barrier energies. First the cross-sections are calculated using hot equatorial configurations of β_{2i}-static deformed nuclei. The role of spherical and β_{2i}-dynamic deformations is also included to investigate the effect of deformations on decay path of ^{268}Sg* compound nucleus. Deformations show their influence particularly for fragment mass lying in the range $70 \leq A_2 \leq 130$. Therefore the deformation effects are of immense importance for understanding the dynamics of the ^{30}Si+^{238}U→^{268}Sg* reaction. The role of cold polar configuration is explicitly examined for the sub-barrier region. A variation in the mass distribution is observed from symmetric to asymmetric in going from above barrier region to sub-barrier region, when equatorial configuration is replaced by polar configuration. This observation inturn suggest that the quasi-fission component may be competing with fission in sub-barrier region. Other important results are: (i) the barrier

height (V_B) increases with increase in energy and angular momentum. (ii) higher barrier modification (ΔV_B) is needed for sub-barrier energies, i.e., relatively larger barrier modification is required for a cold non-compact configuration as compared to hot compact configuration. (iii) The ΔV_B is reported to be least for the higher angular momentum states.

It may be noted that upto now the neutron evaporation, α-decay, heavy particle decay, fission and quasi-fission phenomenon are investigated using spherical and β_{2i}- deformed choice of fragmentations. It is now of further interest to analyze the role of higher multipole deformations in superheavy mass region, and the same is addressed in chapter 6. In addition to this, an isotopic analysis is also worked out for a variety of superheavy systems.

Bibliography

[1] R. K. Gupta, M. Balasubramaniam, R. Kumar, N. Singh, M. Manhas, and W. Greiner, J. Phys. G: Nucl. Part. Phys. **31**, 631 (2005).

[2] K. Nishio, H. Ikezoe, I. Nishinaka, S. Mitsuoka, K. Hirose, T. Ohtsuki, Y. Watanabe, Y. Aritomo, and S. Hofmann, Phys. Rev. C **82**, 044604 (2010).

[3] K. Sandhu, M. K. Sharma, and R. K. Gupta, Phys. Rev. C **86**, 064611 (2012).

[4] R. K. Gupta, M. Manhas, and W. Greiner, Phys. Rev. C **73**, 054307 (2006).

[5] B. B. Singh, M. K. Sharma, R. K. Gupta, and W. Greiner, Int. J. Mod. Phys. E **15**, 699 (2006).

[6] S. Kanwar, M. K. Sharma, B. B. Singh, R. K. Gupta, and W. Greiner, Int. J. Mod. Phys. E **18**, 1453 (2009).

[7] M. K. Sharma, G. Sawhney, R. K. Gupta, and W. Grenier, J. Phys. G: Nucl. Part. Phys. **38**, 105101 (2011).

[8] G. Sawhney, G. Kaur, M. K. Sharma, and R. K. Gupta, Phys. Rev. C **88**, 034603 (2013).

Chapter 6

Role of higher order deformations and isotopic dependence

In the previous chapter, the decay of $^{268}Sg^{*}$ was studied using DCM [1]- [7] across the Coulomb barrier. The calculations were made for ER and fission cross-sections by including the quadrupole (β_{2i}) deformations within optimum (θ_i) orientation approach. The application of optimized orientations leads to symmetric fragmentation for above barrier region (equatorial configuration) and asymmetric distribution of fission fragments for below/sub barrier region (polar configuration). In this chapter, the same concept is extended further to explore the isotopic analysis of $^{278,286}112^{*}$ [5] nuclear systems using β_{2i}-deformations. In addition to this, the higher order deformations upto hexadecapole (β_{4i}) are also included in the study of $^{278,286}112^{*}$ nuclei.

Besides Z=112 superheavy nuclei, the N/Z dependence for Z=114 and Z=115 nuclear systems are also explored in the DCM framework. In the decay of $^{290,292}114^{*}$ nuclei [6], the isotopic dependence is analyzed via the distribution of the preformation probability and fragmentation potential of the decaying fragments. However, N/Z effects in Z=115 isotopes [7] are investigated by addressing the channel cross-sections of $^{289,291,293}115^{*}$ nu-

clei.

The organization of chapter is as follows: Brief introduction regarding Z=112, 114 and 115 nuclei is discussed in Sec. 6.1. The DCM calculated results are presented in Sec. 6.2 and the summary of the results is described in Sec. 6.3.

6.1 Introduction

In heavy ion reactions, the experimental and theoretical developments to examine the decay properties of nuclei located in the superheavy mass region is mainly associated with the formation of compound nucleus and its subsequent decay. To explore this, certain factors such as angular momentum, deformation, orientation, isospin (N/Z-ratio) effect etc have been studied extensively, in order to extract useful information regarding the dynamics of superheavy reactions.

To uplift the knowledge about the superheavy reaction dynamics, the understanding of deformation and orientation degrees of freedom is extremely essential. As the interaction potential is highly sensitive to the choice of deformation, henceforth the inclusion of the higher multipole deformations is equally important to address heavy ion reactions. To account this issue, the ^{40,48}Ca+^{238}U$\rightarrow^{278,286}112^{*}$ reactions [8] are studied using β_{2i} and β_{4i} deformations in framework of the Dynamical cluster decay model (DCM) [1]- [7]. The addressal of above reactions is also important from the point of view that one can analyze the role of isospin (N/Z ratio) in the decay of Z=112 isotopes with A_{CN}=278 and 286. According to [8], less fusion probability is measured for ^{40}Ca+^{238}U reaction as compared to ^{48}Ca+^{238}U. Hence, isotopic analysis of these reactions show higher contribution of quasi-fission for ^{40}Ca-induced reaction.

The role of different N/Z ratio can also analyzed by keeping the projectile intact and

varying the target nuclei. In view of this, the $3n$, $4n$ and $5n$ decay of $^{290,292}114^*$ nuclei formed in ^{48}Ca+^{242,244}Pu reactions [9, 10] are studied in DCM framework [1]- [7] over a wide range of excitation energies. For $^{290}114^*$ the maximum excitation energy of 45 MeV was assigned [11], where only $3n$ and $4n$ evaporation channels were reported. However, Ellison *et al.* [9] observed a new isotope $^{285}114$ in the $5n$ evaporation product of $^{290}114^*$ at relatively higher energy, of the order of 50 MeV. Besides $^{290}114^*$, another Z=114 isotope, $^{292}114^*$ has also been investigated experimentally at excitation energies E^*_{CN} = 36.1-39.5 MeV and E^*_{CN} = 39.8- 43.9 MeV in GSI using TASCA recoil separator [10]. It is relevant to mention here that fission and quasi-fission cross-sections are also reported in [12] in the energy range 27-37 MeV for $^{292}114^*$ nucleus. In addition to this, the understanding of ^{48}Ca+^{241,243,245}Am reactions, in which ^{48}Ca+^{243}Am reaction is experimentally observed in [13], also provide an opportunity to explore the isotopic effects, associated with superheavy mass region.

6.2 Calculations and Results

Here in Sec. 6.2.1, the role of higher order deformations, included upto hexadecapole (β_{4i}) is examined for $^{278,286}112^*$ nuclei formed in the ^{40,48}Ca + ^{238}U reactions at $E_{c.m.}$=230 MeV and 180 MeV. First the effect of hexadecapole (β_{4i})-deformation is observed on the compact angle of nuclear structure and finally on the decay path of $^{278,286}112^*$ nuclei. Subsequent to this, in Sec. 6.2.2, the N/Z dependence is investigated for the decay of Z=112, 114 and 115 nuclei, published in [5], [6] and [7] respectively, using β_{2i}-deformations with optimum orientation approach.

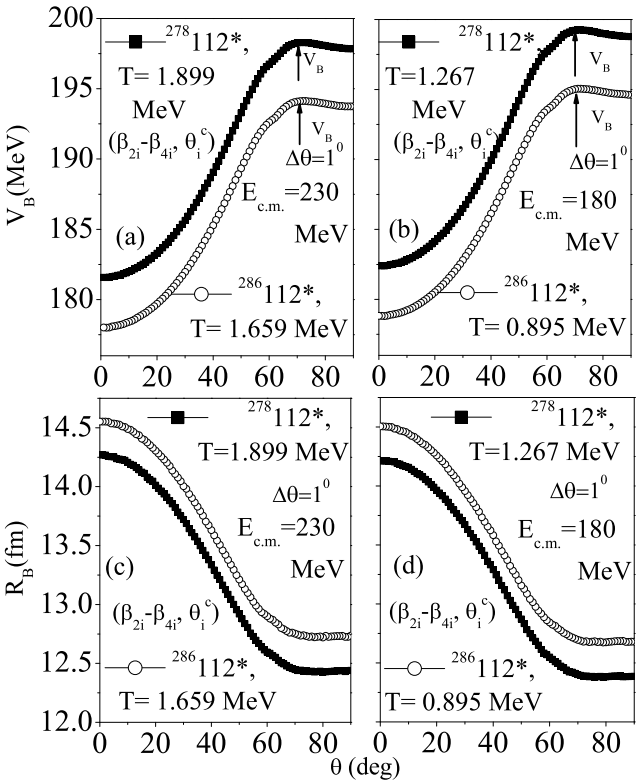

Figure 6.1 (a ,b) Barrier height plotted as a function of orientation angle (θ_i) for ^{40,48}Ca+^{238}U$\rightarrow^{278,286}$112* reactions at $E_{c.m.}$=230 MeV and 180 MeV respectively. (c, d) Same as above figures, but for barrier position.

6.2.1 Role of higher order deformations

The orientations associated with quadrupole deformations, which are included here for best fit of data, are optimized with respect to signs of (+/-, zero) of quadrupole deformations alone for hot and cold configurations [14]. The optimized orientations help us to decide the most compact and elongated nuclear structure on the way to compound nuclear formation or decay respectively via equatorial and polar interactions. On the other hand, when higher order deformations are taken into account, the scenario of compactness of the nuclear systems is modified slightly, the most compact system can be observed for θ_c<90^0 [15]. In context to this observation, Fig. 6.1 (a,b) is plotted, in which the variation of barrier height shows that the orientation angle at which the compactness occurs is less than 90^0 as the barrier height is maximum at $\sim$ 72^0 for both nuclei. It may be

noted that the compact angle with higher multipole deformations for $^{286}112^{*}$ nucleus is observed in [15]. Our aim here is to check the degree of compactness for lighter isotope $^{278}112^{*}$ alongwith the effect of temperature on the barrier height and barrier position of the $^{278}112^{*}$ and $^{286}112^{*}$ compound nuclear systems. Fig. 6.1 (c,d) shows the variation of barrier position with orientation angle (θ_i) for $^{278}112^{*}$ and $^{286}112^{*}$ nuclei, and the most compact structure is formed for the lower values of R_B and highest value of V_B. So one may conclude that the compact structure with higher multipole deformations for $^{278}112^{*}$ and $^{286}112^{*}$ nuclei is obtained at θ_c=72^0, independent of energy (temperature) involved. However it may be noted that magnitude of V_B and R_B is modified slightly with inclusion of temperature effects. Hence one can say that the inclusion of higher order deformations provide an opportunity to understand the compact configuration of compound nuclear systems, as the compact angle gets modified while going from quadrupole to hexadecapole deformations.

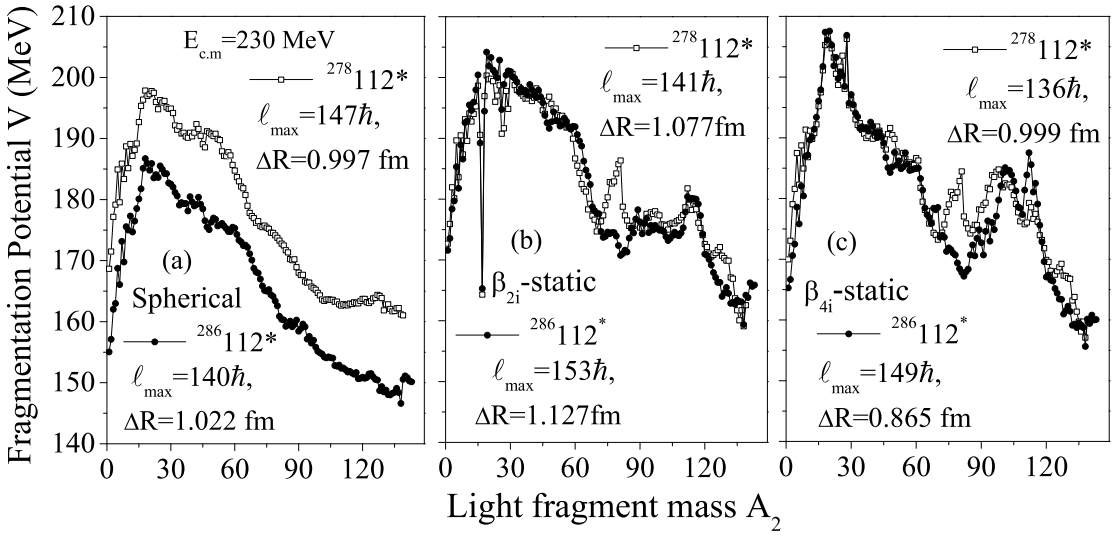

Figure 6.2 Comparative analysis of fragmentation potentials for ^{40,48}Ca+^{238}U$\rightarrow^{278,286}112^{*}$ reactions as a function of light fragment mass (A_2) for (a) spherical (b) β_{2i}-static with "optimum" orientations (θ_i^{opt}) and (c) β_{4i}-static with "compact" orientations (θ_i^c) at ℓ_{max} values, calculated at energy $E_{c.m.}$=230 MeV, using hot equatorial configuration.

In order to investigate the role of higher order deformations on decaying fragments of $^{278,286}112^{*}$ nuclei, Fig. 6.2 is plotted, which shows the change in the fragmentation path while going from spherical to deformed (β_{2i} to β_{4i}) choice of fragments. Smooth fragmentation potential can be seen for the spherical fragmentation approach for both compound nuclei. On the contrary, the fragmentation structure of $^{278,286}112^{*}$ nuclei, shown in Fig. 6.2 (b) and Fig. 6.2 (c), exhibit an emergence of valleys in the heavy mass fragment (HMF) region for the use of static- β_{2i} and β_{4i} choices of deformations. The HMF region affected with β_{2i}-static deformed fragmentation is A_2=70-85 which changes to A_2=70-98, by including β_{4i}-static deformations. However, the fragmentation pattern for light particles and fission fragments with β_{2i} and β_{4i} deformations remain almost identical, therefore the fission cross-sections for the entire energy range are calculated for β_{2i}-deformed fragmentation only, results of which are discussed in subsequent section. It is relevant to mention that the occurrence of sharp minima in Fig. 6.2 (b) at A_2 = 17 is associated with the inappropriate values of optimized β_{2i}- deformations for ^{17}B fragment [4]. However it doesn't effect the overall cross-sections as the penetrability (not shown here) of this fragment comes out to be negligibly small.

6.2.2 Role of isospin in the decay of Z=112, 114 and 115 superheavy isotopes

Isotopic dependence in Z=112 nuclei

In order to look for the role of isospin in the decay of Z=112 nuclei, the fission cross-sections of $^{278}112^{*}$ and $^{286}112^{*}$ nuclei are analyzed within the wide range of excitation energy $E^{*}_{CN}\approx$ 19-90 MeV in the framework of DCM [1]- [7]. The cross-sections are calculated at above and below the Coulomb barrier, same as that of $^{268}\mathrm{Sg}^{*}$, discussed in

previous chapter. In the decay of ^{268}Sg*, neutron as well as fission cross-sections both are available to understand the orientation-effects on the decaying fragments. However, for ^{278,286}112* compound nuclei, we have confined to fission cross-sections in reference to [8]. In view of this, isospin dependence is depicted through the structural changes in the decay of fission fragments only, not for the whole mass range.

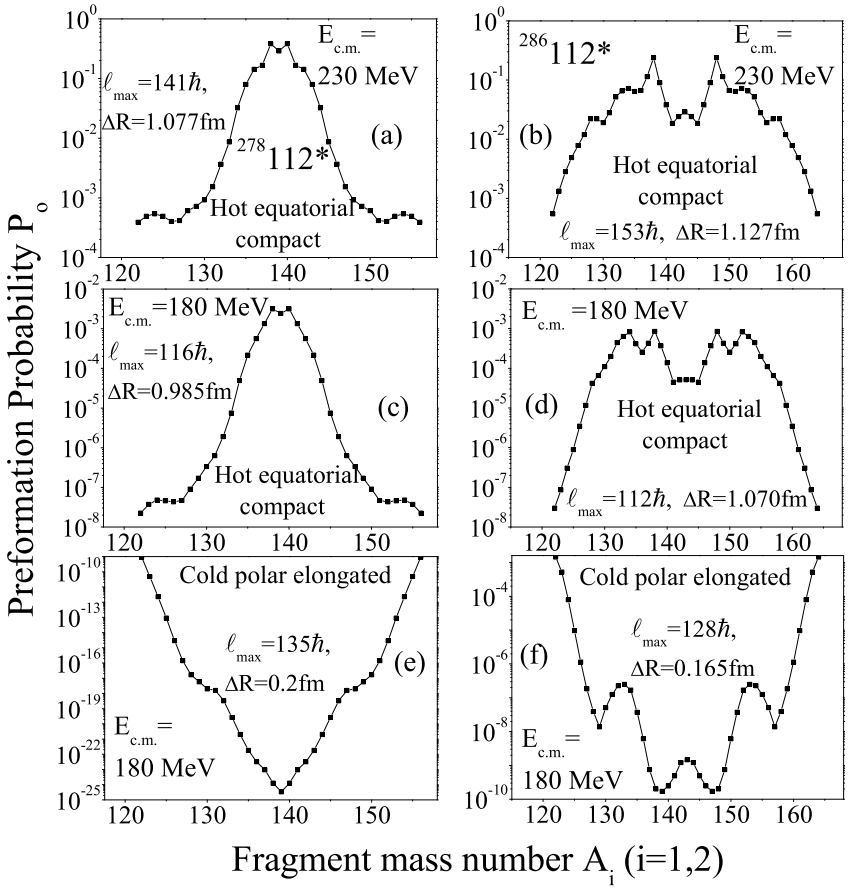

Figure 6.3 Plot of preformation probability varies with fragment mass for symmetric fission channels of ^{40,48}Ca+^{238}U$\rightarrow^{278,286}$112* reactions at (a,b) $E_{c.m.}$ =230 MeV and (c,d) 180 MeV, using hot equatorial configuration and (e,f) $E_{c.m.}$ =180 MeV with cold polar configuration.

In context to this, Fig. 6.3 is plotted in which the preformation probability of symmetric fragment mass at above and below barrier energies is shown. This figure clearly depicts that relatively more symmetric structure is evident for the fission component of ^{278}112* compound nucleus as compared to ^{286}112* nucleus at extreme energies across the

barrier i.e. $E_{c.m.}$= 230 and 180 MeV for the use of hot orientation approach. One may notice that, no significant change in structure is observed at below barrier region using hot equatorial configuration of $^{278,286}112^{*}$ nucleus. Only the magnitude of preformation factor reduces while going from above barrier ($E_{c.m.}$= 230 MeV) to sub-barrier ($E_{c.m.}$= 180 MeV) region. For the comparative analysis of cold polar configuration in the dynamics of ^{40,48}Ca+^{238}U$\rightarrow^{278,286}112^{*}$ reactions, Fig. 6.3 (e,f) is plotted for symmetric decaying fragments within cold orientation approach at lowest energy of 180 MeV. Here one can see that the preformation factor for the decay of both nuclei decreases drastically when the hot equatorial configuration are replaced by cold polar ones at the sub-barrier region. The suppression in the magnitude of preformation probability is higher for $^{278}112^{*}$ nucleus as compared to $^{286}112^{*}$, hence more contribution of quasi-fission may be anticipated for lighter superheavy isotope. It is relevant to mention that, as the distribution of the preformation probability is calculated using collective clusterization, so the suppression in the magnitude of the symmetric fragments reveals the fact that the relative probability may increase for the asymmetric fragments which may lead to the phenomenon of quasi-fission.

To have a better description of fragment distribution in fission region, Fig. 6.4 is plotted which is same as that of Fig. 6.3, but with proper description of atomic and mass numbers. Precisely, this figure gives the exact fragment distribution of the decaying fragments plotted upto $A_{CN}/2$. It is clear that the Z-number, contributing towards the fission cross-sections are lying in the range $Z_2\sim$49-56. However mass numbers of decaying fragments contributing towards fission cross-sections are A_2=122-139 and A_2=127-143 respectively for $^{278}112^{*}$ and $^{286}112^{*}$ compound nuclei. Such fragment identification and their respective emergence in the decay process, provide an interesting aspect related with dynamics of heavy ion induced reactions.

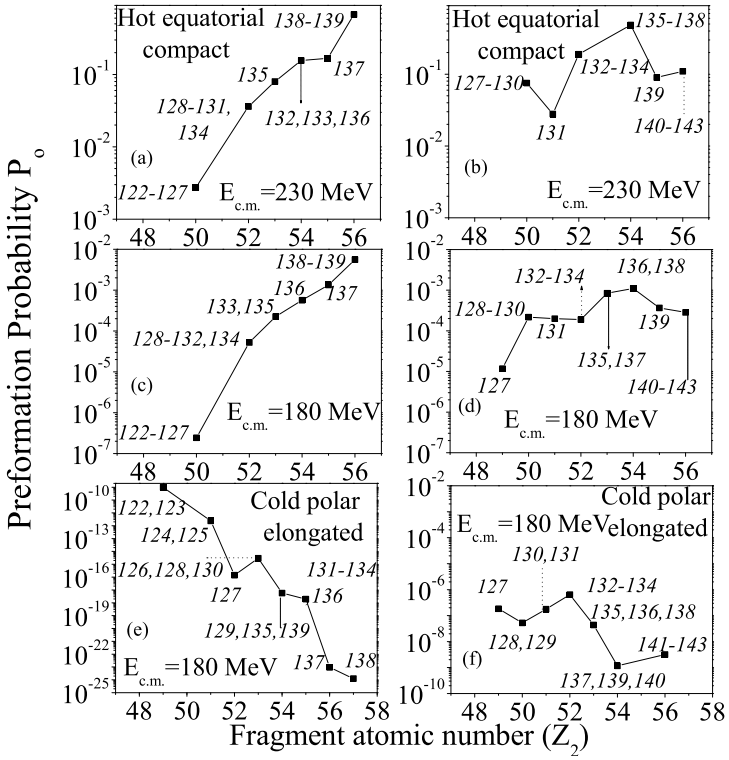

Figure 6.4 Preformation probability as a function of symmetric fragment's atomic number for the decay of $^{278,286}112^{*}$ compound nuclei associated with (a,b,c,d) equatorial and (e,f) polar configurations, (*the mass numbers of decaying fragments are shown within for each atomic number*).

Isotopic dependence in Z=114 nuclei

It is worth mentioning that the role of isospin in Z=112 nuclei is checked mainly to see the structural changes in the fission fragments (equivalently to address quasi-fission), as the experimental data is taken to study the fission cross-sections only. On the other hand, as both neutron evaporation and fusion-fission components are investigated for Z=114 nuclei using DCM in [6], henceforth competing decay channels in the form of ER and fission provide overall information regarding post compound nucleus dynamics. The inclusion of higher order deformations are not discussed here, as their effect on the neutron evaporation and fission fragment region remains silent, similar to the one discussed above in context of Z=112 nuclei.

In view of this, Fig. 6.5 is plotted for two extreme values of angular momentum ℓ=0

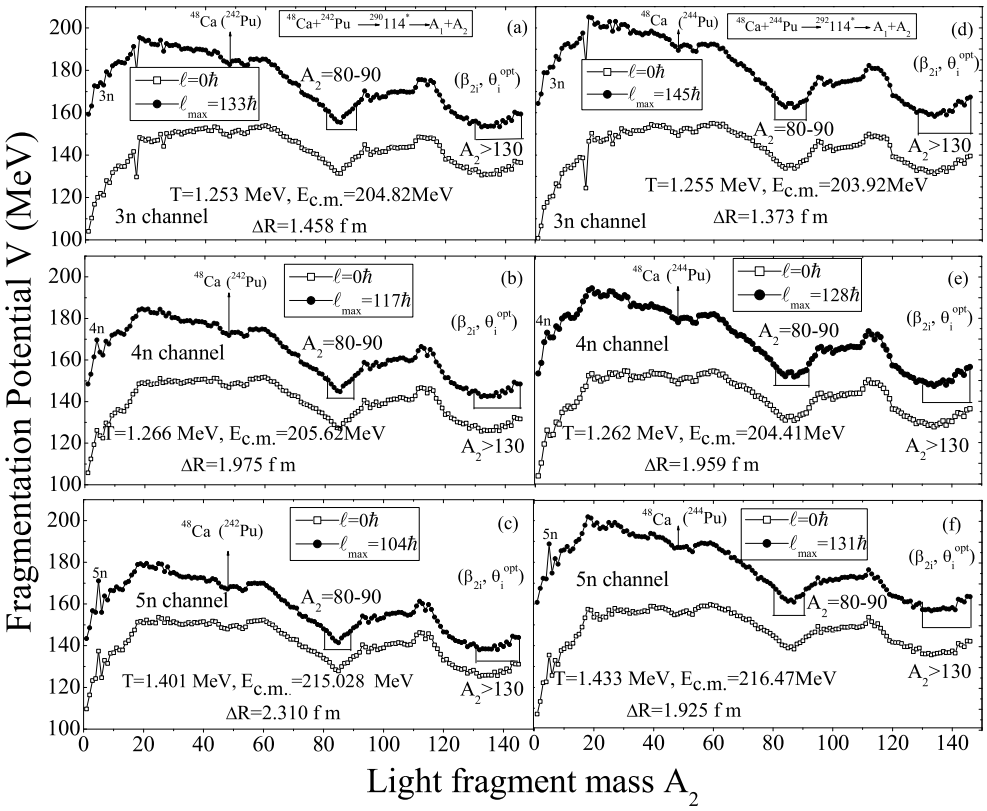

Figure 6.5 Fragmentation potentials for ^{48}Ca+^{242,244}Pu$\rightarrow^{290,292}$114* reactions as a function of light fragment mass (A_2) with β_{2i} deformations and "optimum" orientations (θ_i^{opt}) at $\ell = 0$ and ℓ_{max} values.

and ℓ_{max} at the neck-length parameters of $3n$, $4n$ and $5n$ decay channels for comparable energies. Following interesting points can be observed from Fig. 6.5: (i) The fragmentation paths for ^{290}114* and ^{292}114* yield similar behavior, independent of energy of projectile; (ii) strong minima are seen for evaporation residues as well as for the fission fragments with A_2>130 along with heavy mass fragment (HMF) window $80 \leq A_2 \leq 90$; (iii) the structure of V(A_2) is nearly independent of the ℓ-values for all evaporation channels; (iv) a valley (minima in potential) is seen consistently for ^{48}Ca+^{242,244}Pu channels, for ^{290}114* and ^{292}114* nuclei respectively. Consecutively, one can realize that the fragmentation path remains nearly identical with the inclusion of two neutrons to ^{290}114* nucleus.

The role of N/Z ratio is also tested by adding or subtracting two successive neutrons to the different compound nuclei corresponding to Z=114. The comparison between the

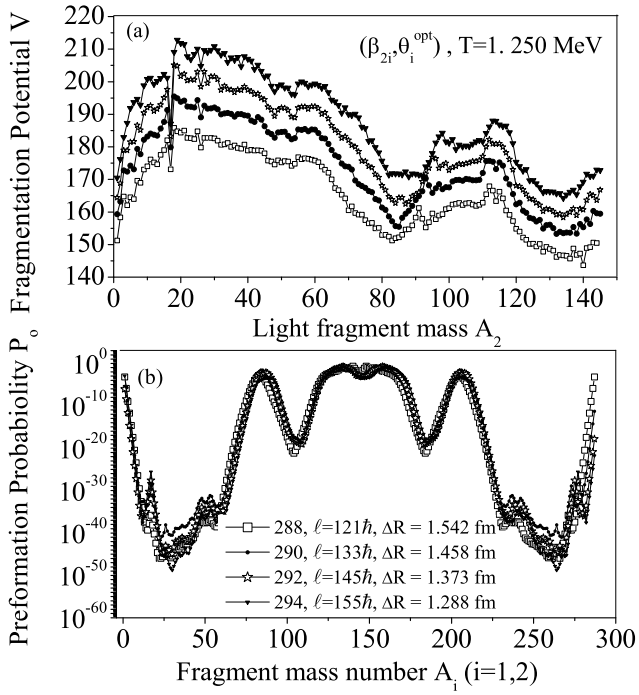

Figure 6.6 (a) Fragmentation potential and (b) preformation probability for Z=114 isotopes at neck-length parameter of $3n$ neutron-evaporation channel using β_{2i}-deformations and optimum orientations (θ_i^{opt}) at $\ell = \ell_{max}$.

decay profile of various isotopes of Z=114 nuclei is shown in Fig. 6.6. Here two more isotopes of Z=114 with A_{CN} = 288 and 294 are considered. The isotopic analysis is made only in reference to $3n$ decay by extrapolating neck-length parameter 'ΔR', obtained for $^{290}114^*$ and $^{292}114^*$ at T≈1.25 MeV. Fig. 6.6 (a) represents the fragmentation potential as a function of light fragment mass (A_2) for different isotopes of Z=114 superheavy nucleus. Broadly speaking the fragmentation path is quite similar when two neutrons are added subsequently in Z=114 and N=174, i.e. to $^{288}114^*$ nucleus, to form $^{290}114^*$, $^{292}114^*$ and $^{294}114^*$ nuclei. Although some slight variations are seen in heavy mass fragment (HMF) and fission region but in general the trend is same. Similar results can be depicted from Fig. 6.6 (b), where the preformation probability is plotted for different Z=114 superheavy nuclei. Hence it can be concluded that addition of two, four and six neutrons to $^{288}114^*$ (or changing N/Z ratio) govern only small but not significant change in the fragmentation/preformation path of HMF and fission fragments of different compound

Table 6.1 The DCM calculated neutron evaporation residue cross-sections (σ_{xn}, x=2, 3 and 4), for the decay of $^{289}115^*$ and $^{293}115^*$ compound systems, formed in ^{48}Ca+^{241}Am and ^{48}Ca+^{245}Am reactions, respectively, at the same CN excitation energy and neck-length parameter as that of $^{291}115^*$.

	^{48}Ca+^{241}Am						^{48}Ca+^{245}Am				
xn	E^*_{CN} (MeV)	T (MeV)	ℓ_{max} ($\hbar$)	P_0	P	σ^{DCM}_{xn} (pb)	T (MeV)	ℓ_{max} ($\hbar$)	P_0	P	σ^{DCM}_{xn} (pb)
$2n$	33.37	1.146	117	1.62×10^{-8}	6.69×10^{-10}	0.0637	1.138	137	1.10×10^{-10}	2.01×10^{-8}	1.88
$2n$	34.12	1.158	118	2.67×10^{-10}	5.69×10^{-9}	0.444	1.150	138	1.67×10^{-11}	1.25×10^{-7}	11.40
$2n$	36.15	1.192	119	2.83×10^{-10}	6.24×10^{-9}	0.509	1.183	139	4.74×10^{-11}	1.26×10^{-7}	14.60
$3n$	33.37	1.146	109	5.16×10^{-11}	2.26×10^{-7}	4.13	1.138	129	9.64×10^{-14}	1.18×10^{-5}	1.95
$3n$	34.30	1.161	110	2.08×10^{-11}	2.46×10^{-7}	5.19	1.153	130	2.88×10^{-13}	1.88×10^{-5}	2.63
$3n$	36.15	1.192	110	6.58×10^{-11}	4.80×10^{-7}	14.10	1.183	131	6.26×10^{-14}	3.57×10^{-5}	5.15
$3n$	40.34	1.258	114	2.01×10^{-10}	9.74×10^{-8}	8.36	1.249	134	2.43×10^{-12}	8.61×10^{-6}	1.69
$3n$	44.97	1.327	118	7.54×10^{-10}	1.47×10^{-8}	2.38	1.318	138	1.13×10^{-12}	1.88×10^{-6}	0.40
$4n$	40.34	1.258	95	6.17×10^{-13}	1.72×10^{-4}	3.98	1.249	115	3.24×10^{-14}	2.12×10^{-3}	0.789
$4n$	44.97	1.327	100	5.58×10^{-14}	1.62×10^{-4}	16.80	1.318	120	1.07×10^{-15}	1.84×10^{-3}	1.32

nuclei corresponding to Z=114, but no such change is observed for the evaporation residue region.

Isotopic dependence in Z=115 nuclei

The decay of $2n$, $3n$ and $4n$ evaporation channels of $^{291}115^*$, formed in ^{48}Ca+^{243}Am reaction is already discussed in chapter 4, where a nice fitting of the experimental data [13] is obtained in the fixed neck-length parameter range 1.2 to 2.00 fm, shown in Fig. 4.3 (of chapter 4). In order to understand the effect of the isotopic dependence on the decay of Z=115 nuclei, the calculations are made for ^{48}Ca+^{241}Am and ^{48}Ca+^{245}Am reactions, using the same neck-length parameters as are extracted for the ^{48}Ca+^{243}Am reaction. As the structural changes remain silent for neutron evaporation, evident from the above Fig 6.2 (b) and Fig 6.5, hence it will be of further interest to analyze the effect of isospin on magnitudes of the output parameters such as preformation probability (P_0), penetration probability (P) and finally on the channel cross-sections of Z=115 nuclei formed by using

different target masses. The calculated cross-sections of neutron evaporation channels ($2n$, $3n$ and $4n$) for $^{289}115^*$ and $^{293}115^*$ nuclei are given in Table 6.1, which are predicted over a wide range of compound nucleus energies. Thus, systematic variation in xn cross-sections as a function of target mass (241, 243 and 245) may impart useful information in reference to isotopic dependence of Z=115 element. In addition to this, the magnitude of the preformation and penetration probabilities are also modified for the decay of $^{289}115^*$ and $^{293}115^*$ superheavy nuclei, as compared to $^{291}115^*$ superheavy nuclei.

6.3 Summary

Summarizing, in this chapter, the comparative analysis of the dynamics involved in $^{278}112^*$ and $^{286}112^*$ nuclei is carried out over a wide range of center of mass energies, above and below the Coulomb barrier. With the inclusion of β_{4i}-deformations, the compact angle is modified which in turn affects the decay path of compound nuclei. Confining to optimum orientations associated with β_{2i} deformations, the symmetric fission is dominant for hot equatorial configuration, which gets reversed when hot configuration is replaced by the cold polar one. In view of this, higher contribution of quasi-fission is anticipated for the neutron deficient isotope of Z=112. To explore the isotopic dependence further in superheavy mass region, the $3n$, $4n$ and $5n$ decay cross-sections of ^{48}Ca+^{242,244}Pu$\rightarrow^{290,292}114^*$ reactions are also calculated by using DCM. No significant changes are observed in the fragmentation path of the Z=114 isotopes. The fragmentation and preformation behavior remain nearly identical for $^{288}114^*$, $^{290}114^*$, $^{292}114^*$ and $^{294}114^*$ compound nuclei. For Z=115 isotopes, the neutron evaporation cross sections are calculated for $^{289}115^*$ and $^{293}115^*$ compound nuclei formed in ^{48}Ca+^{241}Am and ^{48}Ca+^{245}Am reactions and compared with decay cross-sections of $^{291}115^*$ to address the isotopic dependence for Z=115

isotopes.

The outcome of this thesis and the work described in chapters 3-6, are summarized in chapter 7.

Bibliography

[1] R. K. Gupta, S. K. Arun, R. Kumar, and Niyti, Int. Rev. Phys. (I.RE.PHY.) **2**, 369 (2008).

[2] M. Kaur, R. Kumar, and M. K. Sharma, Phys. Rev. C **85**, 014609 (2012).

[3] G. Kaur and M. K. Sharma, Nucl. Phys. A **884**, 36 (2012).

[4] K. Sandhu, M. K. Sharma, and R. K. Gupta, Phys. Rev. C **86**, 064611 (2012).

[5] K. Sandhu, G. Kaur, and M. K. Sharma, Nucl. Phys. A **921**, 114 (2014).

[6] K. Sandhu and M. K. Sharma, Braz. J. Phys. **44**, 64 (2014).

[7] R. Kumar, K. Sandhu, M. K. Sharma, and R. K. Gupta, Phys. Rev. C **87**, 054610 (2013).

[8] K. Nishio, S. Mitsuoka, I. Nishinaka, H. Makii, Y. Wakabayashi, H. Ikezoe, K. Hirose, T. Ohtsuki, Y. Aritomo, and S. Hofmann, Phys. Rev. C **86**, 034608 (2012).

[9] P. A. Ellison *et al.*, Phys. Rev. Lett. **105**, 182701 (2010).

[10] J. M. Gates *et al.*, Phys. Rev. C **83**, 054618 (2011).

[11] Yu. Ts. Oganessian *et al.*, Phys. Rev. C **70**, 06460 (2004).

[12] M. G. Itkis *et al.*, J. Nucl. and Radiochem. Sci. **3**, 57 (2002).

[13] Yu. Oganessian *et al.*, Phys. Rev. Lett. **108**, 022502 (2012); Phys. Rev. C **87**, 014302 (2013).

[14] R. K. Gupta, M. Balasubramaniam, R. Kumar, N. Singh, M. Manhas, and W. Greiner, J. Phys. G: Nucl. Part. Phys. **31**, 631 (2005).

[15] R. K. Gupta, M. Manhas, and W. Greiner, Phys. Rev. C **73**, 054307 (2006).

Chapter 7

Summary and outlook

In this thesis the possible decay modes of a variety of superheavy nuclear systems are investigated using the collective clusterization approach. The Preformed cluster model (PCM) is used to understand the ground state decays of nuclei to explore the phenomenon of α-decay and heavy particle radioactivity (HPR) and the Dynamical cluster decay model (DCM), has been applied to study the decay paths of excited compound nuclear systems formed in superheavy mass region. The effects of various features such as excitation energy, angular momentum, deformations, orientations, barrier modification and shell effects etc have been extensively investigated in view of binary fragmentation analysis based on the well known Quantum Mechanical Fragmentation Theory (QMFT).

An overview of present status of research and general introduction related to this work have been discussed in Chapter 1. The details of the methodology i.e Preformed cluster model (PCM) and Dynamical cluster decay model (DCM), based on the Quantum Mechanical Fragmentation Theory (QMFT), are discussed in Chapter 2. In DCM the temperature dependence is included in various interaction potentials such as binding energies, Coulomb potential, proximity potential whereas no temperature dependence is applicable in PCM, as it deals with ground state decay mechanisms. Although, the

deformation and orientation effects are duly incorporated in both formalisms.

First in order to address the role of shell effects for the superheavy mass region, the decay analysis of $^{296}116^{*}$ and $^{266}Rf^{*}$ compound systems is carried out through DCM in Chapter 3. The shell effects with proton magic Z=114, 120, 126 and neutron magic N=184 are included to calculate the excitation functions of neutrons at different energies. In the decay of $^{296}116^{*}$ nucleus, within sticking approach of moment of inertia (I_S), the lowest magnitude of the fragmentation potential is obtained for Z=126 and N=184 magic pair. Consequently, highest channel cross-sections are calculated for the same magic shell closures, which implies that the proton magic Z=126 and neutron magic N=184 can be taken as the best suited magic pair to address the neutron evaporation channels. The magicity criteria is further explored by understanding the neutron evaporation channels of $^{266}Rf^{*}$ nucleus by including the non-sticking moment of inertia (I_{NS}). Again the fragmentation behavior shows minima for Z=126 and N=184 magic shell pair. In addition to this, the preformation probability for all the neutron decay channels remains highest for the Z=126 and N=184 magic pair as compared to other superheavy shell closures. Hence on the basis of the fragmentation potential, preformation probability and channel cross-sections analysis of $^{296}116^{*}$ and $^{266}Rf^{*}$ compound nuclei, Z=126 and N=184 magic shell closures are considered as the best candidates to address the neutron evaporation decay channels of the superheavy nuclei. The fission cross-sections, however, support that Z=120 starts competing with Z=126 proton magic.

Using Z=126 and N=184 closures, neutron evaporation channels of various superheavy nuclei such as $^{297}117^{*}$, $^{291}115^{*}$ and $^{290,292}114^{*}$ are investigated within the framework of the DCM. In this chapter, the decay of $^{297}117^{*}$ compound nucleus is discussed with the above magic shell criteria. The dynamics of other nuclei are discussed in the subsequent chapters. In order to investigate the role of deformations, the decay of $^{297}117^{*}$ CN is studied by

considering spherical as well as deformed fragmentation approaches with corresponding orientations. The measured data could not be fitted to the fragmentation potentials calculated for spherical nuclei. However, with the inclusion in the deformation effects included upto β_{2i}, the available data for $2n$ and $3n$ decay cross-sections could be addressed quite nicely but the $4n$-decay cross-sections are underestimated by about 25%. The ^{4}He decay cross-section is then added to the $4n$-cross-section to attain the experimental value, which indicates that ^{4}He decay is contributing towards $4n$ cross-section at E^{*}_{CN}=39.3 MeV and 35.3 MeV. The smooth fragmentation behavior is observed for the spherical consideration whereas relatively more structure in the decay path can be seen with the inclusion of the deformation effects. Within the deformed approach, the angular momentum effects on the fragmentation path for this reaction remain silent. The magnitude of ℓ_{min} and ℓ_{max}, calculated from the penetration and preformation probabilities and from channel cross-sections, are reported to be highest for $2n$ cluster and lowest for the $4n$ cluster. In addition to this, the barrier lowering parameter (ΔV_B), which is the inbuilt property of DCM, is calculated to be least for the heaviest neutron cluster and for the higher angular momentum states.

In Chapter 4, the neutron decay channels of $^{291}115^{*}$ nuclear system formed via ^{48}Ca + ^{243}Am reaction are investigated in the framework of DCM. The addressal of $^{291}115^{*}$ nuclear system is required to explore the importance of deformation effects as only $2n$-cross-sections are fitted with the spherical choice of fragments. To understand the dynamics involved through $3n$ and $4n$ decays of $^{291}115^{*}$ compound nucleus, the deformation effects upto β_{2i} are highly desirable. The PES for the spherical approach shows symmetric fission fragmentation, whereas asymmetric peaks in heavy fragment mass region are observed for the deformed choice. The effects of dynamic deformations up to β_{2i} are also investigated for $2n$-decay at E^{*}_{CN}=33.37 MeV. The PES remain almost identical for the static and

dynamic deformed approach, as the temperatures involved are quite small lying in the range T=1.1-1.3 MeV. The only difference lies in the fact that higher magnitude of neck-length parameter and lower ℓ_{max} values are required to address the $2n$-decay through dynamic deformations as compared to static β_{2i}-deformations. Further the neck-length parameters required to fit the $2n$, $3n$ and $4n$ evaporation channels varies smoothly with CN excitation energy. The neck-length (representing the reaction time) is lowest for $2n$ channel and remains highest for the case of $4n$-decay channel. Following the systematics of the neck-length variation, the $2n$, $3n$ and $4n$ decay channels are also predicted at the bass barrier, which could be of interest for the future experiments.

In addition to the neutron evaporation, the ground state decays such as α-emission and heavy particle radioactivity (HPR) are also discussed in this chapter. The α-decay chains from $^{287}115$, $^{288}115$ and $^{289}115$ nuclei are investigated by using the Preformed cluster model (PCM) for spherical and deformed fragmentation approaches. A nice fitting of the experimentally observed half-lives is obtained with in a constant scaling factor in penetration probability. The half-lives of α-decay chains prefer "hot" optimum orientations, rather than the usual "cold" optimum orientations for α-decays. Using the same orientation approach i.e. "hot" optimum orientations, an attempt is made to examine the possibility of heavy cluster emission from $^{278}113$, $^{287-289}115$ and $^{293,294}117$ isotopes resulting in a doubly magic ^{208}Pb daughter or its neighboring nuclei. The calculations are performed within the framework of Preformed cluster model (PCM) using Prox-77 and Prox-00 interaction potentials. The decay structure remains almost identical for both proximity potentials with spherical as well as deformed fragmentation approach. Further the half-lives with the use of both proximity potentials are predicted over a wide range of the neck-length parameters, which are further helpful for the future experimental studies. In addition to this, the importance of shell effects are also explored for HPR. The

emergence of most favored cluster is independent of the choice of superheavy magic shell closures Z=114, 120, 126 and N=184.

Besides the deformation effects, the explicit role of orientations is also addressed in Chapter 5 by studying the dynamics of ^{268}Sg* nucleus formed in the ^{30}Si+^{238}U reaction. The decay of compound nucleus ^{268}Sg* has been investigated through DCM approach, over a wide range of center-of-mass energies $E_{c.m.}$=125-169 MeV, where both the neutron evaporation residues ($3n$, $4n$ and $5n$) and fission cross-sections are measured at below and above barrier energies. At first the cross-sections are calculated for the "hot-optimum" orientations including β_{2i}-static fragmentation approach. Using this, the specific role of spherical as well as dynamic deformations is investigated to check the effect of deformations on the decay path of ^{268}Sg* compound nucleus. The deformation effects (β_{2i}-static and dynamic) show their influence in the mass range $70 \leq A_2 \leq 130$, whereas the fragment mass distribution remains identical for LP's and IMF's. For spherical consideration larger number of fission fragments contribute towards total cross-section, however this number gets reduced significantly when deformation effects of decaying fragments are included.

Further the cold polar approach is applied to understand the dynamics of sub-barrier regions, whereas the above barrier cross-sections are fitted for the hot-equatorial configurations of nuclei. The symmetric mass distribution is observed for the hot equatorial configuration which becomes asymmetric for the cold polar configuration at below barrier energies. The symmetric fragment distribution reveals the fact that the fusion-fission can be main disintegration mode for the above barrier region. On the other hand, the emergence of asymmetric component shows the signature of quasi-fission for below/sub-barrier region. The overestimated cross-section at lowest energy supports the fact that quasi-fission may competes with fission at below-barrier energies. This is because barrier height (V_B) decreases for the cold polar orientations as compared to hot equatorial.

Further it is shown that the barrier height (V_B) increases with increase in fragment mass and angular momentum for both the configurations. Also to address the sub-barrier region, larger 'barrier modification' ΔV_B is needed for cold non-compact configuration as compared to hot compact configuration. The ΔV_B is reported to be least for the higher angular momentum states.

Finally in the Chapter 6, the optimized orientations criteria is applied further to understand the effect of isotopic dependence by analyzing ^{40,48}Ca+^{238}U$\rightarrow^{278,286}112^*$ reactions across the Coulomb barrier. Also in this chapter, the effect of higher order deformations included upto hexadecapole (β_{4i}) is investigated in the decay and formation of the $^{278,286}112^*$ compound nuclei. With the inclusion of the β_{4i}-deformations, the degree of compactness changes. The maximum barrier height is obtained at the compact angle $\sim 72^0$, which is further confirmed by the barrier position, having minimum value at the same compact angle. In the decay path of $^{278,286}112^*$ compound nuclei, it is observed that HMF region is mainly affected with the inclusion of deformations. The HMF region modified with β_{2i}-static deformed fragmentation is A_2=70-85 which changes to A_2=70-98 decaying fragments for the use of β_{4i}-static deformations. However, the fragmentation potential for LP's and fission region remains almost identical. Confining to optimum orientations associated with β_{2i} deformations, the symmetric fission is dominant for hot equatorial configuration, whereas suppression in its magnitude is seen when hot configuration is replaced by cold polar one. The suppression in the preformation probability is higher for the $^{278}112^*$ nucleus as compared to $^{286}112^*$.

The isospin effects are also studied for Z=114 and 115 superheavy isotopes. As no significant structural difference is observed in the decay of $^{290}114^*$ and $^{292}114^*$ compound nuclei at comparable energies, hence changing N/Z ratio, doesn't play a significant role for these nuclei. In addition to this, the angular momentum and $E_{c.m.}$ do not influence

the fragmentation paths of $^{290,292}114^{*}$ nuclei. The role of changing N/Z ratio is tested further by adding or subtracting two successive neutrons to the different compound nuclei corresponding to Z=114. The comparative decay path of the $^{288}114^{*}$,$^{290}114^{*}$,$^{292}114^{*}$ and $^{294}114^{*}$ shows some slight variations in heavy mass fragment (HMF) and fission region but in general the trend is similar. No such change is observed for the evaporation residue region. Finally, the role of isospin is also studied for Z=115 isotopes formed in ^{48}Ca+^{241}Am, ^{48}Ca+^{243}Am and ^{48}Ca+^{245}Am reactions and $2n$, $3n$ and $4n$ cross-sections are predicted for $^{289}115^{*}$ and $^{293}115^{*}$ compound nuclei.

This work can be extended further to understand the reaction dynamics of light and heavy mass regions of the periodic table, so that a comparative analysis be carried out for better description of nuclear dynamics and associated aspects. Besides this, the methodology may be refined further to explore the phenomenon of deep quasi-fission (DQF), deep inelastic collision (DIC) and other competing nCN channels. In addition to this, one may explore the effect of higher order deformation and associated orientation effects in ground state decays such as α-decay, cluster radioactivity, heavy particle radioactivity (HPR) and spontaneous fission etc.